Oxidation of Strong C-H Bonds by a Powerful O_2-Derived Iron(IV)-Oxo Species

A DISSERTATION
SUBMITTED TO THE FACULTY OF THE
UNIVERSITY OF MINNESOTA
BY

Scott Timothy Kleespies

IN PARTIAL FULFILLMENT OF THE REQUIREMENTS
FOR THE DEGREE OF
DOCTOR OF PHILOSOPHY

Professor Lawrence Que, Jr., Advisor

Acknowledgements

I would like to thank my adviser, Professor Lawrence Que, Jr., for giving me the opportunity to work in his lab and providing me with several interesting and exciting projects which I was able to leave a mark on. I would also like to thank him for his patience and encouragement during my graduate studies. I would also like to thank past and present members of the Que group, particularly Drs. Matthew Cranswick and Katherine Van Heuvelen for teaching me the ins and outs of the resonance Raman setup and having the patience to deal with my numerous questions regarding its fickle nature. I would like to thank Dr. David Boyce and Andy Jasniewski who were my struggle-partners with the resonance Raman. I would also like to thank Drs. Gregory Rohde and Anusree Mukherjee for all their help and valuable insight throughout my research.

I would also like to thank my collaborators, past and present, whose unique projects, and their associated challenges, allowed me to gain a wide breadth of knowledge and lend my expertise to help solve some very interesting problems. I would specifically like to thank Dr. Chien-Wei (Ryan) Chiang, Heather Stout, Professor Way-Zen Lee and Professor Eckard Münck for their help on the BDPP-superoxo project. For their help on the water-oxidation project, I would like to thank Dr. Zoel Codola, Professor Miquel Costas and Dr. Julio Lloret-Fillol.

Finally, I would like to thank my friends and family who helped support me during my graduate career.

Abstract

Dioxygen plays a crucial role in the metabolic processes of living organisms, as both its formation and activation are essential to maintaining life. Nonheme iron enzymes catalyze an amazing array of oxidation reactions utilizing O_2 under mild conditions. Understanding the mechanisms by which nature is able to utilize dioxygen to perform these transformations is of great interest both on a fundamental and practical level. To this end, synthetic systems have been employed to gain in-depth mechanistic insight.

The tridentate ligand Tp^{Ph2} (Tp^{Ph2} = hydrotris(3,5-diphenylpyrazol-1-yl)borate) has been previously used as a synthetic model for the 2-His-1-carboxylate active sites of nonheme iron oxygenases. Addition of an α-keto carboxylate provides a five-coordinate complex that, upon addition of oxygen, undergoes oxidative decarboxylation of the α-keto acid with concomitant self-hydroxylation of a single ortho position of a ligand phenyl ring, thus acting as a functional mimic of α-KG-dependent dioxygenases. As in α-KG-dependent dioxygenases, a Fe(IV)=O species is proposed to be the oxidant that carries out ligand self-hydroxylation. This work focuses on attempts to intercept the reactive iron-oxygen species with hydrocarbons with varying C-H bond dissociation energies (BDE), including *n*-butane. The reactions were analyzed to identify oxidation products and assess the oxidative power of the putative Fe(IV)=O oxidant.

The first step in the activation of O_2 by non-heme iron enzymes is usually the formation of an Fe(III)-superoxo species upon binding of O_2 to the Fe(II) center and subsequent electron transfer. Such species are well characterized in the enzymatic and synthetic heme literature, but only recently have iron-superoxo species been trapped and characterized in nonheme iron enzymes. In this thesis is reported the characterization of the first synthetic mononuclear nonheme Fe(III)-superoxo species by bubbling O_2 into a solution of Fe(II)(BDPP) (BDPP = 2,6-Bis(((S)-2-(diphenylhydroxymethyl)-1-pyrrolidinyl)methyl)pyridine) at -80 °C and its conversion to a Fe(III)-hydroperoxo species through H-atom abstraction and then to a diferric-peroxo species via comproportionation.

Heterobimetallic centers are also involved in oxygen metabolism. In this thesis is reported the characterization of two nonheme heterobimetallic Fe-O-M species: a Fe^{III}-O-Cr^{III} species generated from dioxygen activation and a Fe^{IV}-O-Ce^{IV} intermediate generated during iron-catalyzed water oxidation.

Table of Contents

List of Tables

List of Figures

List of Schemes

Chapter 1: Synthetic Models of 2-Oxoglutarate-Dependent Oxygenases and Reaction Intermediates

1.1 Scope and Aim of Dissertation

Chapter 1 reviews previously published synthetic models of a specific class of oxygen-activating enzymes, 2-oxoglutarate (2OG)-dependent oxidases and oxygenases, and reviews previously published synthetic models of reaction intermediates in dioxygen activation.

Chapter 2 explores the C-H bond cleavage of high-BDE substrates by a pair of nonheme iron complexes which mimic 2-oxoglutarate (2OG)-dependent oxidases and oxygenases. The demonstration that the oxoiron(IV) intermediate generated by these complexes can hydroxylate high-BDE substrates not only provides a stepping stone towards our understanding of how metalloenzymes work, but also highlights the potential such synthetic systems may hold.

Chapter 3 introduces the first synthetic, nonheme, mononuclear Fe(III)-superoxo species and the additional intermediates formed during the exploration of its reactivity. The generation of a Fe(III)-hydroperoxo species through substrate oxidation by the Fe-superoxo species supports the mechanistic notion that Fe-superoxo species can carry out hydrogen atom abstraction from a substrate C-H bond that is necessary for the initiation of the 4-e^- oxidation of substrates by nonheme iron enzymes.

Chapter 4 examines a pair of heterobimetallic Fe-O-M species generated both from dioxygen activation and water oxidation. The comparison of Fe-O-M species bearing isomers of the same ligand are compared and spectroscopic differences are rationalized.

1.2 Introduction

1.2.1 Synthetic Models of 2-Oxoglutarate-Dependent Oxygenases

The 2-oxoglutarate (2OG)-dependent oxidases and oxygenases represent the largest family of non-heme iron enzymes.[1] They employ 2OG as a co-substrate to carry out a variety of metabolic transformations, many of which involve the cleavage of a substrate C–H bond. A consensus mechanism has emerged in which a common pathway in 2OG-dependent enzymes leads to the formation of an Fe(IV)=O species[2] that is capable of a wide array of substrate oxidations, including hydroxylation, halogenation, desaturation, electrophilic aromatic substitution and epoxidation.[3] Mechanistic studies, particularly by the Bollinger/Krebs group[3], have led to the proposed catalytic cycle shown in Figure 1.1.

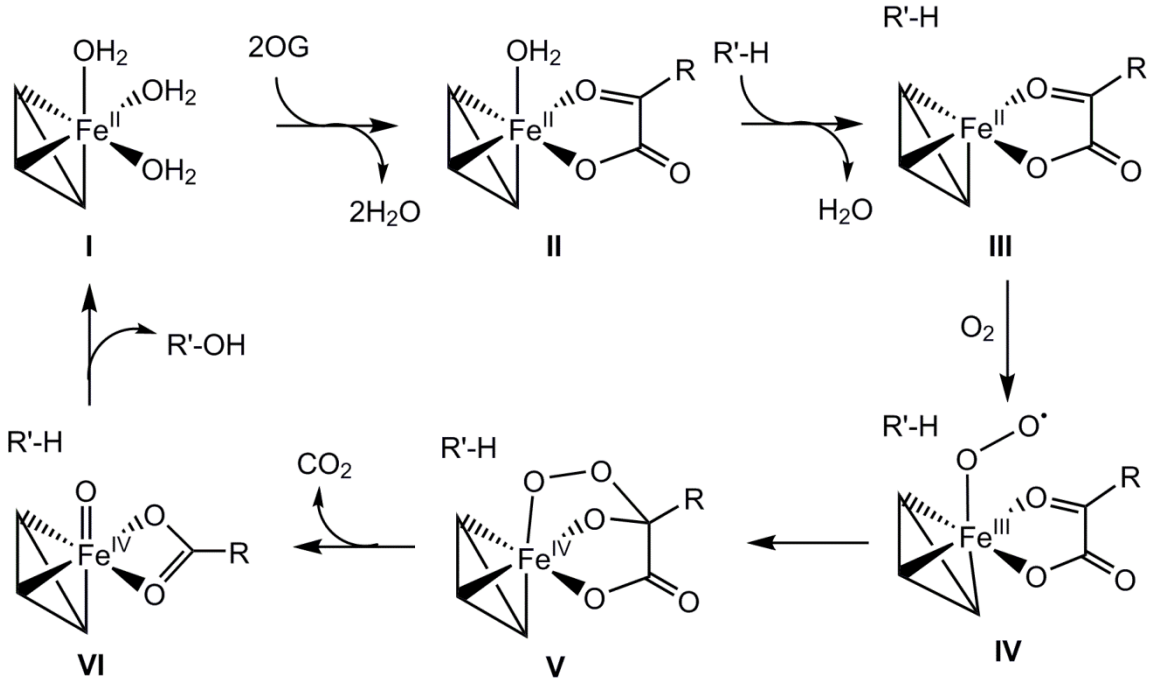

Figure 1.1 Consensus mechanism for 2OG-dependent oxygenases.

The most detailed investigation has been carried out on the enzyme TauD, which catalyzes the hydroxylation of the C_1 position of taurine as a means of recycling sulfur in the cell. Three of the species in the catalytic cycle have been

crystallographically characterized.[4] In the TauD•Fe(II) complex, the Fe(II) center is bound to two histidine and one aspartate residue in a facial arrangement that is referred to as the 2-His-1-carboxylate facial triad, a common motif found among mononuclear non-heme iron enzymes.[5] The three remaining coordination sites in this octahedral complex are occupied by water molecules. Addition of 2OG results in its binding to iron as a bidentate ligand, displacing two water molecules. Taurine binding at the active site, but not to the iron center, expels the third water molecule, resulting in a ternary complex with a five-coordinate Fe center. O_2 binding to the coordinately unsaturated Fe(II) center then forms an Fe(III)-superoxo adduct, and the nascent superoxide attacks the electrophilic 2-oxo carbon atom of the 2OG ligand to afford an alkylperoxo-Fe(IV) intermediate. Subsequent O–O and C-C bond cleavage results in the formation of CO_2, succinate, and an Fe(IV)=O species that is capable of C–H bond cleavage. The hydroxylated product is then produced and the iron center returns to its original oxidation state to start another catalytic turnover. Of the three proposed O_2-derived intermediates, only the Fe(IV)=O species has been trapped.[6–8] This intermediate, called **J** in the TauD cycle, has been shown to have a high-spin (S = 2) Fe(IV)=O center[6] with an Fe–O distance of 1.62 Å (by EXAFS)[9] and a ν(Fe=O) of 821 cm^{-1} (by resonance Raman spectroscopy).[10] Computational studies suggest that the iron(IV) center of intermediate **J** may be either five- or six-coordinate.[11] The rate determining step of the catalytic cycle is the attack of the substrate C–H bond by the Fe(IV)=O moiety, which exhibits an H/D kinetic isotope effect (KIE) of ~50.[7,11] This large KIE allowed TauD-**J** to accumulate in sufficient amounts so as to be characterized by a variety of spectroscopic techniques.

The use of model complexes allows chemists to retain the most pertinent part of the enzyme, the active site, while removing the complexity and synthetic difficulty associated with the rest of the protein. Key features of the active site include the primary coordination sphere, which in 2OG-dependent oxygenases is typically a conserved 2-His-1-carboxylate facial triad,[5] and secondary sphere steric and hydrogen bonding interactions. In model complexes these features may be approximated and tuned by appropriate ligand design choices. Model complexes also allow greater control of the reaction rate through the manipulation of temperature and the use of a wide range of solvents. By controlling the rate of the reaction, intermediates can be trapped and

characterized leading to a greater understanding of the reaction mechanism for the model and subsequent extrapolation to the enzymatic system of interest.

There has long been an interest in using purely chemical systems to provide an understanding of the reactions catalyzed by 2OG-dependent enzymes.[12] Thus, early investigations led to systems that were capable of oxidizing the C-H bonds of substrates by a combination of an iron center with either hydrogen peroxide or a reducing agent and dioxygen.[13–15] Likewise, the iron-mediated oxidative decarboxylation of 2-oxoacids had also been reported.[16,17] However, it was not until the late 1980s that the first example of a system, of relevance to 2OG-dependent enzymes, that catalyzes both the decarboxylation of a 2-oxoacid and the two-electron oxidation of a substrate utilizing dioxygen as a terminal electron acceptor was reported. This system coupled the oxidative decarboxylation of pyruvic acid to the oxidation of cyclohexane using an iron catalyst.[18] Unfortunately, the iron catalyst was poorly defined and a relationship between the structure and reactivity of the iron-containing species was not developed. Studies over the last two decades have provided structurally well-defined functional models of 2OG-dependent enzymes that utilize combinations of iron, a supporting ligand and model substrates and provide significant mechanistic insights.

The first crystallographically characterized synthetic Fe(II)-2-oxoacid complexes utilized the tetradentate ligands tris(2-pyridylmethyl)amine (TPA) and 6-Me_3-TPA (Figure 1.2) with benzoylformate (BF) as the 2-oxoacid.[19,20]

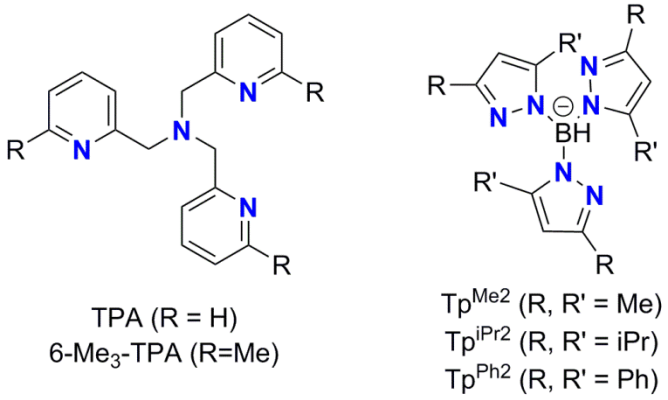

Figure 1.2 Supporting polydentate ligands used to model the active site of 2OG-dependent oxidases and oxygenases.

[(TPA)Fe^{II}(BF)]$^+$ is yellow in color (λ_{max} = 385 nm) and its crystal structure showed the BF to be bound monodentate via a carboxylate oxygen, with the remaining coordination site occupied by a solvent molecule. In non-coordinating solvents like CH_2Cl_2, however, the BF becomes bidentate and the complex is green in color (λ_{max} = 550-610 nm). For the 6-Me_3-TPA complex, the crystal structure showed that the BF bound in a bidentate fashion (Figure 1.3), giving rise to a characteristic purple color (λ_{max} = 544 nm) due to a metal-to-ligand charge transfer (MLCT) transition from a filled d orbital of the Fe(II) to a π^* orbital of the keto group.[21] Similar MLCT features have been seen in 2OG-bound enzymes.[22–25]

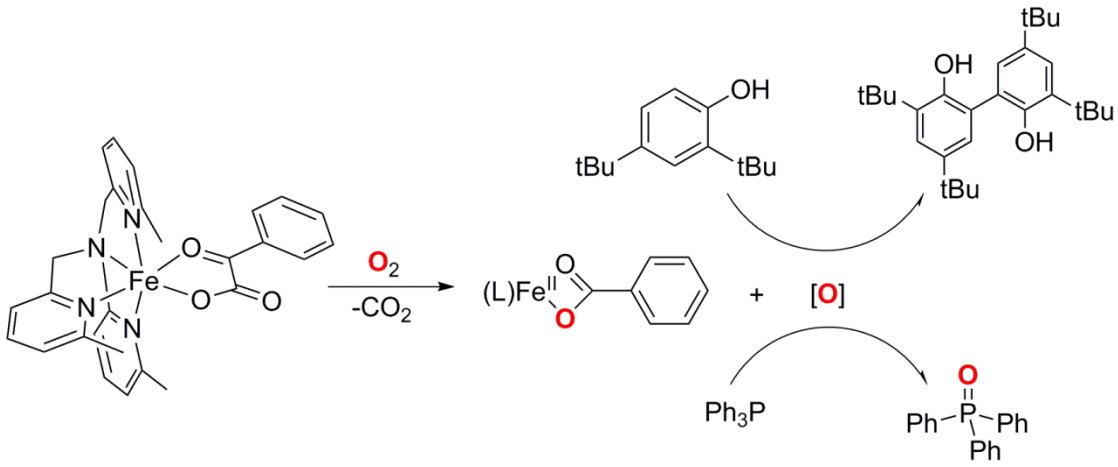

Figure 1.3 Reaction scheme for [(6-Me_3TPA)Fe^{II}(BF)]$^+$.

Both of these model complexes react with dioxygen, albeit over the course of days, to form the corresponding benzoate complexes, which are the products of oxidative decarboxylation of the 2-oxoacid (Figure 1.3). This slow reaction rate is postulated to arise from the fact that the iron center is coordinatively saturated, so ligand dissociation is required to provide an open site for O_2 to bind and allow the reaction to proceed. This is consistent with the consensus mechanism for 2OG-dependent enzymes (Figure 1.1), in which the sequential binding of 2OG and substrate results in the formation of a five-coordinate ternary complex (**III**) with a vacant binding location for dioxygen that is adjacent to the 2OG and proximal to the substrate. The ligand dissociation step is likely to be rate determining, as no direct evidence for any iron-oxygen intermediates could be found. Interception experiments suggest the formation of an O_2-derived oxidant in the

oxidative decarboxylation reaction of these complexes that can perform H-atom abstraction from 2,4-di-tert-butylphenol and oxygen-atom transfer to PPh_3.[20]

Switching a tetradentate ligand to a tridentate ligand should in principle leave an open coordination site on the iron center for O_2 binding and thus result in a faster rate of O_2 activation. The first examples of synthetic Fe(II)-2-oxoacid complexes with a tridentate ligand were obtained through the use of the hydrotris(pyrazolyl)borate ($Tp^{R,R'}$) ligand (Figure 1.2), which more closely mimics the monoanionic facial tridentate ligand set of the "2-His-1-carboxylate facial triad" motif.

[$(Tp^{Me2})Fe^{II}$(BF)] represents the first example of a synthetic facial N3 Fe(II)-2-oxoacid complex.[26] This complex exhibits the characteristic MLCT feature found in the corresponding TPA complexes, indicating bidentate binding of BF. Unlike with the tetradentate TPA complexes, [$(Tp^{Me2})Fe^{II}$(BF)] reacted with O_2 in a matter of minutes and afforded benzoate as a product. The inclusion of cyclohexene or *cis*-stilbene during the oxygenation led to their epoxidation. Of note is the retention of configuration found for the *cis*-stilbene reaction, strongly implicating the formation of a metal-based oxidant like that proposed for the 2OG-dependent enzymes.

The replacement of the methyl groups of the Tp^{Me2} ligand with larger substituents led to the formation of [$(Tp^{R2})Fe^{II}$(2-oxoacid)] complexes that had somewhat slower rates of oxygenation but provided important mechanistic insights. Indirect evidence for the involvement of an iron(III)-superoxo species was found in studies of [$(Tp^{iPr2})Fe^{II}$(pyruvate)].[27] Oxygenation of this complex in MeCN at -40 °C resulted in the formation of an O_2 adduct. This species exhibits a visible absorption band at 682 nm, a ν(O-O) of 889 cm^{-1} obtained from a resonance Raman experiment, and a Mössbauer doublet with an isomer shift δ of 0.65 mm/s and a quadrupole splitting ΔE_Q of 1.35 mm/s. These spectroscopic features are reminiscent of those for the O_2 adducts of [$(Tp^{iPr2})Fe^{II}(O_2CR)$] complexes first reported by Kitajima[28] and later characterized crystallographically by Kim and Lippard,[29] which have a (μ-1,2-peroxo)diiron(III) core that is supported by two carboxylate bridges. In the oxygenation of [$(Tp^{iPr2})Fe^{II}$(PRV)], addition of 2,4,6-tri-*tert*-butylphenol produced the phenoxyl radical in 80% yield and prevented the formation of the peroxo-bridged dimer (Figure 1.4). As the peroxo-bridged

dimer reacted 70-fold more slowly with the added phenol, a reactive precursor to this peroxo species was implicated. This reactive precursor is very likely an initially formed Fe(III)-superoxo species, which abstracts the H-atom from the O–H bond of the phenol to generate the phenoxyl radical.

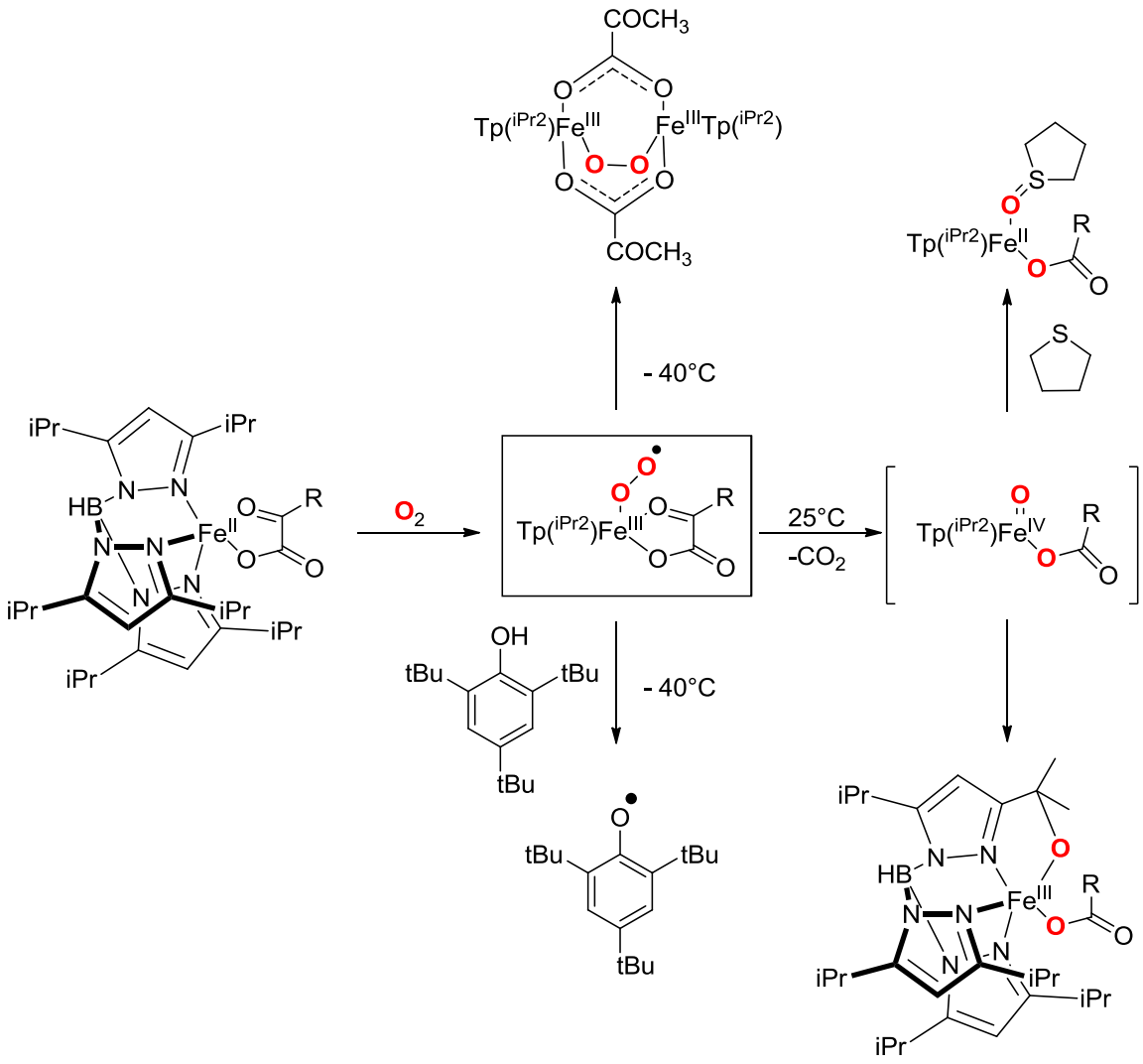

Figure 1.4 Reaction scheme for [(Tp^{iPr2})Fe^{II}(PRV)] (R = Me).

On the other hand, room temperature oxygenation of [(Tp^{iPr2})Fe^{II}(PRV)] gave different results. An oxidized product was observed that exhibited an ESI-MS peak at *m/z* 536, which was formulated to be {(Tp^{iPr2})Fe + O – H}$^{+}$, suggesting the ligand had been oxygenated. The site of oxygenation was determined to be the tertiary C-H of an isopropyl group by a ^{1}H-NMR analysis of pyrazoles obtained by treatment of the product

with strong acid. These results demonstrated that an oxidant was formed that was capable of cleaving a C–H bond on the Tp ligand. When tetrahydrothiophene was added to the [(Tp^{iPr2})Fe^{II}(PRV)] solution before the start of the reaction, the hydroxylated ligand was no longer detected, and instead tetrahydrothiophene was found to be oxidized to its sulfoxide (Figure 1.4). Even one equivalent of tetrahydrothiophene was sufficient for this interception to occur.[27] This potent oxidant that is capable of both oxidizing a C-H bond and oxygenating tetrahydrothiophene is likely to be an Fe(IV)-oxo species, similar to the intermediates proposed in the catalytic cycle of TauD and other 2OG-dependent enzymes.

Experiments with [(Tp^{Ph2})Fe^{II}(BF)] further enhanced our mechanistic understanding.[30] Oxygenation of [(Tp^{Ph2})Fe^{II}(BF)] resulted in the conversion of its purple color (λ_{max} = 531 nm) to green (λ_{max} = 650 nm) over the course of one hour. Characterization of the green product showed that the Tp^{Ph2} ligand had undergone hydroxylation at the ortho position of one of the 3-phenyl rings with the green color arising from a phenolate-to-Fe(III) charge transfer transition. Benzoate was also present in the final reaction mixture, showing that the BF had undergone decarboxylation (Figure 1.5). A crystal structure of the green product confirmed its formulation. Furthermore, the use of $^{18}O_2$ showed a high percentage of ^{18}O incorporation into both the phenolate and the benzoate, thus making this complex an excellent model for the dioxygenase reactivity seen in non-heme iron oxygenases.

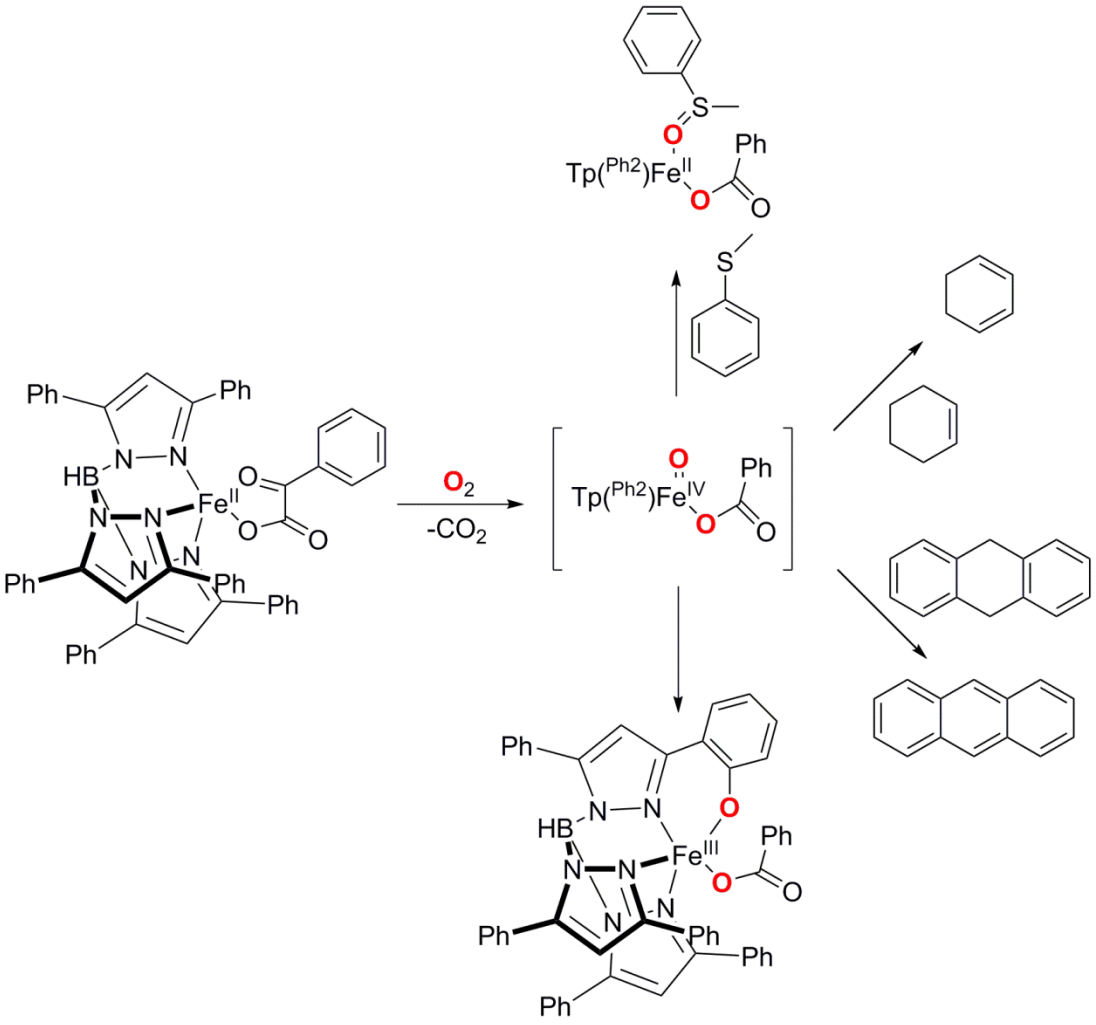

Figure 1.5 Reaction scheme for [(Tp^{Ph2})Fe^{II}(BF)].

Kinetic studies demonstrated that the rate of formation of the green chromophore was first-order with respect to dioxygen and irreversible.[30] Further experiments using substituted BF cofactors showed that electron-withdrawing substituents increased the rate of reaction. A Hammett ρ value of +1.3 was obtained, indicative of a nucleophilic mechanism. The reaction was deduced to have a rate determining step involving the initially formed superoxo species acting as a nucleophile to attack the electrophilic α-keto group of the BF ligand. Thus the rate-determining step in the activation of O_2 by [(Tp^{Ph2})Fe^{II}(BF)] is early in the reaction mechanism and likely to precede the formation of the Fe(IV)=O oxidant.

The kinetic results for the oxygenation of the [(Tp^{Ph2})Fe^{II}(BF)] complexes make it highly unlikely that the putative Fe(IV)=O oxidant can be isolated and characterized. To learn more about the reactivity of this transient species, Mukherjee et al. added potential substrates into the reaction solution to compete with the intramolecular ligand self-hydroxylation, using the deep green chromophore of the self-hydroxylated product as a visual probe to assess the effectiveness of the added substrates at intercepting the proposed oxidant.[31] For example, the addition of 10 equivalents of thioanisole prevented the appearance of the green chromophore and resulted instead in the formation of [(Tp^{Ph2})Fe^{II}(O_2CPh)(PhS(O)Me)] in 70% yield with respect to Fe, showing that intermolecular oxo-transfer can be more facile than intramolecular ligand hydroxylation. Intermolecular H-atom abstraction was also demonstrated. With the addition of 100 equivalents of cyclohexene, only 20% of the green chromophore was observed together with cyclohexadiene as the organic product. The use of cyclohexene-d_{10} afforded the same extent of interception, and the competitive oxidation of cyclohexene and cyclohexene-d_{10} revealed a product kinetic isotope effect of 10. Substrates with C–H bonds as strong as 95 kcal/mol were also oxidized, but with varying interception efficiencies. These results indicate that quite a powerful oxidant can be formed in the oxygenation of [(Tp^{Ph2})Fe^{II}(BF)]. Density function theory (DFT) calculations suggest that this oxidant is likely to be a high-spin Fe(IV)=O complex.[31,32]

The past decade has seen a significant jump in our mechanistic understanding of the chemistry of the 2OG-dependinet enzymes, from studies of the enzymes themselves as well as from the synthesis of relevant model complexes. Several model complexes have been synthesized and characterized, which are structurally comparable to either the binary or ternary complexes (**II** and **III**, respectively, in Figure 1.1) of 2OG-dependent enzymes and serve as functional models of these enzymatic reactions. The significantly higher reactivity of the five-coordinate model complexes compared to their six-coordinate counterparts emphasizes the importance of having a vacant coordination site for efficient O_2 binding and subsequent reactivity, as borne out by the observed displacement of water in the enzyme active site that occurs only upon substrate binding in order to prime the iron center in the 2OG-dependent enzyme for catalysis. The absence of

this control would result in the wasteful uncoupling of 2OG oxidative decarboxylation from substrate oxidation.

The oxidations carried out by these functional models encompass a number of enzymatically relevant reaction types including dehydrogenation, hydroxylation, epoxidation and electrophilic aromatic hydroxylation. Mechanistic studies have indicated that all of these reactions are likely carried out by a transient Fe(IV)=O species (**VI**, in Figure 1.1), which exhibits remarkable versatility in terms of its reaction scope. Although this transient species has not yet been observed or spectroscopically characterized in any of the functional models, the trapping of such a reaction intermediate would be a phenomenal achievement for the synthetic field. Additionally, interception experiments have provided indirect evidence for the initial formation of an Fe(III)-superoxo moiety (**IV**, Figure 1.1) prior to the formation of the Fe(IV)=O oxidant, providing the first experimental evidence for such a species in a catalytic cycle of relevance to 2OG-dependent enzymes.

1.2.2 Synthetic Models of Reaction Intermediates in Enzymatic O_2 Activation

The activation of dioxygen (O_2) for the controlled oxidation of organic substrates by metalloenzymes is involved in many key metabolic functions such as DNA and RNA repair, antibiotic synthesis and the sensing of hypoxia in cells.[12] Because of the importance and breadth of these reactions, much work has focused on understanding the mechanisms of dioxygen activation by metalloenzymes. Despite the variety of reactions catalyzed and the diversity of the active sites, a common mechanistic scheme for the activation of dioxygen has emerged (Figure 1.6). In most mononuclear nonheme systems, the first step is the binding of dioxygen to the Fe(II) center to form an Fe(III)-superoxo species. From this species, there are multiple possible paths to generate subsequent intermediates from the Fe-superoxo precursor.

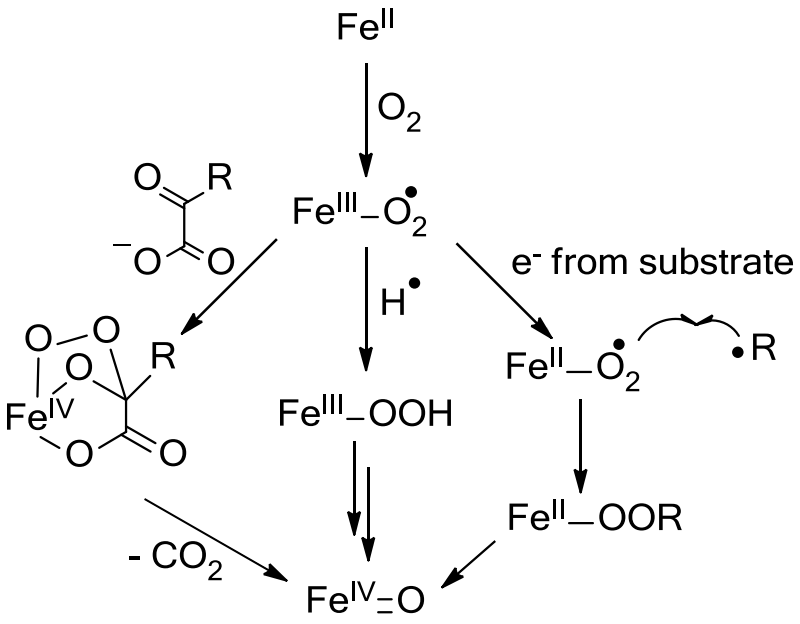

Figure 1.6 Dioxygen activation mechanisms starting with an Fe(III)-superoxo and ending with an Fe(IV)=O.

As stated in the previous section, for one class of enzymes, 2-oxoglutarate (2OG)-dependent oxidases and oxygenases, this Fe-superoxo species attacks the electrophilic 2-oxo carbon atom of the 2OG ligand to afford an Fe(IV)-alkylperoxo intermediate. Subsequent O–O and C-C bond cleavage results in the formation of CO_2, succinate, and an Fe(IV)=O species that is capable of C–H bond cleavage (Figure 1.1). An alternate route is through the addition of an H-atom, via hydrogen atom abstraction (HAA) of the substrate, to form an Fe(III)-hydroperoxo species. Subsequent electron-transfer from the substrate to the Fe-center forms an Fe(II)-hydroperoxo species, which then performs a second HAA and undergoes O-O bond cleavage to form a high-valent Fe(IV)-oxo species, as proposed for Isopenicillin *N* synthase (IPNS).[33] A third route involves an electron-transfer from the substrate to the Fe-center, post Fe-superoxo formation, followed by coupling of the superoxo and substrate radicals to form an Fe(II)-alkylperoxo species. Subsequent O-O bond cleavage generates a high-valent Fe-oxo species, as proposed for one possible mechanism in cysteine dioxygenase (CDO),[34] or leads to the insertion of an oxygen atom into an aromatic ring, as proposed for homoprotocatechuate

2,3-dioxygeanse (2,3 HPCD).[35] The wealth of intermediates generated during dioxygen-activation by metalloenzymes has spurred synthetic chemists to attempt to create synthetic models of these reaction intermediates to better understand their features and reactivities.

Despite the ubiquity of the iron-superoxo intermediate in the activation of O_2 by nonheme mononuclear enzymes, only a handful have been spectroscopically characterized.[34–37] A dinuclear nonheme iron-superoxo complex, $[Fe^{II}_2(6\text{-}Me_3TPA)_2(\mu\text{-}OH)_2]^{2+} + O_2$, has been characterized and showed a resonance-enhanced feature at 1310 cm^{-1}, which was assigned to the O-O vibration of the bound superoxo. Unfortunately, further characterization by Mössbauer or X-ray absorption studies were unable to be conducted due to the requirement of CH_2Cl_2, which has a very high electronic extinction coefficient in the 6 - 14 keV range, as solvent to generate this species.[38]

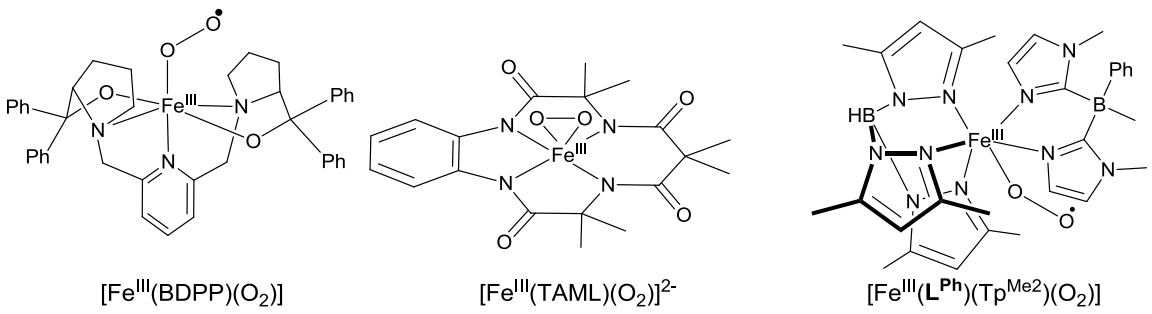

Figure 1.7 Nonheme, mononuclear, synthetic Fe(III)-superoxo species.

The first synthetic mononuclear, nonheme Fe(III)-superoxo species, $[Fe^{III}(BDPP)O_2]$, was recently trapped and characterized (Figure 1.7).[39] This species showed a resonance-enhanced vibration at 1125 cm^{-1}, while Mössbauer spectroscopy revealed a high-spin iron center that is ferromagnetically coupled to the superoxo radical, giving a net S = 3 ground state.[39] The net S = 3 ground state is similar to that seen in CDO [34] while HPCD [35] has a net S = 2 ground state because of antiferromagnetic coupling between the Fe-center and superoxo radical. The fact that nature uses both ferro- and antiferromagnetic coupling is interesting, and with the generation of additional synthetic species more insight into the reactivities of each type can be explored to lend insight into nature's use of both spin states. $[Fe^{III}(BDPP)O_2]$ was also found capable of

carrying out HAA from a substrate C-H bond, supporting the notion that initial oxidation of substrate by Fe-superoxo species is a viable pathway for the 4-e^- oxidation of substrates by nonheme iron enzymes. Since the characterization of [Fe^{III}(BDPP)O_2], an additional pair of mononuclear Fe-superoxo species have been trapped and characterized, [Fe^{III}(TAML)(O_2)]$^{2-}$ [40] and [Fe^{III}(**L**^{Ph})(Tp^{Me2})O_2] [41] (Figure 1.7). These species show spectroscopic features characteristic of Fe-superoxo species; rR values of 1260 and 1168 cm^{-1}, respectively, and integer-spin ground states through the coupling of the Fe-center and the superoxo radical (Table 1.1). [Fe^{III}(**L**^{Ph})(Tp^{Me2})O_2] was found to form a Fe(III)-hydroperoxo species from HAA of a substrate. This represents the first such synthetic example of this transformation.[41] The Fe(III)-hydroperoxo species was characterized as low-spin with a ν(O-O) frequency of 778 cm^{-1}.

Table 1.1. Spectroscopic data for Fe-superoxo species

	$[Fe^{II}_2(\mu\text{-}OH)_2\text{-}(6\text{-}Me_3TPA)_2]^{2+} + O_2$	$[Fe^{III}(BDPP)O_2]$	$[Fe^{III}(TAML)(O_2)]^{2-}$	$[Fe^{III}(\mathbf{L}^{Ph})(Tp^{Me2})O_2]$	2,3-HPCD	CDO
Ox State	3+, 2+	3+	3+	3+	3+	3+
Fe Spin State Ground State (coupling)	- - (AF)	5/2 (HS) 3 (F)	3/2 (IS) 1 (AF)	1/2 (LS) 0 (AF)	5/2 (HS) 2 (AF)	5/2 (HS) 3 (F)
ν(O-O), cm-1 ($\Delta^{18}O$)	1310 (-71)	1125 (-63)	1260[a] (-77)	1168 (-78)	-	-
Binding Mode	End-on	End-on	Side-on	End-on	End-on	End-on
λ_{max}, nm (ε_M), M^{-1} cm^{-1}	325 (10300)	330 (9400)	490 (2600)	350 (-)	-	565 (-)
δ, mm/s	-	0.58(3)	0.10	-	0.50(1)	-
ref	38	39	40	41	35	34

[a] Value obtained by IR. AF = antiferromagnetically coupled. F = ferromagnetically coupled. HS = High-spin. IS = Intermediate spin. LS = Low spin.

Following superoxo formation, the next step in O_2 activation for (2OG)-dependent oxidases and oxygenases is the formation of a putative Fe(IV)-alkylperoxo (Figure 1.1). No examples have been trapped during enzyme reactions and synthetic mimics of this species are sorely lacking with only one well-defined example currently known.[42,43] $[Fe^{IV}(\beta\text{-BPMCN})(OO^tBu)(OH)]^{2+}$ was generated by the reaction of the Fe(II)-complex with ^{t}BuOOH and showed resonance-enhanced features at 832 and 845 cm^{-1}, which were assigned to the O-O vibration of the bound alkylperoxo (Figure 1.8). This species was found to undergo Fe-O bond cleavage, as opposed to the O-O bond cleavage required in the oxidative decarboxylation step proposed for the catalytic cycle of 2OG-dependent enzymes.

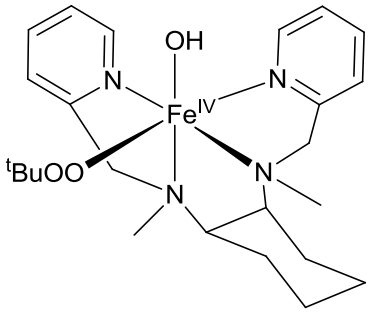

$[Fe^{IV}(\text{-BPMCN})(OO^tBu)(OH)]^{2+}$

Figure 1.8 Proposed structure for an Fe(IV)-alkylperoxo species.

While the superoxo intermediate has been proposed as merely a step towards the formation of the active oxidant for 2OG-dependent enzymes, there are a growing number of enzymes for which the proposed mechanism requires that substrate oxidation be initiated by the Fe(III)-superoxo intermediate.[44,45] For enzymes such as isopenicillin *N* synthase (IPNS),[33] *myo*-inositol oxygenase (MIOX),[36] CloR,[46] and 2-hydroxyethyl phosphonate dioxygenase (HEPD),[47] this initial oxidation involves HAA to form a Fe(III)-hydroperoxo species (Figure 1.6).[45] There are several well characterized synthetic Fe(III)-hydroperoxo complexes that, until recently, had exclusively been generated by either the addition of H_2O_2 to the Fe(II) precursor or protonation of a Fe(III)-peroxo species.[48–52] These Fe(III)-hydroperoxo species fall into two classes based on the spin-

state of the Fe-center, which is reflected in the ν(O-O) frequency. Low-spin Fe(III)-hydroperoxo complexes exhibit ν(O-O) frequencies in the 778-811 cm^{-1} range, while those with a high-spin Fe-center range from 838-891 cm^{-1}. Both HS and LS Fe(III)-hydroperoxo species have been detected in nature and can be characterized by their chemistry; LS species have been found to cleave strong C-H bonds[53,54] while HS species oxidize electron-rich aromatics.[55–57] The ability to generate both HS and LS synthetic systems has allowed for the combined experimental/computational study into C-H bond activation.[58] This study found, in line with what is observed in nature, that LS complexes should be more reactive towards strong C-H bonds, while HS species should be more reactive towards substrates with low ionization potentials and weak C-H bonds. For enzymes such as MIOX and HEPD, the Fe(III)-hydroperoxo species is proposed to undergo O-O bond cleavage to generate a high-valent Fe-oxo.[45] Such a transformation was seen for a HS Fe(III)-hydroperoxo supported by the TMC ligand.[48]

The third possible pathway for the Fe(III)-superoxo intermediate is similar to what has been observed for 2OG-dependent enzymes, in that the formation of an Fe-alkylperoxo eventually leads to O-O bond cleavage and generation of a high-valent oxidant.[34] However, the route taken to reach the Fe-alkylperoxo species is substantially different. In this mechanism, electron-transfer from an electron-rich substrate, an aromatic ring in 2,3-HPCD and a sulfur group in CDO, to the Fe-center generates a substrate radical which then couples with the Fe-bound superoxo radical to form an Fe(II)-alkylperoxo (Figure 1.6). Such a species was trapped *in crystallo* for 2,3-HPCD when an alternative substrate, 4-nitrocatechol, was used.[37] To date there are no nonheme synthetic model complexes that mimic this unique species, thus preventing in-depth study of the characteristics and reactivity of such a distinctive intermediate.

Chapter 2: C-H Bond Cleavage by Bioinspired Nonheme Oxoiron(IV) Complexes, Including Hydroxylation of n-Butane

2.1 Introduction

The efficient oxidation of hydrocarbons under mild conditions and utilizing environmentally benign reagents is a challenging task which has garnered considerable interest over the last few decades.[59] More recently, there has been intense focus on the oxidation of gaseous alkanes, especially methane, as new oil and gas extraction technologies and techniques have opened up entirely new sources of these fuels.[60] There are numerous inherent challenges associated with the oxidation of alkanes that nature has found ways of overcoming. Metalloenzymes have evolved to perform selective and efficient oxidation of inert C-H bonds under mild conditions and using environmentally benign reagents.[12,61] These enzymes harness the power of molecular oxygen to generate high-valent oxidants which perform numerous challenging oxidative transformations of C-H bonds. In nonheme iron-containing enzymes, this oxidant is proposed to be a Fe^{IV}=O species.[1,3,62]

To understand how metalloenzymes are able to perform such reactions and gain insight into the nature of the oxidant, chemists have developed synthetic models to better understand the mechanism and to study the reactive species utilized. There are currently over 60 characterized synthetic nonheme Fe^{IV}=O complexes.[63–66] These species have provided a wealth of structural, spectroscopic and reactivity data.

All the synthetic nonheme Fe^{IV}=O complexes described to date have been generated by an oxidant other than O_2, which has allowed them to accumulate and be characterized with various spectroscopic methods and sometimes by X-ray crystallography.[63–66] A rare exception to this pattern is the putative oxoiron(IV) species that is produced by the oxygenation of $[Fe^{II}(Tp^{Ph2})(O_2CC(O)Ph)]$ (**1a**), an iron(II) complex that serves as a functional model for the α-ketoglutarate (α-KG)-dependent enzymes like TauD (Figure 2.1). Upon exposure to O_2 in benzene solvent at room temperature, **1a** undergoes oxidative decarboxylation of its benzoylformate ligand (the α-ketoglutarate analog) to form a green chromophore designated as $[Fe^{III}(Tp^{Ph2}*)(O_2CPh)]$ (**2a**).[30] The latter has been identified as an iron(III)-phenolate complex, resulting from the self-hydroxylation of one of the ligand phenyl rings (Figure 2.1). Kinetic studies show that the reaction rate is first order in iron complex and first order in O_2,[30] indicating that

the rate determining step corresponds to an early phase of the reaction. By analogy to the α-KG-dependent enzymes, it is proposed that the oxidative decarboxylation step forms a yet unobserved Fe^{IV}=O oxidant **3a**, which DFT calculations suggest to have an *S* = 2 ground state when the carboxylate is coordinated in a monodentate fashion.[31,67]

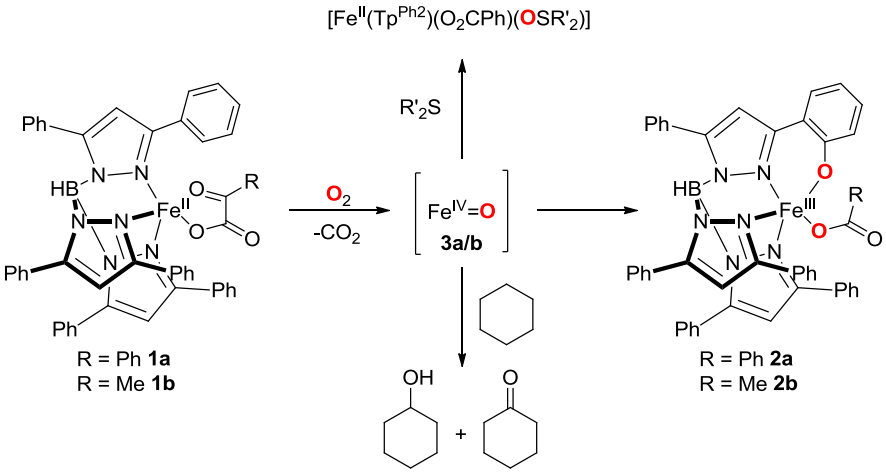

Figure 2.1. Some reactions of **1a/b** with O_2 in benzene at 25 °C.

It has previously been shown that it was possible to intercept the high-valent species **3a** by introducing external substrates that could be oxidized intermolecularly in competition with the intramolecular ligand hydroxylation.[31] The lower yield of the green chromophoric product from the latter reaction was used as a convenient probe for assessing the relative rates of intermolecular and intramolecular oxidation. Indeed, the addition of 10 equiv. thioanisole (PhSMe) into the reaction of **1a** with O_2 completely prevented the intramolecular self-hydroxylation. Instead, a colorless $[Fe^{II}(Tp^{Ph2})(O_2CPh)(OSR_2)]$ adduct was observed based on ESIMS, NMR, and Mössbauer evidence. The sulfoxide adduct formed in 70% yield, a value comparable to the amount of self-hydroxylated product obtained in the absence of thioanisole.

Probing the thioanisole interception further revealed some interesting but expected insights. The addition of stoichiometric PhSMe suppressed formation of the self-hydroxylated product by 60%, demonstrating the high oxo-transfer ability of the putative Fe^{IV}=O oxidant **3a**. Substituting PhSMe with the more electron-rich

tetrahydrothiophene decreased by 90% the amount of self-hydroxylated product, while the less electron-rich Ph_2S had the opposite effect (40%). So **3a** is sensitive to the basicity of the substrate. It should be noted however that the reaction time was unchanged for these three experiments as the rate determining step is associated with the formation of **3a** rather than its decay.

In the 2009 paper on this system, limited success was reported in intercepting **3a** with hydrocarbons.[31] While addition of substrates with weak C–H bonds such as 9,10-dihydroanthracene, fluorene, or cyclohexene significantly decreased the yield of the self-hydroxylated product, substrates with stronger C–H bonds were much less effective. Indeed, the addition of 0.1 M ethylbenzene (BDE = 87 kcal mol^{-1}), toluene (BDE = 90 kcal mol^{-1}), or cyclohexane (BDE = 99 kcal mol^{-1}) did not affect the yield of **2a**, raising the possibility that **3a** may not be a powerful enough oxidant to be able to cleave these stronger C–H bonds. However, the observation that the use of 0.1 M cyclooctane (BDE = 95 kcal mol^{-1}) as substrate slightly decreased the yield of **2a** provided some incentive to follow up on these earlier observations and obtain the more recent results described below.

2.2 Results and Discussion

In these more recent experiments, we have used higher substrate concentrations in order to increase the intermolecular oxidation rate and enhance the likelihood of intercepting the nascent Fe^{IV}=O oxidant **3a**. Indeed this expectation has been borne out in the reactions of **1a** with O_2 in the presence of up to 2 M toluene or cyclohexane (Figure 2.2 top and Table 2.1). For example, with 1 M toluene, the yield of **2a** decreased from 64% to 48% concomitant with the formation of PhCHO in 33% yield. Even more significant were the experiments with 1 M cyclohexane where even less **2a** was formed (34%) and cyclohexane oxidation products were obtained in 44% yield with a 1:3 ratio of cyclohexanol to cyclohexanone. Parallel experiments carried out on the corresponding pyruvate complex $[Fe^{II}(Tp^{Ph2})(O_2CC(O)CH_3)]$ (**1b**) to serve as a check on the generality of the results obtained for **1a** gave comparable results (Figure 2.3 top and Table 2.1). In previous work, **1b** was found to react with O_2 fourfold more rapidly than **1a** at 25 °C, achieving completion within 15 min (versus 1 h for **1a**), but the amount of self-

hydroxylated **2b** obtained was lower.[30] The lower extent of self-hydroxylation for **1b** may reflect a less efficient formation of **3b** relative to that of **3a** or the decay of a higher fraction of **3b** via an alternative unproductive pathway in competition with self-hydroxylation. However, as seen in Figure 2.2 bottom, Figure 2.3 bottom and Table 2.1, the oxygenation of **1b** gave rise to intermolecular oxidation products either equal to or higher than **1a**.

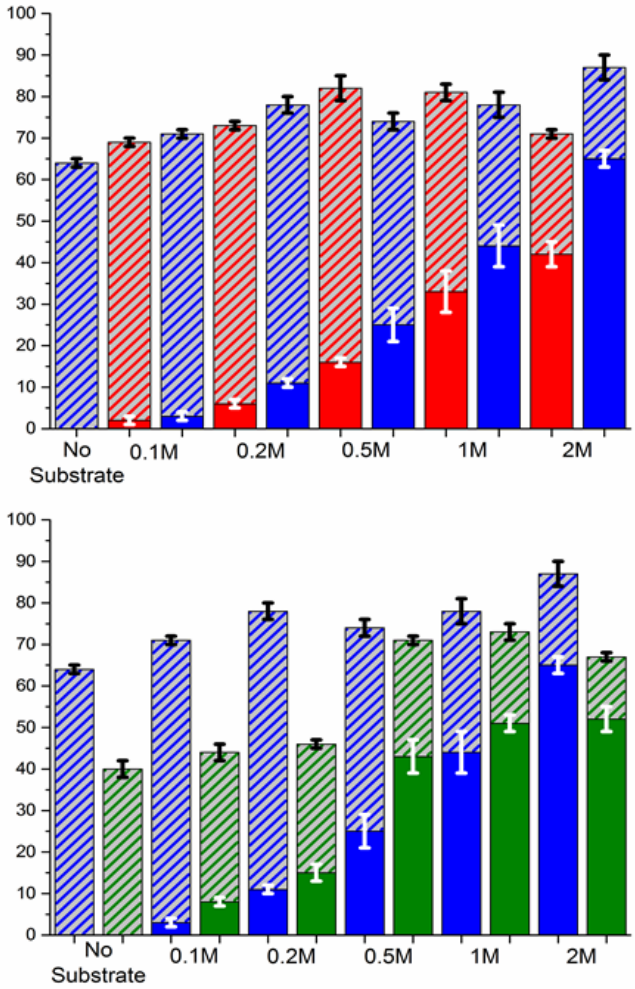

Figure 2.2. Top: Comparison of product yields in the reactions of **1a** with O_2 as a function of cyclohexane (blue) or toluene (red) concentration. Bottom: Comparison of product yields in the reactions of **1a** (blue) and **1b** (green) with O_2 as a function of cyclohexane concentration. Solid bars: yield of oxidized substrate. Dashed bars: yield of **2a/b**. See Figure 2.1 for structures of **1a** and **1b**.

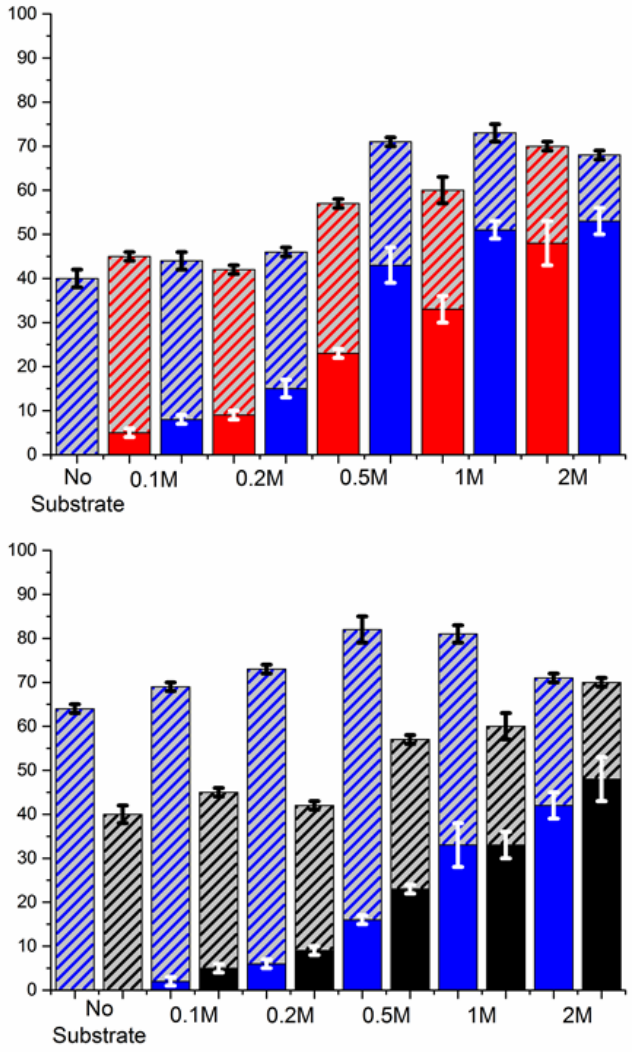

Figure 2.3. Top: Comparison of product yields in the reactions of **1b** with O_2 as a function of cyclohexane (blue) or toluene (red) concentration. Bottom: Comparison of product yields in the reactions of **1a** (blue) and **1b** (black) with O_2 as a function of toluene concentration. Solid bars: yield of oxidized substrate. Dashed bars: yield of **2a/b**.

Table 2.1. Product yields in the reactions of O_2 with $Fe^{II}(Tp^{Ph2})$(BF/PRV) (**1a/b**)

Substrate	[sub]	Self-Hydroxylation Yield		Substrate Oxidation Yield		Total Yield	
		1a	**1b**	**1a**	**1b**	**1a**	**1b**
none	-	64(1)	40(2)	0	0	64(1)	40(2)
cyclohexane	0.1M	68(1)	36(2)	3(1)	8(1)	71(2)	44(3)
cyclohexane	0.2M	67(2)	31(1)	11(1)	15(2)	78(3)	46(3)
cyclohexane	0.5M	49(2)	28(1)	25(4)	43(4)	74(6)	71(5)
cyclohexane	1M	34(3)	22(2)	44(5)	51(2)	78(8)	73(4)
cyclohexane	2M	22(3)	15(1)	65(2)	53(3)	87(5)	68(4)
toluene	0.1M	67(1)	40(1)	2(1)	5(1)	69(2)	45(2)
toluene	0.2M	67(1)	33(1)	6(1)	9(1)	73(2)	42(2)
toluene	0.5M	66(3)	34(1)	16(1)	23(1)	82(4)	57(2)
toluene	1M	48(2)	27(3)	33(5)	33(3)	81(7)	60(6)
toluene	2M	29(1)	22(1)	42(3)	48(5)	71(4)	70(6)

Reaction conditions: ~1 mM Fe^{II} complex, 20 °C. Each value is an average of at least three runs.

Table 2.2. Alcohol/Ketone Product Yields of Cyclohexane Oxidation Reactions

	1a		**1b**		**1a**	**1b**
[substrate]	Alcohol	Ketone	Alcohol	Ketone	A/K	A/K
2M	16	47	2	52	1/2.9	1/26
1M	12	34	2	50	1/2.8	1/25

Table 2.3. Protio versus Deutero Substrate Product Yields for PKIE Determination

	1a		**1b**		PKIE	
Substrate	D	H	D	H	**1a**	**1b**
5:1 d:h Cyclohexane	7[a]	17[a]	8[a]	19[a]	12	12
5:1 d:h Toluene	2500[b]	7500[b]	2200[b]	6600[b]	15	15

[a] Yields reported correspond to the amount of ketone product seen. The yield of the alcohol was too low to be accurately determined. [b] Yields were determined by the relative abundance of the M+1 peaks in the MS spectra.

The major (or only) oxidation products observed in toluene and cyclohexane oxidation are not the alcohols but the corresponding aldehyde or ketone (Table 2.2). These outcomes suggest two mechanistic possibilities. The first scenario entails the subsequent oxidation of the initially formed alcohol product by a second equivalent of **3**. This notion is not implausible because the oxygenation of the iron(II) precursor being rate determining makes this step slower than the substrate oxidation step, and alcohol oxidation would be expected to be much more facile than oxidation of the hydrocarbon. The second scenario involves diffusion of the alkyl radical formed in the initial H-atom abstraction into solution and reacting with the excess O_2 present. At this point, we are unable to assess the likelihood of the nascent alkyl radical undergoing oxygen rebound. What is clear however is that the nascent alkyl radical is formed by the action of a metal-based oxidant, based on results from competitive experiments between a substrate and its perdeuterated analog in their respective oxidations by **1a** and **1b**. Product analysis showed product kinetic isotope effects (PKIE) of 12 for cyclohexane oxidation and 15 for toluene oxidation (Table 2.3). Such nonclassical KIE values have been observed for the reactions of C–H bonds with a number of nonheme oxoiron(IV) complexes[68–72] and support the postulate that **3** is also a member of this class of high-valent iron complexes.

Having demonstrated the ability of **3** to oxidize cyclohexane, we shifted our attention to the light alkane substrate *n*-butane, which has a high solubility in benzene (approximately 4 M at 10 °C by NMR). Indeed, bubbling *n*-butane into a benzene solution of **1a** or **1b** followed by O_2 resulted in a lower yield of **2a/b** (39%/20%),

suggesting the interception of **3a/b** by *n*-butane. ^{1}H-NMR analysis of the product solution showed the characteristic multiplets of the C2 proton of 2-butanol at δ 3.7 ppm and the C3 protons of 2-butanone at 1.8 ppm (Figure 2.4).

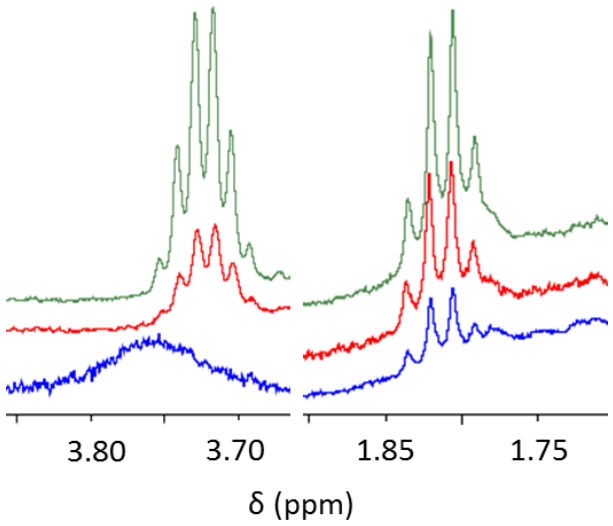

Figure 2.4. Left: Stacked NMR spectra showing the $CH_3CH_2C(\boldsymbol{H})OHCH_3$ (3.7 ppm) peak in a reaction solution of **1a** under various conditions. Bottom/Blue: Oxidation reaction with *n*-butane as substrate. Middle/Red: Reaction mixture upon addition of 25 uL DMSO-d_6 and 2 uL AcOD-d_4 (0.18 mM/Fe). Top/Green: Reaction mixture from middle spiked with 2-butanol (0.49 mM/Fe). Right: NMR spectra showing the changes in the intensity of the $CH_3C(\boldsymbol{H}_2)COCH_3$ (1.8 ppm) peak upon the addition of 2-butanone to a reaction solution of **1a.** Bottom/Blue: Oxidation reaction with *n*-butane as substrate (0.12mM/Fe). Middle/Red: Solution in blue spiked with 2-butanone (0.36 mM/Fe). Top/Green: Solution in red spiked with additional 2-butanone (0.70 mM/Fe).

Because the region below 1.8 ppm contained strong signals from residual *n*-butane, 1D-TOCSY experiments were carried out to identify protons coupled to these multiplets as a means of corroborating our assignments. Indeed, features were observed at 1.5, 1.2 and 0.8 ppm upon irradiation of the 3.7-ppm multiplet belonging to 2-butanol

(Figure 2.5) and at 1.6 and 0.8 ppm in the corresponding experiment for the 2-butanone multiplet at 1.8 ppm (Figure 2.6).

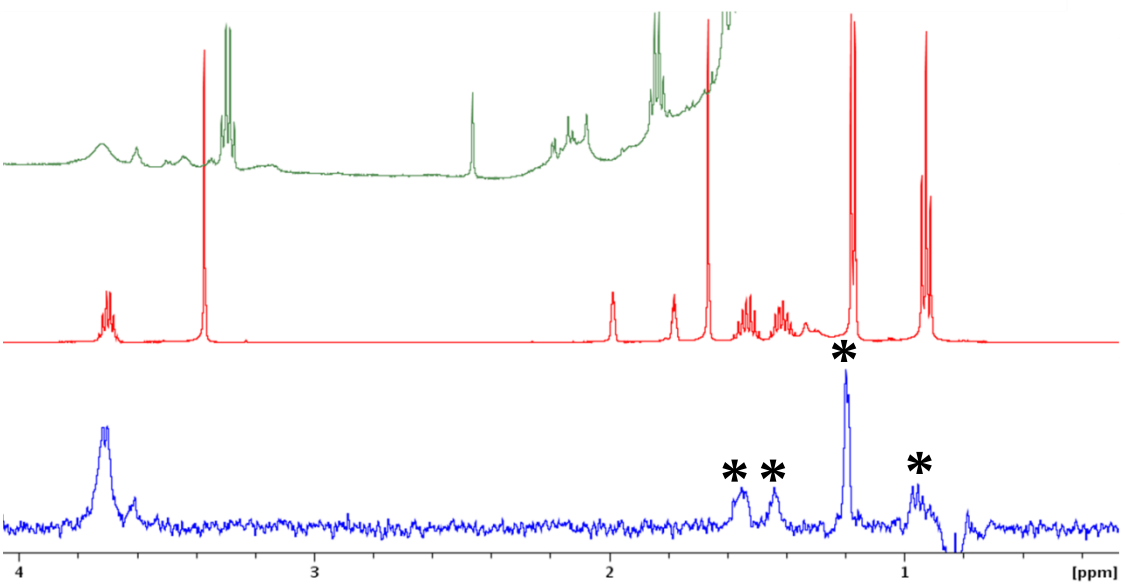

Figure 2.5. Top/Green: ^{1}H-NMR spectrum at the end of a reaction of **1b** and O_2 with *n*-butane in benzene-d_6. Middle/Red: ^{1}H-NMR spectrum of authentic 2-butanol in benzene-d_6 after the addition of DMSO-d_6 and AcOD-d_4. Bottom/Blue: 1D-TOCSY spectrum upon irradiation of the $CH_3C\boldsymbol{H}C(OH)CH_3$ (3.7 ppm) proton of 2-butanol at the end of a reaction of **1b** and O_2 with *n*-butane in benzene-d_6. The peaks marked with an * highlight the peaks enhanced upon irradiation of the $CH_3C\boldsymbol{H}C(OH)CH_3$ (3.7 ppm) proton of 2-butanol.

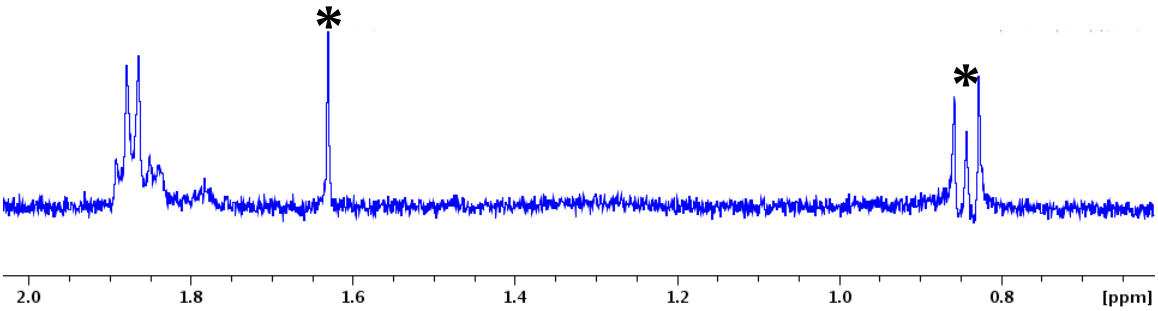

Figure 2.6. 1D-TOCSY spectrum upon irradiation of the $CH_3C\boldsymbol{H}_2C(O)CH_3$ (1.8 ppm) protons of 2-butanone at the end of a reaction of **1a** and O_2 with *n*-butane in benzene-d_6. The peaks marked with an * highlight the peaks enhanced upon irradiation of the $CH_3C\boldsymbol{H}_2C(O)CH_3$ (1.8 ppm) protons of 2-butanone.

It should be noted that the signal from the C2 proton of 2-butanol in the reaction mixture was broad and lacked resolution, which was similar to the spectrum observed for 2-butanol alone in benzene (Figure 2.7). As shown in Figure 2.4 (left), addition of small amounts of dimethyl sulfoxide (DMSO) and acetic acid (AcOH) into the reaction mixture substantially sharpened the C2 proton peak and shifted it upfield. We attribute the broadness of the 2-butanol C2-H signal to a hydrogen-bonded cluster of the alcohol in the nonpolar benzene solvent, which was disrupted upon addition of DMSO and AcOH. Integration of the signals relative to an added tetrachloroethane standard revealed that 2-butanol and 2-butanone were formed in respective yields of 18 and 12% for the reaction with **1a** and of 24 and 15% for the reaction with **1b**. In both cases, addition of aliquots of either 2-butanol or 2-butanone increased the intensities of the 3.7-ppm and the 1.8-ppm peaks, as expected (Figure 2.4). No evidence was found in the NMR spectra for any product arising from C1 oxidation.

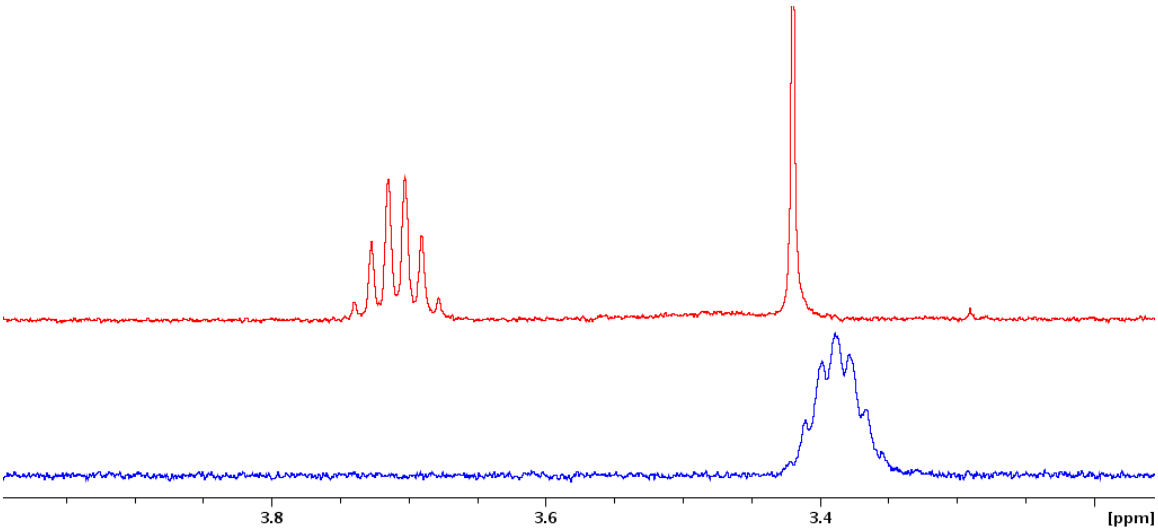

Figure 2.7. Overlay of ^{1}H-NMR spectra showing the changes in peak shape and chemical shifts upon the addition of additives. Bottom/Blue: A benzene-d_6 solution of 2-butanol. Top/Red: Solution in blue upon the addition of 25 uL DMSO-d_6 and 25uL AcOD-d_4. The broad septet becomes better resolved upon addition of DMSO as this additive breaks H-bonding interactions between 2-butanol molecules in benzene. The septet becomes a sextet upon addition of AcOD (red spectrum) due to faster exchange of the OH proton on 2-butanol with deuterium from AcOD.

Our success with *n*-butane led us to attempt other gaseous alkanes. Since we saw no evidence for C1 oxidation with *n*-butane, we decided to utilize ethane as a substrate because it presented only terminal methyl groups for oxidation and these C-H bonds are of a high BDE (BDE = 101 kcal mol^{-1}). Unfortunately, bubbling ethane into a benzene solution of **1a/b** followed by O_2 resulted in no noticeable decrease in **2a/b** nor the detection of any oxidation products. While this lack of oxidation was disappointing, we can rationalize why we did not have success under these conditions. At 25 °C, the solubility of ethane in benzene, by ^{1}H-NMR, is only ~0.07 M, a concentration that is too low to expect to see any detectable oxidation. Therefore, modification to the procedure, such as increasing the pressure of the reaction mixture, will likely need to be employed in attempts to oxidize ethane and, ultimately, methane.

Further attempts at the oxidation of terminal methyl groups were attempted with *t*-butanol (BDE = 100 kcal mol^{-1}). The addition of 1 M *t*-butanol into a benzene solution of **1a/b** followed by O_2 resulted in a lower yield of **2a/b** (55%/30%), suggesting the interception of **3a/b** by *t*-butanol. Despite numerous attempts by ^{1}H-NMR and GCMS, no oxidized products for this reaction were detected. Further analysis is required to confirm that the decrease in the yield of **2a**/**b** is caused by the oxidation of *t*-butanol and not some unproductive decay.

2.3 Summary

The oxidation of *n*-butane by **3** represents the only system thus far to mediate the non-free-radical oxidation of a gaseous alkane by a high-valent iron oxidant generated from O_2. However, there are two other nonheme iron-based systems that carry out similar chemistry on gaseous alkanes, but with ^{t}BuOOH or Oxone as the source of oxidizing equivalents.[73,74] These are promising steps towards the functionalization of gaseous alkanes, but more work is needed to ascertain the nature of the high-valent iron oxidants implicated in these oxidations. The demonstration that **3** can hydroxylate *n*-butane not only provides a steppingstone towards our understanding of how metalloenzymes work but also highlights the potential such synthetic systems may hold.

2.4 Experimental

Materials and Methods

All reagents and solvents were purchased from commercial sources and used without further purification unless otherwise stated. The preparation and handling of air-sensitive materials were carried under an inert atmosphere using a glovebox. The complexes [Fe(Tp^{Ph2})($O_2CC(O)Ph$)] (**1a**) and [Fe(Tp^{Ph2})($O_2CC(O)CH_3$)] (**1b**) were prepared as previously reported.[30]

Physical Methods

UV-vis spectra were recorded on a Agilent Cary 60 UV-vis spectrometer. Gas chromatography (GC) product analyses were performed on a PerkinElmer Autosystem XL gas chromatograph (AT-1701, 30 m; DB-1, 30 m) equipped with a flame ionization detector. GC-mass spectrometry (MS) analyses were performed on a Agilent 7890A gas chromatograph (HP-5MS, 30 m) equipped with an Agilent 5975C mass detector in electron impact mode. NMR analyses were recorded on a Bruker Avance 500 spectrometer.

Product Analysis

Organic products were analyzed after reaction with oxygen via GC. After the reaction, the mixture was passed through a short silica column and eluted with tetrahydrofuran. A known concentration of naphthalene was introduced into the reaction mixture as an internal standard. Yields of the oxidized products were determined by a comparison to authentic standards.

Chapter 3: Characterization of a Series of Nonheme Iron-oxygen Intermediates Relevant to Dioxygen Activation

3.1 Introduction

Non-heme iron oxygenases catalyze an amazing array of oxidation reactions.[12,62,75,76] The first step in the activation of O_2 by these enzymes is usually the formation of an Fe(III)-superoxo species upon binding of O_2 to the Fe(II) center and subsequent electron-transfer.[12,61] Such species are well characterized in the enzymatic and synthetic heme literature,[77,78] but only recently have iron-superoxo species been reported in nonheme iron enzymes.[34–37] Of these limited examples, the mononuclear enzyme homoprotocatechuate 2,3-dioxygenase (2,3-HPCD) has been the most extensively characterized.[35,37]

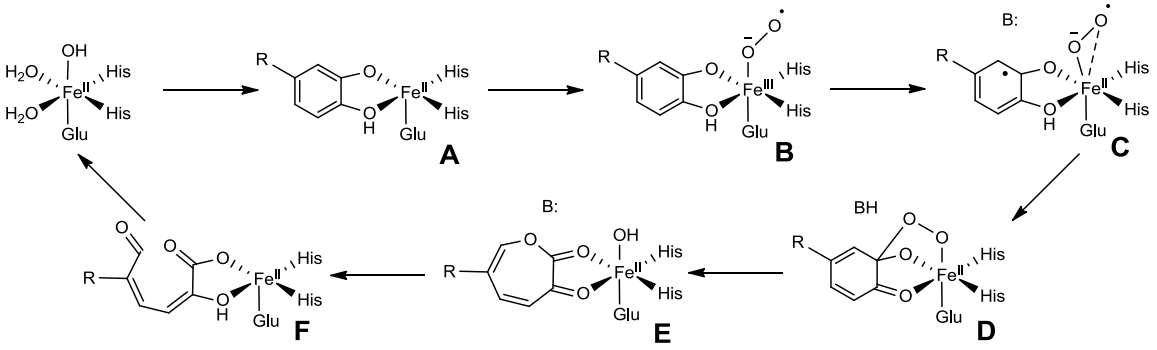

Scheme 3.1. Proposed mechanism for extradiol dioxygenases. Adapted from refs. 35 and 37.

Soaking crystals of 2,3-HPCD with a substrate analog, 4-nitrocatechol (4NC), which had previously been shown to slow the oxygen activation and insertion steps in the catalytic cycle,[79] provided crystals where multiple intermediates (**C, D, F**) were able to be trapped, providing amazing insight into the mechanism (Scheme 3.1).[37] One intermediate, **C**, was a side-on bound Fe-superoxo intermediate. This superoxo species was proposed to be an Fe(II)-superoxo species formed through electron transfer from the substrate, 4-nitrocatechol, to the iron center. It is proposed that species **C** is the reactive species which initiates oxygen attack on the substrate, through coupling of the incipient radicals, to form the alkylperoxo intermediate **D**. Subsequent Criegee rearrangement of **D** would result in O-O bond cleavage and insertion of an oxygen atom into the ring (**E**), eventually

leading to the ring-cleaved product (**F**).[37] Subsequent work, included the mutation of an active site histidine to asparagine (H200N), led to the detection and characterization of an Fe(III)-superoxo species with an $S = 2$ ground state formed from the antiferromagnetic coupling between the $S = 5/2$ Fe-center and the $S = 1/2$ superoxo radical (**B**).[35] The only synthetic nonheme iron-superoxo complexes thus far are both derived from diiron(II) precursors.[38,80] While mononuclear iron-superoxo complexes were lacking until recently,[39–41] there are many examples of well-characterized monomeric superoxo species containing other transition metals such as Cu, Ni and Cr.[81]

For the majority of enzymes, especially those containing a reducing co-substrate (e.g., α-ketoglutarate or tetrahydropterin), the superoxo species formed after coordination of O_2 to the Fe^{II} center is further reduced to form an Fe(IV)=O species which is responsible for H-atom abstraction (HAA) of the substrate. There are, however, a growing number of enzymes for which this mechanism is insufficient to explain the observed chemistry.[44,45] This has led to the proposal that substrate oxidation is actually initiated by the Fe(III)-superoxo intermediate. Such a mechanism has been proposed for isopenicillin *N* synthase (IPNS),[33] *myo*-inositol oxygenase (MIOX),[36] CloR,[46] and 2-hydroxyethyl phosphonate dioxygenase (HEPD).[47] The initial HAA by the ferric-superoxo species would invariably lead to the formation of an Fe(III)-hydroperoxo species, which is further involved in the subsequent oxidation of the substrate. The proposed mechanism for IPNS is shown in scheme 3.2 and highlights the initial HAA by a Fe(III)-superoxo species to form a Fe(III)-hydroperoxo intermediate.

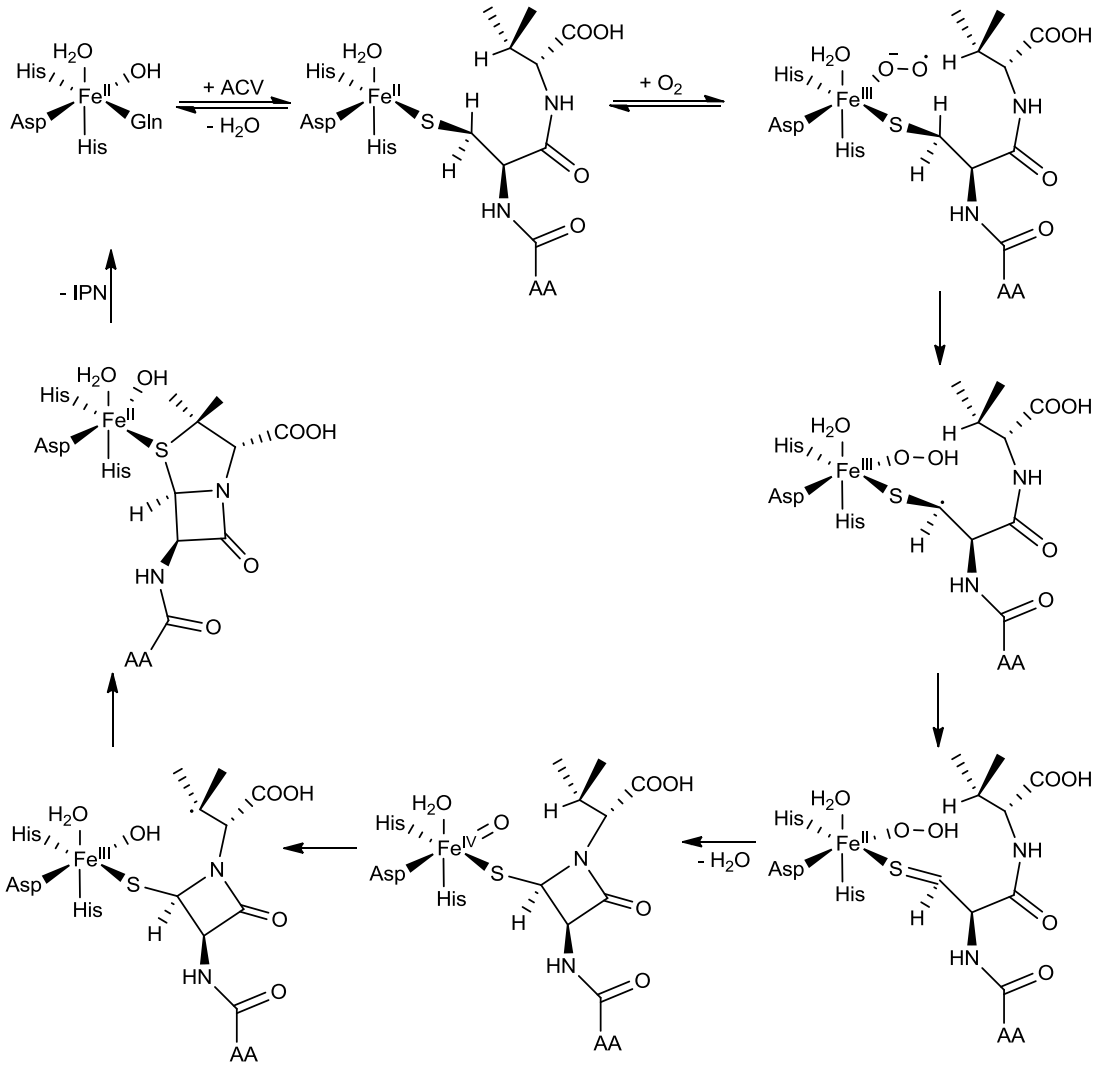

Scheme 3.2. Proposed mechanism for isopenicillin *N* synthase (IPNS). Adapted from ref. 45.

There are several well characterized synthetic Fe(III)-hydroperoxo complexes that, until recently, had exclusively been generated by addition of H_2O_2 to the Fe(II) precursor or protonation of a Fe(III)-peroxo species.[48–52] A recent report by Hikichi and Ogura showed the formation of a Fe(III)-hydroperoxo species generated from HAA of a substrate by a Fe(III)-superoxo species, the first such synthetic example of this transformation.[41]

In this chapter we report the characterization of the first mononuclear, synthetic, nonheme Fe(III)-superoxo species[39] and its conversation to both a Fe(III)-hydroperoxo species through HAA and a diferric-peroxo species through comproportionation.

3.2 Results and Discussion

3.2.1 Fe(III)-superoxo Intermediate

Treatment of 2,6-Bis(((S)-2-(diphenylhydroxymethyl)-1-pyrrolidinyl)methyl)pyridine (H_2BDPP) with NaH in CH_3CN and then with $FeCl_2$ forms a red solution of Fe(II)(BDPP) (**1**). Evaporation of the solvent affords a solid that yields dark red crystals of **1** upon recrystallization from CH_2Cl_2/pentane. Complex **1** exhibits two UV-vis absorption bands at 325 (sh, ε_M 1500 M^{-1} cm^{-1}) and 525 nm (ε_M 570 M^{-1} cm^{-1}) in THF. X-ray crystallography of **1** (Figure 3.1) reveals a mononuclear iron(II) complex with a distorted square pyramidal geometry (τ = 0.48).[82]

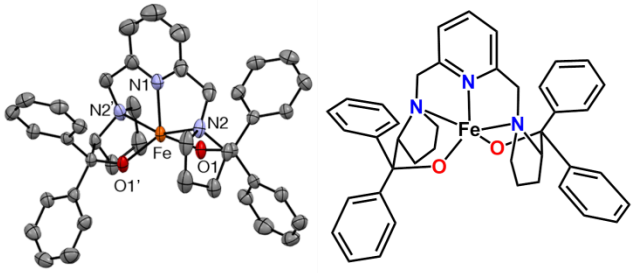

Figure 3.1. X-ray structure (left) and a schematic drawing (right) of Fe(BDPP) (**1**); hydrogen atoms not shown. Selected bond lengths (Å) and angles (°): Fe1−O1 1.927(2), Fe1−N1 2.100(4), Fe1−N2 2.271(3), O1−Fe1−O1' 123.03(16), N2−Fe1−N2' 151.81(18). Crystal structure data collected and solved by researchers at National Taiwan Normal University.[39]

The five-coordinate Fe(II) center of **1** would appear to be well set up to bind O_2. Indeed, bubbling of O_2 through a THF solution of **1** at -80 °C generates a bright yellow solution with an intense absorption band at 330 nm (ε_M 9400 M^{-1} cm^{-1}) (Figure 3.2) and an isosbestic point at 465 nm (Figure 3.2 inset). For comparison, the O_2 adduct of $[Fe^{II}_2(\mu\text{-}OH)_2(6\text{-}Me_3TPA)_2]^{2+}$ (6-Me_3TPA = tris(6-methylpyridyl-2-methyl)amine)

observed in CH_2Cl_2 at -80 °C exhibits a similarly intense UV band at 325 nm (ε_M 10300) and has been characterized to be an Fe(II)Fe(III)-superoxo complex.[38] Interestingly, bubbling of N_2 through the THF solution of **2** for 5 min at -80 °C regenerates **1**, showing that **2** is a reversible Fe−O_2 adduct. Several cycles of alternating N_2/O_2 purges can be achieved.

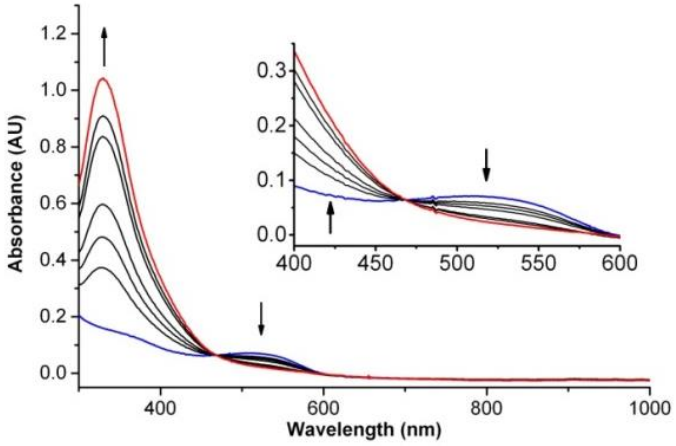

Figure 3.2. Formation of **2** (red line) at -80 °C by bubbling O_2 through a THF solution of **1** (0.1 mM) (blue line).

Excitation of **2** obtained with 413.1-nm irradiation reveals a resonance enhanced vibration at 1125 cm^{-1} (Figure 3.3), presumably arising from the bound O_2. Its frequency falls within the 1100-1200 cm^{-1} range found for the ν(O–O) features of other mononuclear metal-superoxo complexes (Table 3.1).[83–86] Hooke's Law predicts a downshift of 64 cm^{-1} for the ν(O–O) of the $^{18}O_2$ isotopomer. This downshift moves the ν(O–O) for **2** into a region obscured by a THF mode, but the corresponding experiment in d_8-THF shows a peak at 1062 cm^{-1}. Taken together, the observed frequency and 63-cm^{-1} downshift support a superoxo ligand for **2**. Given the pentadentate nature of BDPP and the reversibility of O_2 binding, it is likely that the superoxide is bound end-on, as deduced for the other complexes listed in Table 3.1.

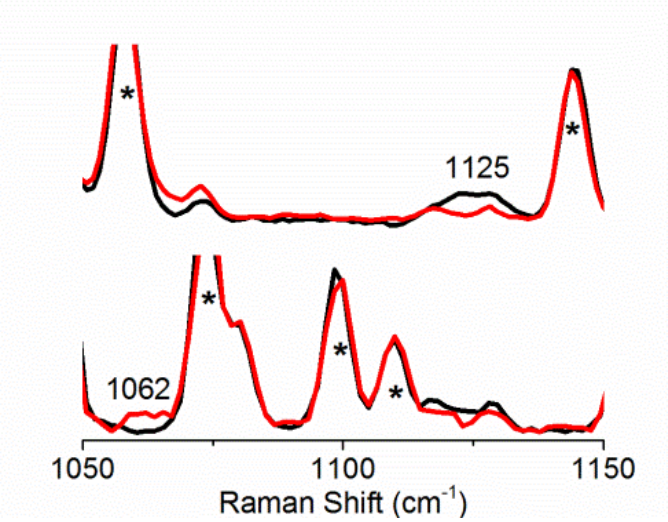

Figure 3.3. Resonance Raman spectra of **2** (λ_{ex} 413.1 nm, 30 mW, 77 K) prepared by bubbling O_2 into **1** (5 mM) in THF or d_8-THF at -80 °C. Top: black, $^{16}O_2$; red, $^{18}O_2$ in THF; bottom: black, $^{16}O_2$; red, $^{18}O_2$ in d_8-THF. Asterisks denote solvent peaks.

Table 3.1. Raman data for metal-superoxo complexes

Superoxo complexes	$\nu(^{16}O–^{16}O)$, cm^{-1}	$\nu(^{18}O–^{18}O)$, cm^{-1}	ref
2	1125	1062	39
$[Fe^{II}_2(\mu\text{-}OH)_2\text{-}(6\text{-}Me_3TPA)_2]^{2+} + O_2$	1310	1239	38
$[Cu^{II}(TMG_3tren)(\eta^1\text{-}O_2)]^+$	1117	1059	83
$[Cu^{II}(6\text{-}pivTPA)O_2]^+$	1130	1067	84
$[Ni^{II}(TMC)O_2]^+$	1131	1067	85
$[Cr^{III}(TMC)(\eta^1\text{-}O_2)(Cl)]^+$	1170	1104	86

Abbreviations used: 6-Me_3TPA = tris(6-methylpyridyl-2-methyl)amine; 6-pivTPA = (6-pivaloylamidopyridyl-2-methyl)-bis(6-methylpyridyl-2-methyl)amine; TMC = 1,4,8,11-tetramethylcyclam; TMG_3tren = 1,1,1-tris{2-[N2-(1,1,3,3-tetramethylguanidino)]ethyl}amine)

Working in collaboration with researchers from Carnegie Mellon University, further insight into the electronic structure of **2** has been gained from an analysis of its Mössbauer spectra. Figure 3.4 shows the 4.2 K spectra of **2** recorded in parallel applied fields B = 2.2 mT (A) and B = 45 mT (B). The spectrum of Figure 3.4B is typical of those observed for high-spin (S_1 = 5/2) Fe(III) species with a ground Kramers doublet that is magnetically uniaxial (such as the $M_S = \pm 5/2$ doublet which has $g_z >> g_x, g_y$). The isomer shift, δ = 0.58(3) mm/s, of the dominant species (the red solid line represents 85% of the Fe) is strongly indicative of high-spin Fe(III). The analysis of the spectra is complicated by the fact that there is also the superoxo ligand, which has its own S = 1/2 spin. If **2** would represent an exchange-coupled Fe(III)-O_2^- pair like that for the HPCD superoxo intermediate,[35] the ground state would have integer spin S = 2 or S = 3, corresponding to antiferromagnetic or ferromagnetic coupling of the two paramagnetic components, respectively.

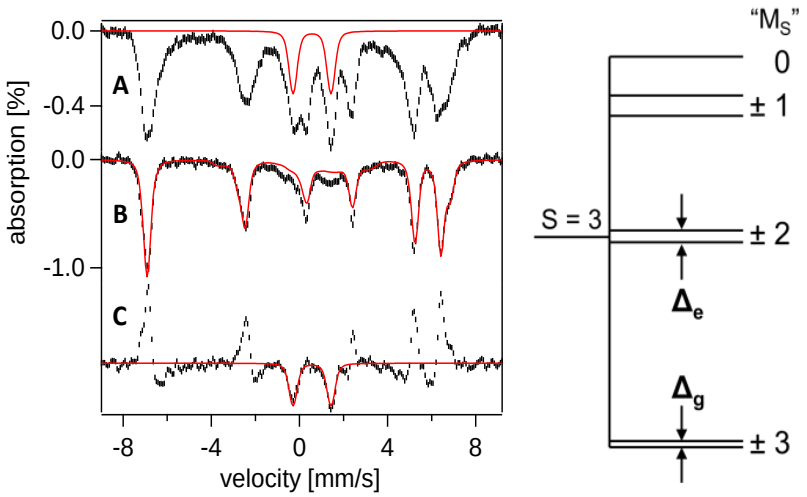

Figure 3.4. *Left*: 4.2 K Mössbauer spectra of **2** recorded in parallel applied fields B = 2.2 mT (A) and B = 45 mT (B). (C) Difference spectrum "2.2 mT minus 45 mT". The red line in (A) outlines a quadrupole doublet that represents ≈ 10% of the Fe attributed to **2**. The red line in (B) is a spectral simulation for **2** and represents 85% of the Fe. The red line represents two similar S = 3 species (parameters of the minority species are given in italics): 53(*32*)%, D = -1.2(*-1.2*) cm^{-1}, E/D = 0.08(*0.08*), δ = 0.58(*0.58*), ΔE_Q = -1.7(*-1.5)* mm/s, η ≈ 0.5(*0.5*), $A_z/g_n\beta_n$ = -13.8 (*-14.3)* T, (because $\langle S_{x,y} \rangle \approx 0$ the spectra are insensitive A_x and A_y). *Right*: Schematic splittings of the S = 3 multiplet. Mössbauer spectra collected and analyzed by researchers at Carnegie Mellon University.

Further Mössbauer analysis of **2** in 2-MeTHF, a glassing solvent, provided unequivocal evidence for the determination of the ground spin state as S = 3 (Figure 3.5). This ferromagnetic coupling between the S = 5/2 Fe(III) center and the S = 1/2 superoxo radical is the opposite to what has been seen in HPCD. In HPCD, the ground spin state is S = 2, through antiferromagnetic coupling.[35] The Mössbauer splitting pattern associated with this electronic doublet can be obtained from the properties of the M_S = ±3 doublet: we have to scale $B_{int,z}$ of the spectrum associated with the M_S = ± 3 doublet by 2/3, the ratio of the spin expectation values along z. The excellent match of the simulation with the experimental spectrum shows that the electronic ground state has indeed S = 3; of course, we do not have to scale as the S = 3 spin Hamiltonian produces the correct

splitting automatically once E/D is set to ≈ 0.02. (NB: For an assumed S = 2 ground multiplet the splitting of the two spectra would scale by ½ rather than 2/3). The intensity associated with the (blue) M_S = ±2 spectrum requires a Boltzmann factor that is produced for D = - 1.1 cm^{-1}. The same D-value yields the correct decrease of the intensities of the nuclear Δm = 0 lines with increasing applied field.

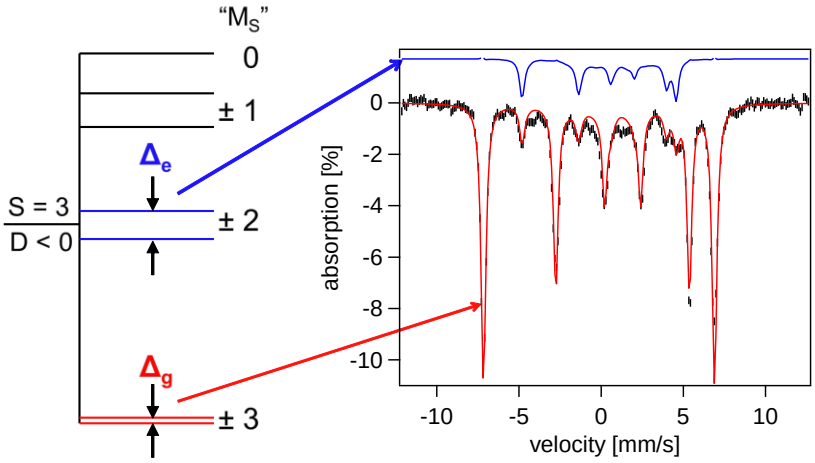

Figure 3.5. *Left*: Schematic level splitting of the S = 3 multiplet for D < 0 and B = 0. Δ_g and Δ_e are the splittings of the M_S = ± 3 and M_S = ± 2 doublets, respectively. *Right*: Mössbauer spectrum of **2** recorded at 4.2 K in a parallel field B = 0.12 T. The major six-line pattern originates from the M_S = ± 3 ground state; the subcomponent drawn in blue is associated the excited M_S = ±2 levels. Mössbauer spectra collected and analyzed by researchers at Carnegie Mellon University.

Having assigned **2** as a Fe(III)-superoxo species, we decided to test the notion that an Fe(III)-superoxo moiety can abstract an H-atom from a substrate C–H bond. This question was examined by adding an excess of 9,10-dihydroanthracene (DHA, $D_{C–H}$ 78 kcal/mol[87]) to a THF solution of **2** at -70 °C, which resulted in the decay of the characteristic 330-nm band of **2**. Anthracene was formed in 90% yield relative to the amount of **2**, and neither anthrone nor anthraquinone were found as byproducts. The reaction followed first-order kinetics in the presence of excess DHA and a plot of the pseudo first-order rate constants against the concentration of DHA gave a straight line,

from which a second order rate constant k_2 of 0.005 M^{-1} s^{-1} was obtained. When DHA-d_4 was used as substrate, a kinetic isotope effect of 7 was observed, showing that C–H bond cleavage is involved in the rate determining step (Figure 3.6).

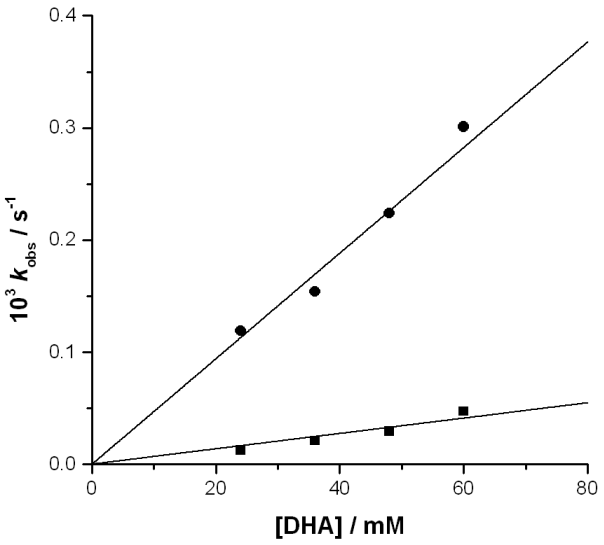

Figure 3.6. Plot of k_{obs} values versus substrate concentration for the reaction of 0.6 mM **2** with DHA (•) and DHA-d_4 (■) at -70 °C. KIE = 7. Rate data collected by researchers at National Taiwan Normal University.

We compared our data with those of the two other metal-superoxo complexes for which the kinetics of intermolecular C–H bond cleavage has been studied. After adjustment for differences in temperature and substrate D_{C-H} values, it appears that **2** has a C–H bond cleaving rate comparable to that of $[Cr^{III}(TMC)O_2(Cl)]^+$ (k_2 = 0.17 $M^{-1}s^{-1}$ at -10 °C for DHA oxidation)[86] but slower than that of $[Cu^{II}(6\text{-pivTPA})O_2]^+$ (k_2 = 0.19 $M^{-1}s^{-1}$ at -125 °C for 1-benzyl-1,4-dihydronicotinamide ($D_{C–H}$ 71 kcal/mol) oxidation).[84] In addition, the latter two complexes were found to exhibit nonclassical KIE values for C–H bond cleavage of 50[86] and 12,[84] respectively, that may implicate hydrogen tunneling. What the differences among the KIE values indicate about the nature of the superoxo ligand and how that affects HAA should be an interesting topic for future work. In addition, as observed for $[Cr^{III}(TMC)(\eta^1\text{-}O_2)(Cl)]^+$,[86] we also found a 1:1 reaction

stoichiometry for **2** consumed and anthracene formed, indicating that **2** provides two oxidizing equivalents for the oxidation of DHA. This result suggests that the Fe(III)-OOH species, presumably formed upon HAA of DHA by **2**, must react further with the nascent DHA radical.

Table 3.2. Spectroscopic and reactivity data for Fe-superoxo complexes

	2	**$[Fe^{III}(TAML)(\eta^2\text{-}O_2)]^{2-}$**	**$Fe^{III}(L^{Ph})(Tp^{Me2})(\eta^1\text{-}O_2)$**
Ox State	3+	3+	3+
Fe Spin State Ground State (coupling)	5/2 (HS) 3 (ferromagnetic)	3/2 (IS) 1 (antiferromagnetic)	1/2 (LS) 0 (antiferromagnetic)
ν(O-O) (Δ18)	1125 (-63)	1260 (-77) [a]	1168 (-78)
Binding Mode	End-on	Side-on	End-on
C-H HAT (Rate) [KIE]	DHA (0.007) [7] -70°C	No Rxn	No Rxn
O-H HAT (Rate) [KIE]	TEMPOH (29.2) [7] -80°C	Phenol (0.3) [-] -20°C	AZADOL (0.002) [18] -60°C
Aldehydes (Rate)	No Rxn	2-PPA (0.37) 5°C	No Rxn
ref	39	40	41

[a] Value obtained by IR.

Abbreviations used: TAML = tetraamido macrocyclic ligand, 3,3,6,6,9,9-hexamethyl-2,5,7,10-tetraoxo-3,5,6,7,9,10-hexahydro-2*H*-benzo[*e*][1,4,7,10]tetraazacyclo-tridecine-1,4,8,11-tetraide); Tp^{Me2} = hydrotris(3,5-dimethylpyrazol-1-yl)borate; L^{Ph} = hydrogen methylbis(1-methyl-2-imidazolyl)-(phenyl)borate; DHA = dihydroanthracene; TEMPOH = 1-hydroxy-2,2,6,6-tetramethylpiperidine; AZADOL = 2-hydroxy-2-azaadamantane; 2-PPA = 2-phenylpropionaldehyde.

Since the isolation and characterization of **2**, two more Fe-superoxo species have been characterized, including one crystallographically.[40,41] The relevant spectroscopic and reactivity data is shown in Table 3.2. While the three species shown in Table 3.2 share the same Fe-oxygen moiety, their spectroscopic and reactivity features are markedly different. All three species have an Fe(III) center, but the spin state of the iron center is different for each. This appears to have an influence on the reactivities of these species as only **2** was found able to oxidize C-H bonds, albeit only those with low BDE

values and the reaction proceeds very slowly. All three species were found to be reactive towards O-H bonds but show drastically different rates of reaction spanning over four orders of magnitude even without taking temperature into account. These differences in reactivity may be attributed to the fact that only **2** contains a high-spin iron center that is ferromagnetically coupled to the superoxo radical, while the other two complexes are intermediate- and low-spin species with antiferromagnetic coupling between the iron center and the superoxo radical. The high-spin nature of the Fe center in **2** is the same as that seen for the enzymes HPCD,[35] CDO[34] and MIOX,[36] of which the Fe(III)-superoxo species of MIOX is proposed to perform the initial HAA of the substrate myo-inositol. While perhaps akin to comparing apples with oranges, one can draw a comparison of the differences in spin-state and reactivity of these Fe(III)-superoxo species to those of Fe(IV)=O species where it is proposed that the high-spin variant should be more reactive than the low-spin species.[65] Of interest is the fact that only the TAML-based species was found reactive in nucleophilic oxidation reactions. This unique reactivity may be attributed to the fact that the TAML ligand is tetraanionic and thus the Fe center would be much more electron rich than the Fe centers in the other species, which contain dianionic ligands.

3.2.2 Hydroperoxo and Diferric-peroxo Intermediates Derived from a Common Precursor

The formation of anthracene in a 1:1 reaction stoichiometry with **2** indicates that **2** provides two oxidizing equivalents; the first coming from the initial HAA by **2** and the second perhaps coming from the nascent Fe(III)-hydroperoxo species. This Fe(III)-hydroperoxo species is presumably formed upon initial HAA, and subsequently reacts further with the DHA radical to provide anthracene as the product. In an attempt to trap the species formed from initial HAA, we have employed TEMPOH, which possesses a weak O-H bond (BDE = 70 kcal/mol) and whose one-electron oxidized product is stable. Addition of TEMPOH to a solution of **2** in THF at -80 °C led to rapid decay of the characteristic feature at 330 nm attributed to **2** and the growth of a new feature at 460 nm (ε_M 2200 M^{-1} cm^{-1}) (Figure 3.7), with an isosbestic point at 425 nm. Fitting the decay of the 330 nm band of **2** in the presence of excess TEMPOH gave a second-order rate

constant of 29 M^{-1} s^{-1} (Figure 3.8). EPR taken of the reaction mixture after complete decay of **2** provided a strong signal at $g = 2$, indicative of an organic radical (Figure 3.9).

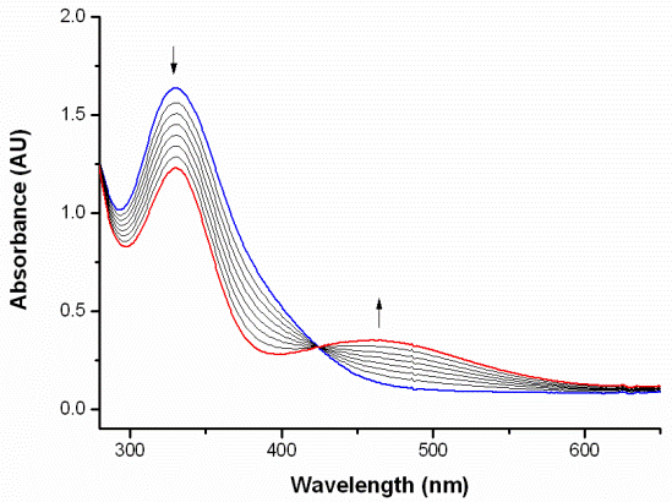

Figure 3.7. UV-Vis spectral change for the reaction of **2** (0.2 mM) with TEMPOH (2 mM) in THF at -80 °C.

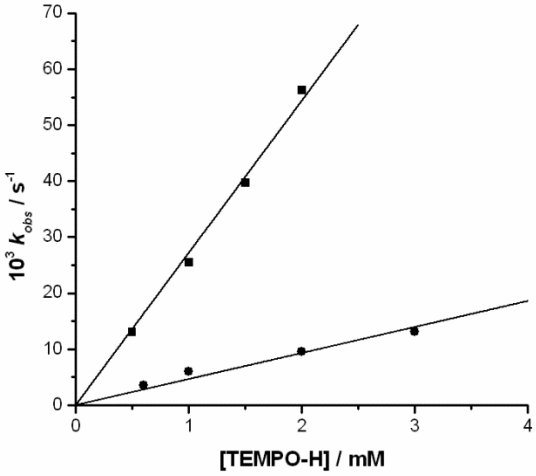

Figure 3.8. Plot of k_{obs} values versus substrate concentration for the reaction of 0.2 mM **2** with TEMPOH (■) and TEMPO-D (•). Rate data collected by researchers at National Taiwan Normal University.

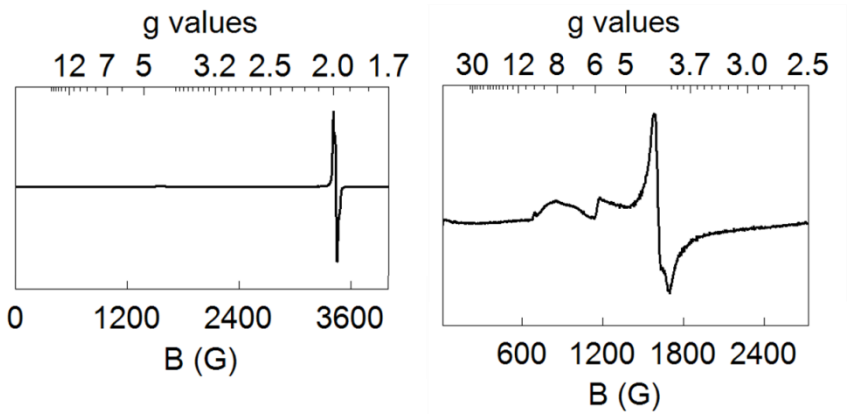

Figure 3.9. Left) 2.4 K perpendicular-mode EPR spectra at the end of the reaction between of **2** with TEMPOH. **Right)** Zoom in of the g = 4.21 species obtained at the end of reaction. EPR data collected by researchers at Carnegie Mellon University.

Integration of this signal showed that TEMPO$^{\cdot}$ was formed in nearly quantitative yield (97%). The use of TEMPOD gave a KIE of 7 indicating that the cleavage of the O-H bond in TEMPOH is the rate determining step. Another signal is found in the EPR spectrum at g = 4.21, a value indicative of a HS Fe(III) species (Figure 3.9). This new intermediate (**3**) is proposed to be an Fe(III)-hydroperoxo species formed through direct HAA from DHA and TEMPOH. A similar transformation was proposed for a recently characterized Fe(III)-superoxo complex.[41] The addition of AZADOL (2-hydroxy-2-azaadamantane) to the Fe(III)-superoxo complex $Fe^{III}(L^{Ph})(Tp^{Me2})(\eta^1\text{-}O_2)$ led to the growth of a new absorption band at 542 nm with resonance Raman features at 778 and 598 cm^{-1}, corresponding to the O-O and Fe-O vibrations, respectively.[41]

Excitation of **3** at 514.5 nm revealed a resonance-enhanced vibration at 841 cm^{-1} which is partially obscured by a mode from the solvent. This vibration becomes clear upon the use of $^{18}O_2$ where the vibration downshifts to 794 cm^{-1} (Figure 3.10). This shift (47 cm^{-1}) is in excellent agreement with the value obtained using Hooke's Law, (48 cm^{-1}) for an O-O vibration. We assign this vibration to the ν(O-O) of the bound end-on hydroperoxo moiety. Its frequency falls outside the range (780-805 cm^{-1}) of the more numerous low-spin Fe(III)-hydroperoxo species but is in excellent agreement with the frequencies seen for high-spin Fe(III)-hydroperoxo species (830-890 cm^{-1}) (Table 3.3).

Another resonance-enhanced vibration is observed at 503 cm^{-1}, which downshifts to 485 cm^{-1} with the use of $^{18}O_2$ (Figure 11). This frequency is well below the reported values for low-spin Fe(III)-hydroperoxo complexes (598-632 cm^{-1}), but within the wide range of values for the high-spin set (419-676 cm^{-1}) (Table 3.3).We assign this vibration to the ν(Fe-O) as the experimental ^{18}O shift (18 cm^{-1}) is in good agreement with the value obtained using Hooke's Law (22 cm^{-1}). The use of TEMPOD did not shift either the ν(O-O) or ν(Fe-O) vibrations in the rR spectrum (Figure 3.12). While the heavier deuterium atom has the potential to cause a shift in the vibration to lower energy, it is not uncommon to see no shift upon incorporation of deuterium (Table 3.3).

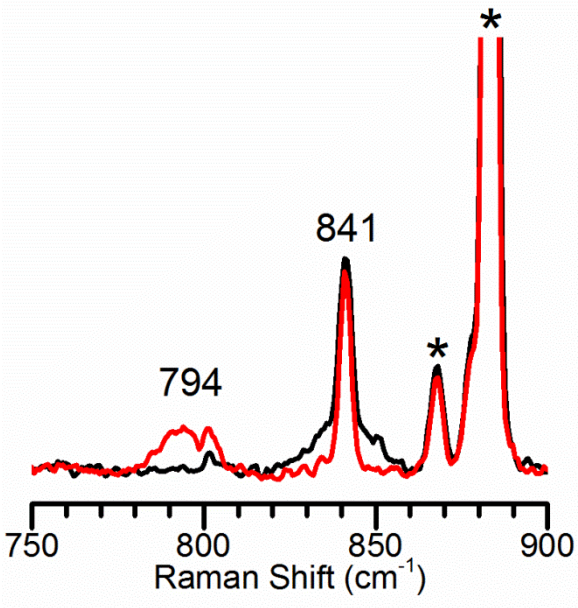

Figure 3.10. Resonance Raman spectra of **3** (λ_{ex} 514.5 nm, 60 mW, 77 K) Black, $^{16}O_2$; Red, $^{18}O_2$ in THF. Asterisks denote solvent peaks.

Table 3.3. Raman Data for Metal-Hydroperoxo Complexes

	Hydroperoxo Complexes	ν(Fe-O), cm^{-1} ($\Delta^{18}O$) [$\Delta^{2}H$]	ν(O-O), cm^{-1} ($\Delta^{18}O$) [$\Delta^{2}H$]	ref
HS	**3**	503 (-18) [0]	841 (-47) [0]	This work
HS	$[Fe(TMC)(OOH)]^{2+}$	676 (-24) [-1]	870 (-50) [-1]	[48]
HS	E114A SOR	567 (-4)	838 (-23)	[88]
HS	oxyhemerythrin	503 (-24) [-3]	844 (-48) [+4]	[89]
HS	$[Fe(cyclam\text{-}PrS)(OOH)]^{2+}$	419 (-19)	891 (-35) [0]	[49]
LS	$[Fe(N_4Py)(OOH)]^{2+}$	632*	790 (-44)	[50]
LS	$[Fe(H\text{-}TPEN)(OOH)]^{2+}$	625 (-23)	801 (-51) [0]	[51]
LS	$[Fe(Me\text{-}TPEN)(OOH)]^{2+}$	617 (-17)	796 (-45) [1]	[51]
LS	$[Fe(L^2)(OOH)]^{2+}$	608 (-24) [-5]	804 (-44)	[90]
LS	$[Fe(L^3)(OOH)]^{2+}$	620 (-22) [-6]	804 (-43)	[90]
LS	$[Fe(TPA)(OOH)]^{2+}$	626* (-16) [-5]	803 (-44)	[52]
LS	$[Fe(L^{Ph})(Tp^{Me2})(OOH)]$	598 (-25)	778 (-40)	[41]

* = Observed feature for the coupled Fe-OOH mode.

Abbreviations used: TMC = 1,4,8,11-tetramethylcyclam; SOR = superoxide reductase; cyclam-PrS-H = 1-(3'mercaptopropyl)-1,4,8,11-tetraazacyclotetradecane; N4Py = N,N-bis(2-pyridylmethyl)-N-bis(2-pyridyl)methylamine; H-TPEN = N,N',N'-tris(2-pyridylmethyl)ethane-1,2-diamine; Me-TPEN = N-methyl-N,N',N'-tris(2-pyridylmethyl)ethane-1,2-diamine; TPA = tris(2-pyridylmethyl)amine; Tp^{Me2} = hydrotris(3,5-dimethylpyrazol-1-yl)borate; L^{Ph} = hydrogen methylbis(1-methyl-2-imidazolyl)-(phenyl)borate.

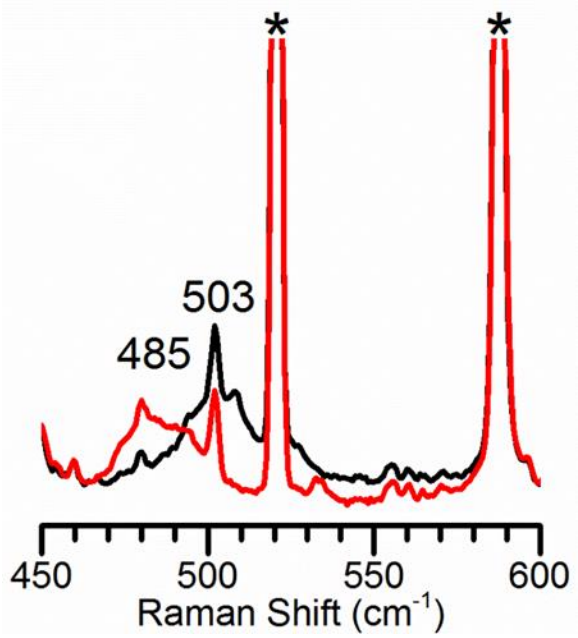

Figure 3.11. Resonance Raman spectra of **3** (λ_{ex} 514.5 nm, 60 mW, 77 K) Black, $^{16}O_2$; Red, $^{18}O_2$ in THF. Asterisks denote solvent peaks.

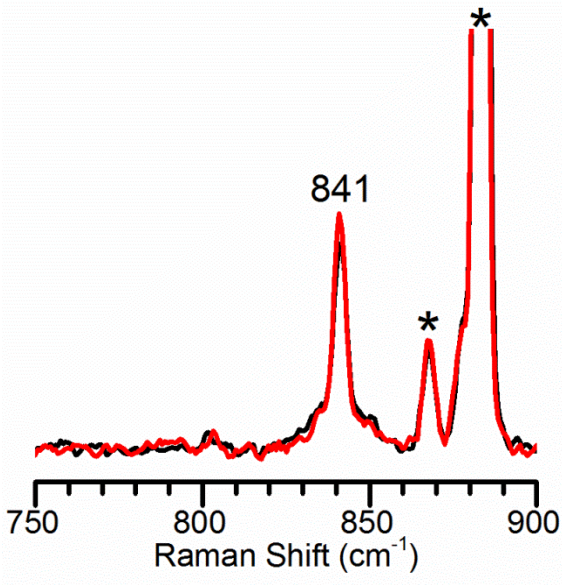

Figure 3.12. Resonance Raman spectra of **3** (λ_{ex} 514.5 nm, 60 mW, 77 K) Black, OOH; Red, OOD in THF. Asterisks denote solvent peaks.

The low ν(Fe-O) value for **3** provides insight into the potential outcome of a reaction between **3** and added protons.[58,91] The value of 503 cm^{-1} is similar to the values obtained for oxyhemerythrin[89] and SOR[88], both of which undergo Fe-O bond cleavage during their respective reactions, but substantially lower than the value for (TMC)FeIII-hydroperoxo,[48] which was found to undergo O-O bond cleavage upon the addition of acid. We would thus expect **3** to undergo Fe-O bond scission upon the addition of acid to form hydroperoxide as the product, like what was seen for the SOR-model, [Fe(cyclam-PrS)(OOH)].[49] Upon addition of the strong acid trifluoromethanesulfonic acid (HOTf), the feature at 460 nm immediately disappeared with no new features observed during the decay. While not definitive proof, the lack of any additional features during decay points towards the assumption that **3** will undergo Fe-O bond cleavage upon the addition of proton. Further experiments need to be conducted to see if H_2O_2 is produced and to more rigorously determine whether the Fe-O or O-O bond is cleaved.

In agreement with the rR data, the Mössbauer spectra of **3** (Figure 3.13) contain a high-spin Fe(III) majority species, outlined by the red traces, that accounts for ca 75% of the iron in the sample. The isomer shift of $\delta = 0.44$ mm/s is indicative of a $S = 5/2$ Fe(III) center. We have simulated the spectra of Figure 3.13 using the standard $S = 5/2$ spin Hamiltonian.

Simulations show that the ^{57}Fe magnetic hyperfine tensor of **3**, like its counterpart in the superoxo species **2**, is anisotropic. Again, $A_{iso}/g_n\beta_n = -19.6$ T is quite small and comparable to the $A_{iso}/g_n\beta_n = -18.8$ T of the Fe(III)-superoxo complex. These observations suggest that the small A_{iso} value is a property of the BDPP ligand.

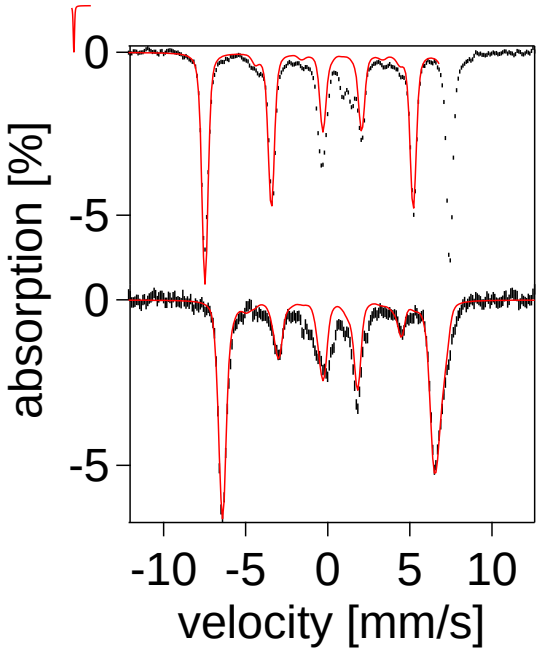

Figure 3.13. 4.2 K Mössbauer spectra of Fe^{III} hydroperoxo complex, **3**, recorded for B = 0.12 T (A) and 7.5 T (B). The red lines are spectral simulations based on the *S* = 5/2 spin Hamiltonian. The theoretical curve is drawn to represent 75% of the Fe in the sample. Mössbauer spectra collected and analyzed by researchers at Carnegie Mellon University.

Combined, the data provides strong evidence for assigning species **3** as a HS Fe(III)-hydroperoxo intermediate, which was generated by a Fe(III)-superoxo species performing HAA on an exogenous substrate. This transformation provides experimental evidence for the proposed first oxidation step by some enzymatic Fe(III)-superoxo species,[45] and is just the second such example by an O_2-derived superoxo intermediate (Scheme 3.3).[41]

Warming of a solution of **2** from -80 °C to -60 °C elicits a color change from bright yellow to deep purple with a new absorption band that appears at 560 nm (ε_M 1000 M^{-1} cm^{-1}) and with an isosbestic point at 430 nm (Figure 3.14). This new species, **4**, could also be formed directly by bubbling O_2 into a solution of Fe(II) complex at -40 °C. Purging a solution of **4** with N_2 at any temperature does not elicit a color change, showing that species **4** is an irreversible Fe-O_2 adduct.

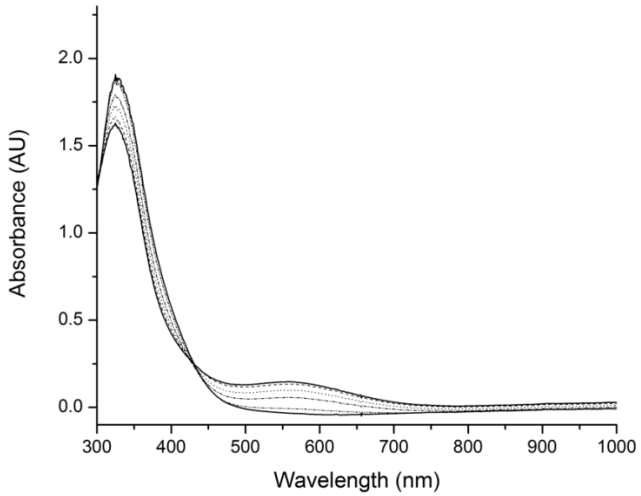

Figure 3.14. UV-Vis spectral change for the reaction of **2** (0.2 mM) in THF at -60 °C.

Excitation of the EPR-silent **4** at 514.5 nm revealed a resonance-enhanced vibration at 839 cm^{-1}, which downshifts to 793 cm^{-1} upon the use of $^{18}O_2$ (Figure 3.15). A frequency of 839 cm^{-1} is consistent with either a Fe-oxo or Fe-peroxo species (Table 3.4). However, the experimental isotopic shift of 46 cm^{-1} is very close to the value obtained using Hooke's Law for an O-O stretch, (48 cm^{-1}); thus we assign this feature to the O-O stretch of a Fe-bound peroxo species. The O-O vibration for **4** is comparable to the values obtained for a series of end-on unsupported dicobalt[92] and dicopper species while being a bit lower than those reported for the numerous end-on bridged diiron species (Table 3.4).

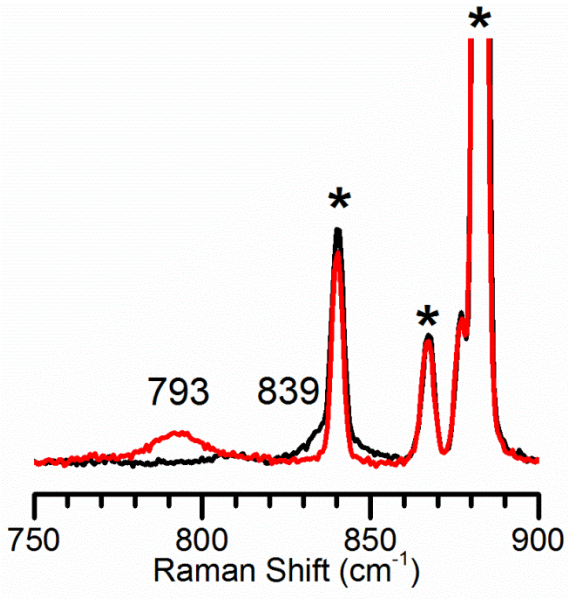

Figure 3.15. Resonance Raman spectra of **4** (λ_{ex} 514.4 nm, 60 mW, 77 K) Black, $^{16}O_2$; Red, $^{18}O_2$ in THF. Asterisks denote solvent peaks.

Table 3.4. Raman Data for Metal-Peroxo Complexes

	Peroxo Complexes	$\nu(^{16}O\text{-}^{16}O)$, cm^{-1} ($\Delta^{18}O$)	ref
unsupported	**4**	839 (46)	This work
unsupported	$[Cu_2(\mu\text{-}O_2)(L^{H,Bn})_2]^{2+}$	839/829 (46)	[93]
unsupported	$[Cu_2(\mu\text{-}O_2)(m\text{-}Xyl^{N3N4})]^{2+}$	832 (51)	[94]
unsupported	$[Cu_2(\mu\text{-}O_2)(m\text{-}Xyl^{N4N4})]^{2+}$	826 (44)	[94]
unsupported	$[Cu_2(\mu\text{-}O_2)(tmpa)_2]^{2+}$	832 (44)	[95]
unsupported	$[Cu_2(\mu\text{-}O_2)(tmpa)(2,6\text{-}PCA)]^{-}$	832 (44)	[96]
end-on, bridged	$[Fe_2(\mu\text{-}O_2)(NO_3)_2(HPTB)]^{+}$	895 (41)	[97]
end-on, bridged	$[Fe_2(\mu\text{-}O_2)(\mu\text{-}O_2CCH_2Ph)_2(Tp^{iPr2})_2]$	888 (46)	[29]
end-on, bridged	$[Fe_2(\mu\text{-}O_2)(\mu\text{-}O_2CPh)_2(Tp^{iPr2})_2]$	876 (49)	[28]
end-on, bridged	$[Fe_2(\mu\text{-}O_2)(\mu\text{-}O)(BnBQA)_2]$	854 (47)	[98]
end-on, bridged	$[Fe_2(\mu\text{-}O_2)(\mu\text{-}O)(6\text{-}Me_3\text{-}TPA)_2]^{2+}$	848 (46)	[99]
end-on, bridged	RNR	870 (46)	[100]
end-on, bridged	Ferritin	851 (51)	[101]
end-on, bridged	Δ^9 desaturase	898 (53)	[102]
end-on, bridged	hDOHH	855 (44)	[103]
side-on	$[Fe(TMC)(O_2)]^{+}$	826 (41)	[48]
side-on	$[Fe(N_4Py)(O_2)]^{+}$	827 (46)	[104]
side-on	$[Fe(tmpIm)(O_2)^{-}$	807 (49)	[105]
side-on	E47A SOR	850 (48)	[106]

Abbreviations: $L^{H,Bn}$ = tris(N-benzylaminoethyl)amine; tmpa = tris(2-pyridylmethyl)amine; PCA = N,N'-bis(2,6-diisopropylphenyl)-2,6-pyridinedicarboxamide; HPTB = N,N,N',N'-tetrakis(2-benzimidazolylmethyl)-2-hydroxy-1,3-diaminopropane; Tp^{iPr2} = hydrotris(3,5-diisopropylpyrazol-1-yl)borate; BnBQA = N-benzyl-N,N-bis(2-quinolinylmethyl)amine; 6-Me_3TPA = tris(6-methylpyridyl-2-methyl)amine; RNR = ribonucleotide reductase; hDOHH = human deoxyhypusine hydroxylase; TMC = 1,4,8,11-tetramethylcyclam; N_4Py = N,N-bis(2-pyridylmethyl)-N-bis(2-pyridyl)methylamine; tmpIm = 5,10,15-trismesityl-20-(2-nitrophenyl)porphyrin; SOR = superoxide reductase.

Mössbauer spectroscopy provided further insight into the nature of **4**. A broad quadrupole doublet with an isomer shift of $\delta = 0.47$ mm/s was seen (Figure 3.16). The isomer shift and quadrupole doublet are indicative of a pair of antiferromagnetically coupled high-spin iron centers. The broadness of the doublet could indicate two slightly inequivalent iron centers. Combined with the rR data, we assign species **4** as an end-on diferric-peroxo species. We assign the peroxo moiety to be bound end-on because of the pentadentate nature of the BDPP ligand. Of interest is the fact that **4** constitutes the first well-characterized, nonheme, unsupported diferric-peroxo species.

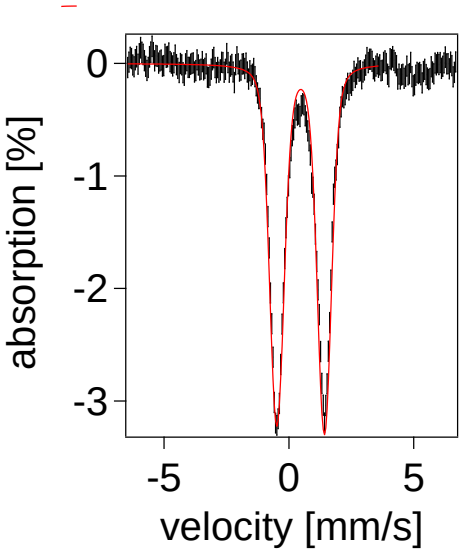

Figure 3.16. 4.2 K Mössbauer spectra of complex **4**, recorded for B = 0. The red line is a spectral simulation based on the S = 5/2 spin Hamiltonian. The theoretical curve is drawn to represent 80% of the Fe in the sample. Mössbauer spectra collected and analyzed by researchers at Carnegie Mellon University.

Comparison of the rR ν(O-O) values for **3** and **4** show that the two values, 841 and 839 cm^{-1}, respectively, are incredibly similar. As this is the first hydroperoxo/end-on peroxo pair generated from the same ligand, we do not know if this observation is unique or a fixture of this type of pair. We can compare our results to similar systems comparing a hydroperoxo species to a substituted peroxo species. $[Fe^{III}(TPA)(OOH)]^{2+}$ and $[Fe^{III}(TPA)(OO^{t}Bu)]^{2+}$ show ν(O-O) values which are of similar frequencies, 803 and 796

cm^{-1} respectively.[52,107] This was also seen in a set of Cu-peroxo species, but their analysis was complicated by the presence of multiple peaks in the ν(O-O) region, which were assigned to varying amounts of O-O bond contribution in a mixed O-O/C-O/C-C vibration.[108]

The proposed mechanism for the formation of **4** from **2** is shown in Scheme 3.3. We propose that, at higher temperatures, the equilibrium between **2** and the starting Fe(II) species (**1**) is shifted towards **1**, thus allowing species **2** to be trapped by **1** in solution forming species **4**. The proposed mechanism is similar to that proposed for diferric-peroxo species formed upon oxygenation of Fe(II)-porphyrins.[109] While the diferric porphyrin complexes were found to undergo O-O bond scission to form an Fe(IV)=O species, thus far we have been unsuccessful in obtaining any evidence for such a transformation in the decay/activation of **4**.

3.3 Summary

To summarize, we have generated the first synthetic example of a mononuclear Fe(III)-superoxo complex in a nonheme ligand environment, providing a model complex with which to compare corresponding complexes that have been trapped, or are likely to occur, in the catalytic cycles of nonheme iron oxygenases. The demonstration that **2** can oxidize DHA at -70 °C supports the mechanistic notion that Fe(III)-O_2^- species can carry out the HAA from a substrate C-H bond that is necessary for the initiation of the 4-e^- oxidation of substrates by nonheme iron enzymes.

Subsequently, we have generated both a Fe(III)-hydroperoxo (**3**) and diferric-peroxo (**4**) species from the above mentioned Fe(III)-superoxo precursor (**2**), providing evidence for the central role Fe-superoxo species play in oxygen-activation chemistry.

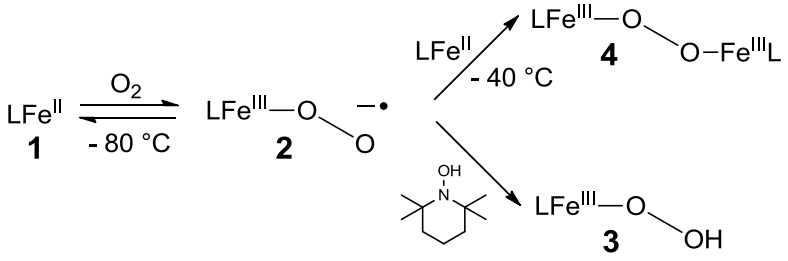

Scheme 3.3. Proposed mechanisms for the formation of **3** and **4** from **2**.

Table 3.5. Summary of Species Characterized in this Chapter

	Superoxo (**2**)	Hydroperoxo (**3**)	Peroxo (**4**)
Ox State	3+	3+	3+, 3+
Fe Spin State	5/2 (HS)	5/2 (HS)	5/2 (HS)
λ_{max}, nm (ε_M, M^{-1} cm^{-1})	330 (9400)	460 (2200)	560 (1000)
ν(O-O), cm-1 ($\Delta^{18}O$)	1125 (- 63)	841 (- 47)	839 (- 46)
Mössbauer, mm/s	0.58	0.44	0.47
Binding-Mode	End-On	End-On	End-on, unsupported

3.4 Experimental

Materials and Methods

All manipulations of Fe Complexes were performed under nitrogen using standard Schlenk techniques. All chemicals were of analytical or spectroscopic grade and purchased from commercial sources and used without further purification. 2,6-Bis(((S)-2-(diphenylhydroxymethyl)-1-pyrrolidinyl)methyl)pyridine (H_2BDPP) and 9,10-dihydroanthracene-d_4 were synthesized according to literature procedures.[110] [Fe^{II}(BDPP)] (**1**) was synthesized by reacting a mixture of NaH (0.0120 g, 0.5 mmol), H_2BDPP (0.1220 g, 0.2 mmol) and $FeCl_2$ (0.0253 g, 0.2 mmol) in 15 mL CH_3CN in a 100-mL Schlenk flask. The suspension solution was stirred at room temperature for 16 h and then filtered; the filtrate was concentrated under vacuum. Adding hexane (3 × 50 mL) to the concentrated filtrate resulted in the precipitation of a red residue of **1**. After filtration, the residue of **1** was dried under vacuum and redissolved in CH_2Cl_2 (10 mL). Complex **1** was then recrystallized by slow diffusion of pentane into the CH_2Cl_2 solution of **1** at room temperature. Red crystals of **1** were obtained over three days in 55% yield (0.7290 g). UV/vis (CH_3CN): 325 nm (1450 M^{-1} cm^{-1}), 530 nm (570 M^{-1} cm^{-1}). Anal. Calcd for [Fe(BDPP)]•0.5CH_2Cl_2 or $C_{41.5}H_{42}ClFeN_3O_2$: C, 70.59; H, 6.00; N, 5.95. Found: C, 70.93; H, 6.43; N, 5.97.

Physical Methods

Resonance Raman spectra were collected with 413.1-nm excitation from a Spectra-Physics model 2060 Krypton-ion laser, with 514.5 nm excitation from a Spectra-Physics model 2080 Argonne-ion laser, and an Acton AM-506 monochromator equipped with a Princeton LN/CCD data collection system. Spectra in THF and d_8-THF were obtained at 77 K using a 135° backscattering geometry. Samples were frozen onto a gold-plated copper cold finger in thermal contact with a Dewar flask containing liquid N_2. As the samples suffered photodegradation from laser irradiation, the laser beam was slowly rastered over the frozen surface during data collection to present fresh spots for irradiation during the course of the experiment. Raman frequencies were calibrated to indene prior to data collection. The monochromator slit width was set for a band pass of 4 cm^{-1} for all spectra. Raman spectral intensities were calibrated relative to the 1145-cm^{-1} solvent peak of THF or the 962-cm^{-1} solvent peak of d_8-THF.

Chapter 4: Characterization of a Series of Heterobimetallic Nonheme Fe-O-M Species

4.1 Introduction

Dioxygen plays a crucial role in the metabolic processes of living organisms, as both its formation and activation are essential to maintaining life. The formation of dioxygen is carried out by green plants, algae and cyanobacteria as a waste product of photosynthesis. The oxidation of water by these organisms, specifically cyanobacteria, led to the Great Oxygenation Event (GOE) and the subsequent evolution of complex life.[111] Dioxygen is a potent oxidant and with the new found atmospheric excess because of the oxidation of water, nature developed a diverse array of metal containing enzymes to utilize dioxygen. These enzymes have evolved to activate O_2 and harness its oxidative power to drive a wide array of critically important reactions such as DNA and RNA repair, antibiotic synthesis and the sensing of hypoxia in cells.[12]

Water oxidation (WO) in nature is performed by a specially developed enzyme, Photosystem II (PS II). Within this enzyme is a unique metallo-oxo cluster, the Oxygen Evolving Complex (OEC), which has been shown to be the active site for WO (Figure 4.1).[112] The OEC is a $CaMn_4O_5$ cubane containing a $CaMn_3O_4$ core with a "dangler" Mn. This "dangler" Mn is part of a heterobimetallic Mn-O-Ca moiety which is proposed, in some mechanistic models,[113–115] to be the key feature responsible for O-O bond formation. In fact, it has been found that the Ca is essential for WO.[116,117] For dioxygen-activating enzymes, the vast majority contain mononuclear or homodinuclear and contain iron or copper in their active sites, a stark difference from the OEC. While the vast majority of dinuclear dioxygen-activating enzymes contain a homobimetallic active site, there are a pair of exceptions which contain heterobimetallic active sites: the heme/copper center of cytochrome oxidase[118] and the recently discovered nonheme Fe-O-Mn center of Class 1c ribonucleotide reductase[119,120] (RNR-1c) (Figure 4.1).

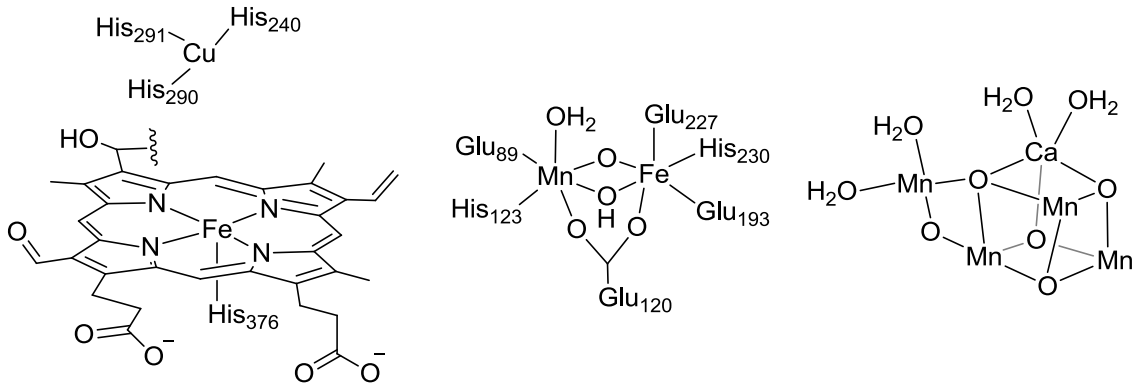

Figure 4.1. Structures of the heterobimetallic active sites of cyctochrome oxidase (left), RNR-1c (center), and the OEC (right).

Because of the importance of WO and the complexity of the OEC, much work has gone into the development and understanding of this metallo-oxo cluster. There is a wealth of synthetic homonuclear Mn-oxo clusters[121] and a number of clusters which mimic the heterobimetallic Mn-O-Ca nature of the OEC.[113,122–124] While these are good structural models, they lack the ability to perform WO. Extensive progress has been made in obtaining and studying synthetic models for the heme/copper center of cyctochrome oxidase,[125,126] but there has been substantially less progress in obtaining synthetic systems mimicking nonheme heterobimetallic complexes, like that found in RNR-1c. The first set of such heterobimetallic complexes were synthesized by hydrolysis between $FeCl_3$(TACN) and MCl_3(Me_3TACN) (M = Cr^{III} or Mn^{III}).[127] This work was followed by the recent synthesis of a Fe^{III}-O-Sc^{III} complex obtained through the reaction of $[Fe^{IV}(O)(TMC)(NCCH_3)]^{2+}$ with $Sc(OTF)_3$.[128–130] One shortcoming to these models is that they were unable to be generated with dioxygen, thus lacking functional mimicry.

The crystal structure of the (TMC)Fe^{III}-O-Sc^{III} species showed that the Fe-O-Sc moiety was on the same side of the TMC ligand (*syn*) as the four methyl groups of the TMC ring (Figure 4.2). While this orientation of the methyl groups has been seen in all the other $[Fe^{II}(TMC)(X)]$ complexes reported to date, where the anionic X ligand occupies the *syn* site, it came as a surprise since the starting Fe^{IV}=O complex has the oxygen atom in the *anti* position.

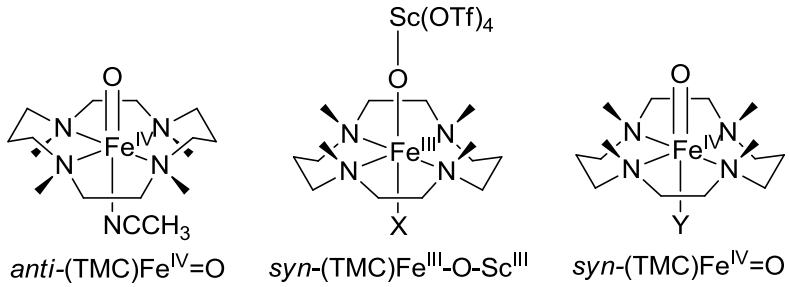

Figure 4.2. Structures for (TMC)Fe^{III}-O-Sc^{III} and the *anti* and *syn* isomers of (TMC)Fe^{IV}=O (X = H_2O or CH_3CN; Y = CH_3CN or OTf).

Because of these puzzling observations, further investigation into the formation of *syn* and *anti* isomers of (TMC)Fe^{IV}=O has been carried out by researchers in the Münck and Que groups.[131] The *anti* isomer of (TMC)Fe^{IV}=O is generated using iodosobenzene (PhIO) and has a characteristic near-IR absorption feature at 824 nm.[132] The use of a bulkier iodosoarene oxidant, 2-$^{t}BuSO_2$-C_6H_4IO (ArIO), produced a Fe^{IV}=O complex with a similar, but distinctly different, near-IR band at 815 nm.[131] Additional characterization by IR, Mössbauer and ^{1}H-NMR confirmed that the use of ArIO generated a species distinct from that generated with PhIO. Definitive proof came in the form of a crystal structure that showed a (TMC)Fe^{IV}=O complex with the oxo unit in the *syn* position (Figure 4.2). The ability to independently synthesize and isolate both the *syn* and *anti* isomers of (TMC)Fe^{IV}=O provides a new set of tools to explore how differences in ligand geometry and orientation effect the properties of closely related species.

In this chapter we report the characterization of two nonheme heterobimetallic Fe-O-M species: a Fe^{III}-O-Cr^{III} species generated from dioxygen activation and a Fe^{IV}-O-Ce^{IV} intermediate generated during iron-catalyzed water oxidation.

4.2 Results and Discussion

4.2.1 Characterization of a heterobimetallic nonheme Fe(III)-O-Cr(III) species

Bubbling O_2 into a solution of 1 mM Fe(TMC)$(OTf)_2$ and 1 mM $Cr(OTf)_2$ in CH_3CN at -40 °C rapidly elicited a UV-vis spectrum with bands at 358, 398, 447, and 558 nm (Figure 4.3), suggesting the formation of a new species designated as **1**. This

spectral pattern was not observed in the absence of either $Fe(TMC)(OTf)_2$ or $Cr(OTf)_2$ from the reaction mixture: $Fe(TMC)(OTf)_2$ simply did not react with O_2, but the reaction of $Cr(OTf)_2$ with O_2 gave rise to features at 358 and 445 nm (Figure 4.3), distinct from those of **1**. Species **1** had a half-life of 10 hrs. at -40 °C and rapidly decayed upon warming to room temperature. Taken together, these observations implicate a role for both Fe and Cr in the formation of **1**.

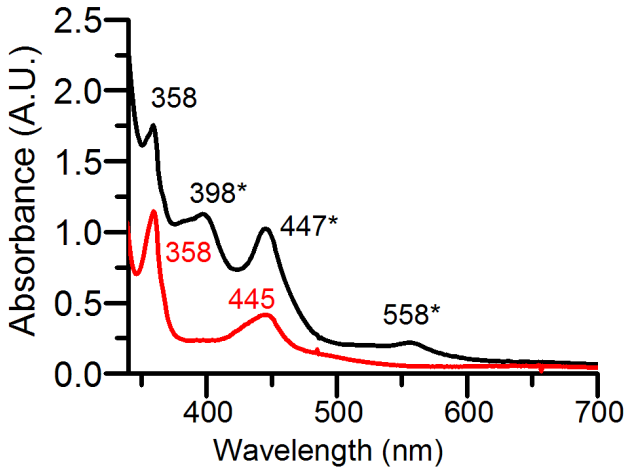

Figure 4.3. UV-vis spectra observed in CH_3CN at -40 °C upon O_2 exposure of 1 mM $Cr(OTf)_2$ (red) and a mixture of 1 mM $Fe(TMC)(OTf)_2$ and 1 mM $Cr(OTf)_2$ (black). Bands with asterisks are associated with **1**.

ESI-MS analysis of the solution of **1** at -40 °C revealed dominant peaks at *m/z* 461.2 (positive mode) and 514.8 (negative mode). The ions observed have masses and isotope distribution patterns that correspond to $[Fe(TMC)(OTf)]^+$ and $[CrO(OTf)_3]^-$, respectively (Figure 4.4). Furthermore, the $[CrO(OTf)_3]^-$ peak was upshifted by two units when $^{18}O_2$ was used, showing the incorporation of an oxygen atom from O_2. Based on these results, we tentatively assign **1** as a heterobimetallic $[(TMC)Fe^{III}\text{-}O\text{-}Cr^{III}(OTf)_4]$ complex.

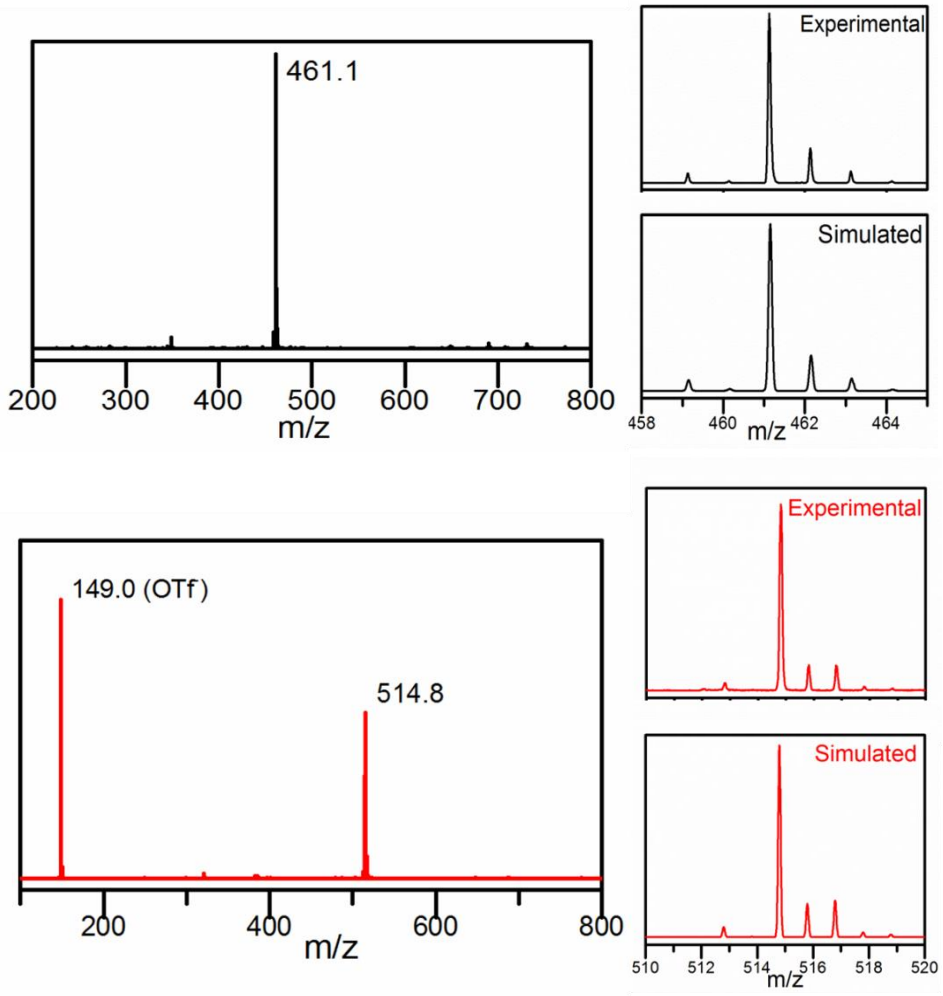

Figure 4.4. ESI-MS spectra of the product from bubbling O_2 into 1 mM $Fe^{II}(TMC)(OTf)_2$ + 1 mM $Cr^{II}(OTf)_2$ solution mixture. Top: positive mode spectrum, together with isotope distribution pattern of the m/z 461.1 peak simulated by $[Fe(TMC)(OTf)]^+$. Bottom: negative mode spectrum, together with isotope distribution pattern of the m/z 514.8 peak simulated by $[Cr(O)(OTf)_3]^-$. ESI-MS data collected and analyzed by Ang Zhou.

To test this hypothesis, we investigated the reaction of $[Fe^{IV}(O)(TMC)(NCCH_3)]^{2+}$ [132] with $Cr(OTf)_2$ [133] in CH_3CN at -40 °C as a more direct means of synthesizing putative species **1**. As shown in Figure 4.5, the addition of $Cr(OTf)_2$ to $[Fe^{IV}(O)(TMC)(NCCH_3)]^{2+}$ in CH_3CN solution caused the instantaneous

disappearance of its characteristic 824-nm peak concomitant with the growth of bands at 398, 447, and 558 that are assigned to **1**. Titration experiments (Figure 4.5, inset) revealed that the transformation was complete upon addition of 1 eq. $Cr(OTf)_2$, strongly suggesting a 1:1 Fe:Cr stoichiometry for **1**.

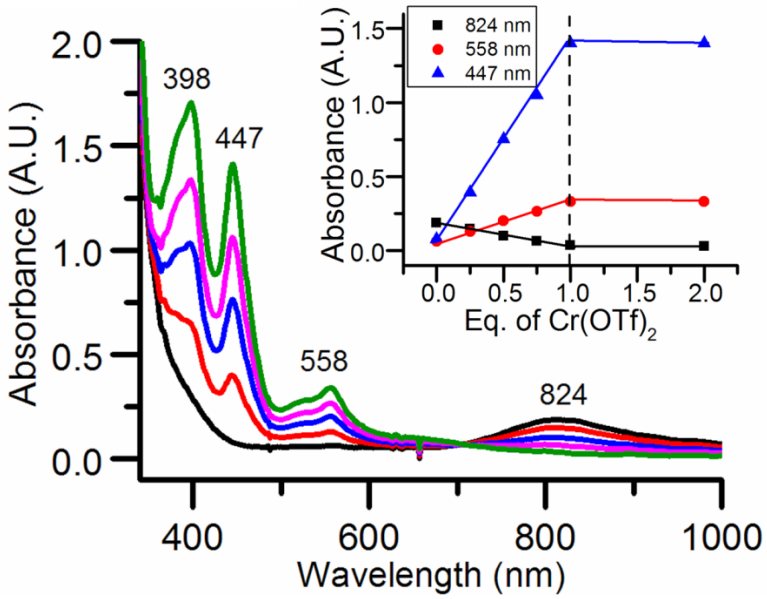

Figure 4.5. UV-vis spectral titration of 0.45 mM $[Fe^{IV}(O)(TMC)(NCCH_3)]^{2+}$ in CH_3CN at -40 °C with $Cr(OTf)_2$. Black, 0 eq.; red, 0.25 eq.; blue: 0.5 eq.; magenta, 0.75 eq.; green, 1 eq. Inset: titration plot. Inset: Formation of **1** vs eq. $Cr(OTf)_2$ added into 0.45 mM $[Fe^{IV}(O)(TMC)(NCCH_3)]^{2+}$ in CH_3CN at -40 °C.

In order to obtain structural insight, Fe K-edge X-ray absorption spectroscopy studies were carried out on **1**. The Fe K-edge of **1** was found at 7124.0 eV, which is comparable to those of known $Fe^{III}(TMC)$ and related complexes.[134,135] The EXAFS region revealed two prominent features at $R + \Delta \sim 1.8$ Å and 3.2 Å. The best fit of the data consisted of 1 O/N scatterer at 1.81 Å, 5 O/N scatterers at 2.17 Å, 4 C scatterers at 2.91 Å and a Cr scatterer at a distance of 3.65 Å. The 1.81 Å scatterer has a Fe-O distance typical of oxo bridges in Fe^{III}-O-M^{III} complexes[136] while the scatterers at 2.17 Å and 2.92 Å arise from the supporting TMC ligand. The intensity of the Cr scatterer derives from multiple scattering pathways due to a linear Fe-O-Cr core as seen in other linear Fe^{III}-O-M complexes.[128–130,137–139] Taken together, we propose that **1** has the

structure shown in Figure 4.6. Of note is the proposal that the Fe-O-Cr unit is in the *anti* position as complex **1** was generated from the *anti* isomer of (TMC)Fe^{IV}=O and the almost immediate formation of the Cr-adduct should prohibit any inversion of the TMC ligand to form the *syn* isomer.

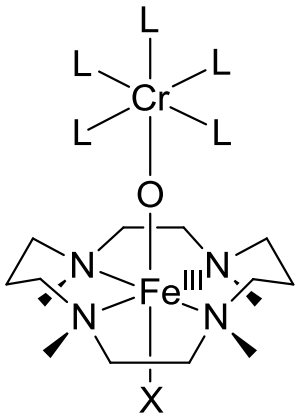

Figure 4.6. Proposed structure for **1** (L = CH_3CN or OTf; X = CH_3CN, NCO or NCS).

Complex **1** was further studied by EPR and resonance Raman (rR) spectroscopy. It is EPR-silent, which is as expected due to antiferromagnetic coupling mediated by the oxo bridge between the Fe(III) and the Cr(III) centers, as seen for two other Fe(III)-O-Cr(III) complexes.[127,139] Excitation of **1** with a 568.2-nm laser elicits a resonance-enhanced vibration at 773 cm^{-1} (Figure 4.7), which falls within the 700-900 cm^{-1} range found for the ν_{as}(Fe-O-Fe) modes of oxo-bridged diiron(III) complexes,[140,141] but below the values determined by IR for a series of Fe-O-Cr porphyrin species (832-849 cm^{-1}).[139] This assignment is corroborated by the observed downshift of this vibration to 730 cm^{-1} upon ^{18}O-subsitution into the oxo bridge. Although a 35 cm^{-1} downshift for a diatomic Fe-O mode is predicted by Hooke's Law, the experimentally obtained ^{18}O shift is 43 cm^{-1}. This larger than predicted shift has been reported for corresponding vibrations of several oxo-bridged diiron(III) complexes.[140]

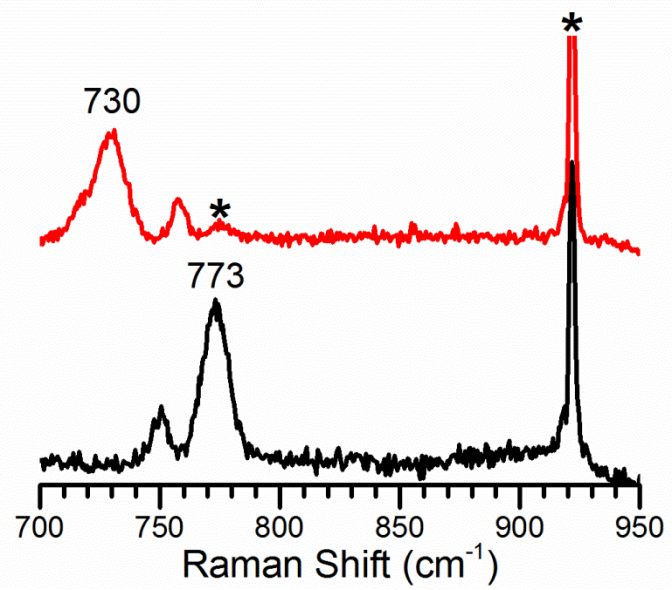

Figure 4.7. Resonance Raman spectra of **1** in CH_3CN (λ_{ex} = 568.2 nm, 20 mW, 77 K). Black, ^{16}O; red, ^{18}O. Asterisks denote solvent peaks.

As previously stated, it is proposed that the Fe-O-Cr core is nearly linear based on the intensity of the Cr scatterer in the EXAFS data. In comparing ν_{as}(Fe-O-M) for **1** with other Fe-O-Fe complexes that have nearly linear Fe-O-Fe cores, we see that the frequency obtained for **1** falls well below the values obtained for these similar systems (~800-890 cm^{-1}).[140] There is also a weaker feature found at 746 cm^{-1} that exhibits an upshift of 7 cm^{-1} upon ^{18}O-substitution; this is an unusual observation that we cannot explain. The 773 cm^{-1} vibration is also weakly enhanced upon 514.5 nm excitation but not observed with 457.9 or 647.1 nm irradiation, suggesting that the 558 nm absorption band can be associated with a transition of the Fe-O-Cr moiety.

Complex **1** exhibits a pre-edge area of 11 units, typical for a six-coordinate Fe(III) center.[142,143] The likelihood of a sixth ligand for the Fe(III) center in **1** is supported by the change in the spectral features upon addition of NCS^- or NCO^-. As shown in Figure 4.8, there are small shifts of the three bands, as well as increases in intensity. Similar shifts in absorption features were seen upon axial ligand substitution in the parent $[Fe^{IV}(O)(TMC)(X)]^{2+/+}$ complexes.[66,144] Based on this information, it is proposed that the

Fe atom has a 6-coordinate environment with the axial position available for ligand substitution (Figure 4.6).

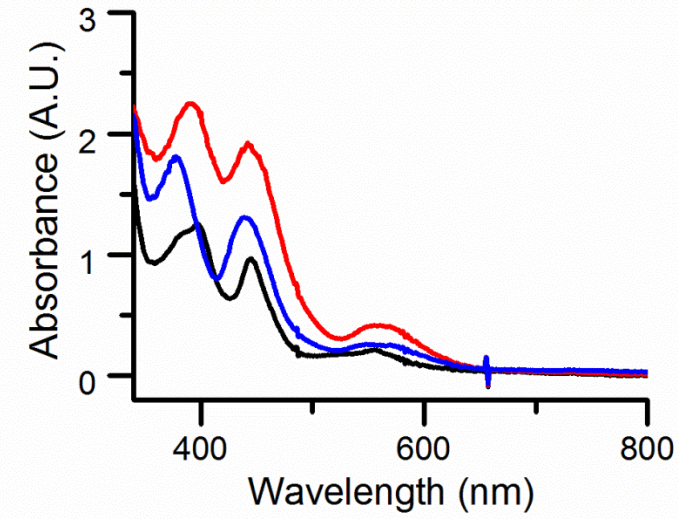

Figure 4.8. UV-vis spectra of 0.3 mM **1** (black), **1-NCO** (blue), **1-NCS** (red) in CH_3CN at -40 °C. λ_{max} (ε_M) for **1**: 398 (3800), 447 (3000), and 558 (700). λ_{max} (ε_M) for **1-NCO**: 380 (6000), 438 (4200), and 560 (850). λ_{max} (ε_M) for **1-NCS**: 390 (7500), 442 (6300), and 560 (1400).

Complexes **1-NCS** and **1-NCO** were studied by rR spectroscopy. Excitation of **1-NCS** and **1-NCO** with a 561-nm laser elicit resonance-enhanced vibrations at 767 and 773 cm^{-1}, respectively (Figure 4.9 and 4.10). Both of these vibrations downshift by 49 cm^{-1} upon the use of ^{18}O. Like **1**, these experimental shifts are larger than that predicted using Hooke's Law (34 and 35 cm^{-1}). The lower frequency for ν_{as}(Fe-O-Cr) in **1-NCS** as compared to **1** follows the trend seen in several trans-ligand substituted systems,[145] including $[Fe^{IV}(O)(TMC)(X)]^{2+/+}$.[144] In these systems, the weakest ν(Fe-O) was seen for the complex with the most basic trans-axial ligand. NCS^- is a stronger trans donor than CH_3CN and we see this represented in the slightly lowered ν_{as}(Fe-O-Cr) value for the NCS adduct. The ^{16}O rR spectrum for **1-NCO** shows a poorly resolved shoulder (Figure 4.10). Fitting this feature with two peaks provided frequency values of 773 cm^{-1} and 770 cm^{-1}. The fact that there appears to be two peaks of very similar ν_{as}(Fe-O-Cr) values and similar intensities, with one having the same frequency as the parent compound **1**, for **1-**

NCO is unexpected. Titration experiments showed that only 1 equiv. of NCS^- or NCO^- is needed to fully form the corresponding species (Figure 4.12). As we do not see a mixture of species in **1-NCS**, we would not expect a mixture of species for **1-NCO**. This is an interesting observation that requires further investigation. If we assume the value of 770 cm^{-1} corresponds to **1-NCO**, then the downshift of 3 cm^{-1} is reasonable. NCO^- is a slightly weaker trans donor than NCS^-, and as **1-NCS** only had a decrease in ν_{as}(Fe-O-Cr) of 6 cm^{-1}, a smaller shift would be expected.

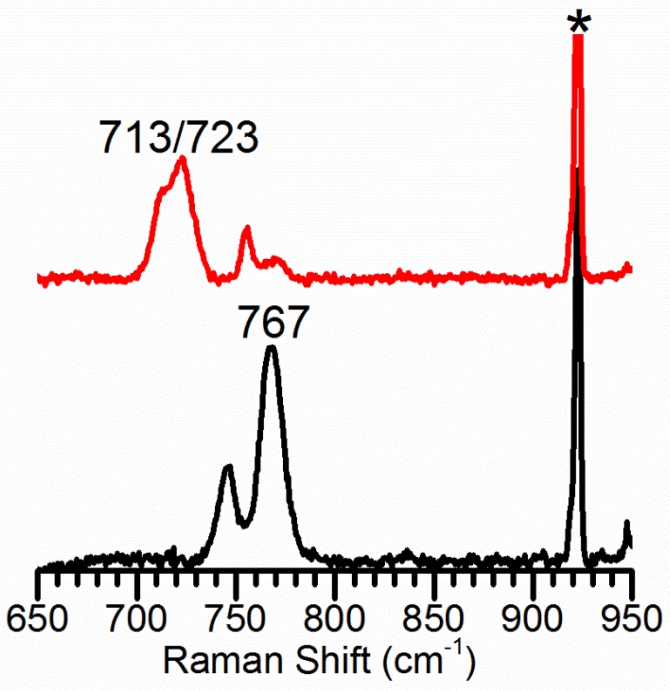

Figure 4.9. Resonance Raman spectra of **1-NCS** in CH_3CN (λ_{ex} = 561 nm, 80 mW, 77 K). Black, ^{16}O; red, ^{18}O. Asterisks denote solvent peaks.

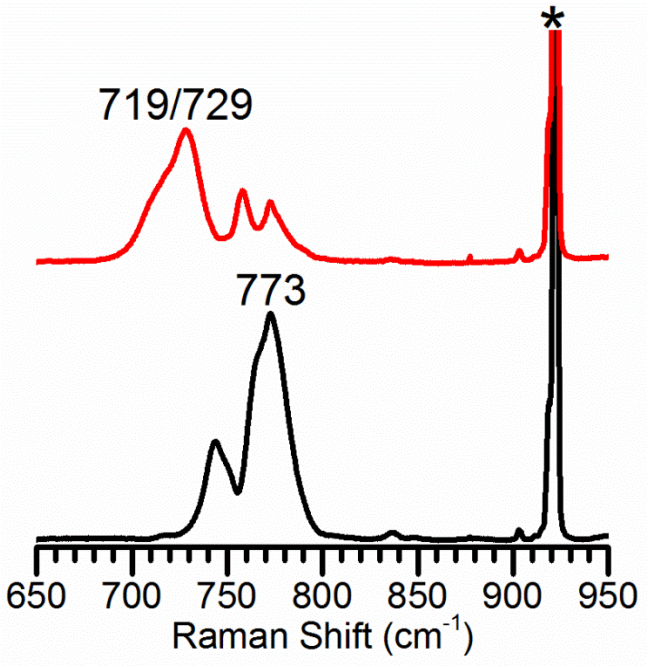

Figure 4.10. Resonance Raman spectra of **1-NCO** in CH_3CN (λ_{ex} = 561 nm, 80 mW, 77 K). Black, ^{16}O; red, ^{18}O. Asterisks denote solvent peaks.

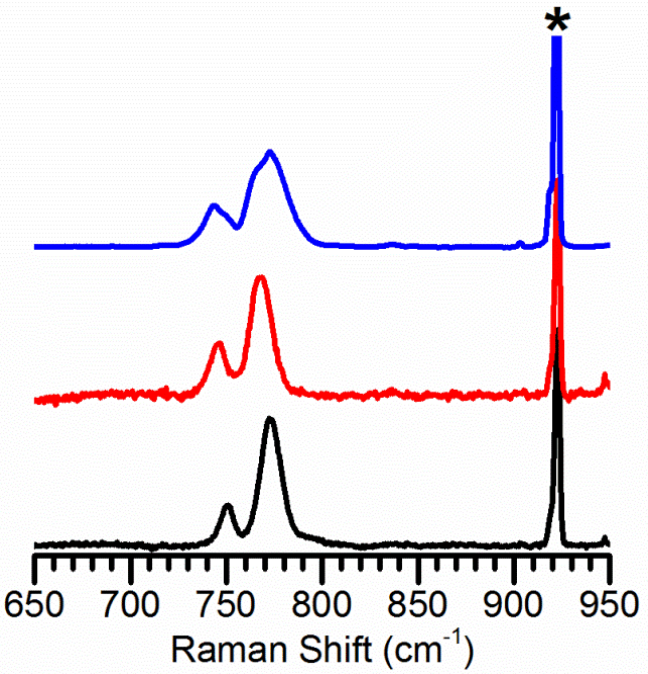

Figure 4.11. Resonance Raman spectra of **1** (Black), **1-NCS** (Red), **1-NCO** (Blue) in CH_3CN (λ_{ex} = 561 nm, 80 mW, 77 K). Asterisks denote solvent peaks.

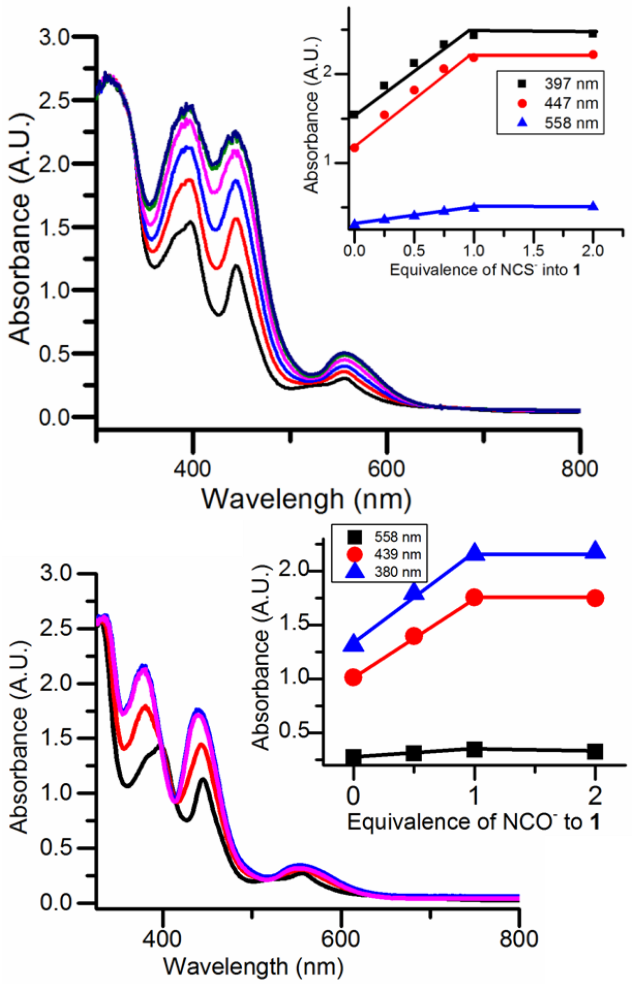

Figure 4.12. Top) Changes in the UV-vis spectrum when NBu_4SCN was added into 0.42 mM **1** in CH_3CN at -40 °C. Inset: Absorbance change with the addition of NCS^- into **1**. **Bottom)** Changes in the UV-vis spectrum when NBu_4NCO was added into 0.4 mM **1** in CH_3CN at -40 °C. Inset: Absorbance change with the addition of NCO^- into **1**.

4.2.2 Resonance Raman Studies of *syn* and *anti* (TMC)Fe-O-M Species

As complex **1** is proposed to be a $(TMC)Fe^{III}$-O-Cr^{III} species in the *anti* orientation (Figure 4.6), attempts were made to obtain the *syn* isomer for characterization and comparison. To a solution of *syn*-$[Fe^{IV}(O)(TMC)(NCCH_3)]^{2+}$ [131] was added 1 equiv. of $Cr(OTf)_2$ leading to the rapid growth (within 20 seconds) of a species with bands at 398, 447, 516 and 560 nm (Figure 4.13). The UV-Vis features of this species are similar,

but distinctly different from those of **1** (Figure 4.5) thus indicating the formation of a new species, designated **2**.

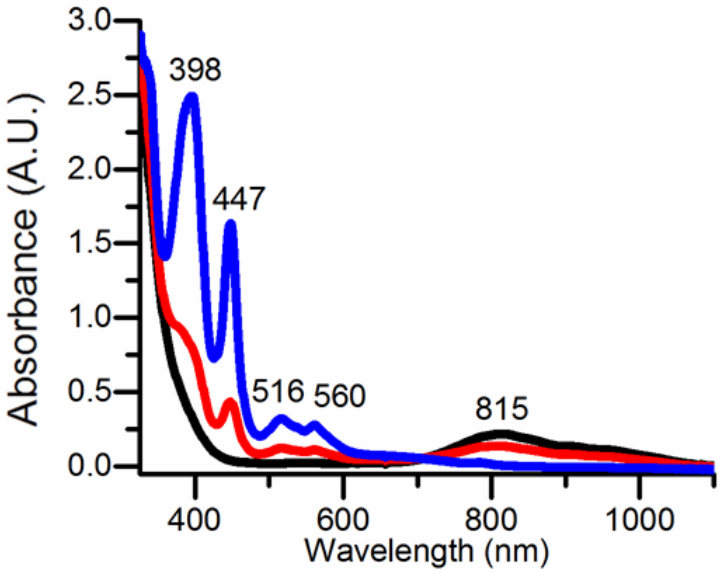

Figure 4.13. UV-vis spectral changes upon the addition of 1 equiv. of $Cr(OTf)_2$ to 0.5 mM *syn*-$[Fe^{IV}(O)(TMC)(NCCH_3)]^{2+}$ in CH_3CN at 25°C.

In order to obtain structural insight, Fe K-edge X-ray absorption spectroscopy studies were carried out on **2**. The Fe K-edge of **2** was found at 7123.6 eV, which is comparable to those of known Fe^{III}(TMC) and related complexes.[134,135] The best fit of the data consisted of 1 O/N scatterer at 1.77 Å, 4 O/N scatterers at 2.16 Å, 4 C scatterers at 2.99 Å and a Cr scatterer at a distance of 3.57 Å. The 1.77 Å scatterer has a Fe-O distance typical of oxo bridges in Fe^{III}-O-M^{III} complexes,[136] while the scatterers at 2.16 Å and 2.99 Å arise from the supporting TMC ligand. The intensity of the Cr scatterer derives from multiple scattering pathways due to a linear Fe-O-Cr core as seen in other linear Fe^{III}-O-M complexes.[128–130,137–139]

Complex **2** shows a resonance-enhanced vibration at 877 cm^{-1} upon irradiation at 514.5 nm (Figure 4.14). This vibration shifts to 832 cm^{-1} upon ^{18}O-substitution into the oxo bridge. The experimental shift of 45 cm^{-1} is in reasonable agreement with the calculated value for a diatomic Fe-O mode as predicted by Hooke's Law, 39 cm^{-1}. The ν_{as}(Fe-O-M) value obtained for **2** also falls within the range of values obtained for other

linear Fe-O-Fe species,[140] thus confirming the linear assignment for the Fe-O-Cr core as proposed by the EXAFS data.

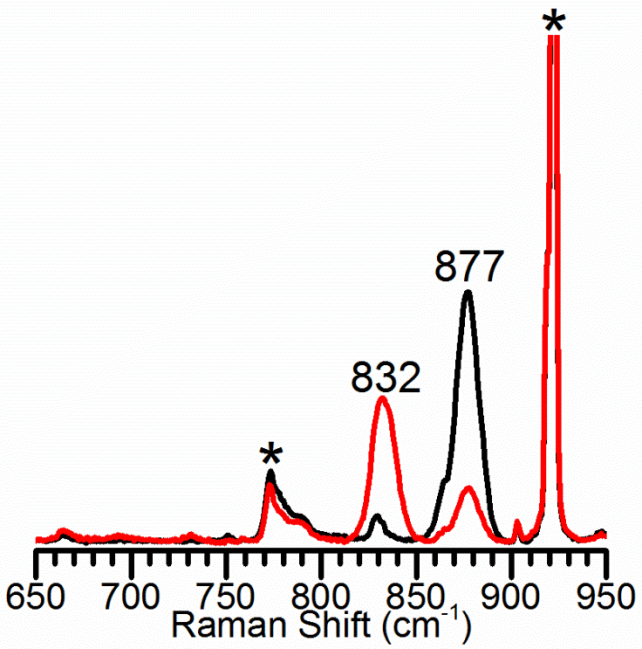

Figure 4.14. Resonance Raman spectra of **2** in CH_3CN (λ_{ex} = 515 nm, 80 mW, 77 K). Black, ^{16}O; red, ^{18}O. Asterisks denote solvent peaks.

The ν_{as}(Fe-O-Cr) value for **2** is drastically different from that for **1** despite the fact that the proposed structures for these complexes are very similar (Figure 4.15). The ~100 cm^{-1} difference in stretching frequency for these two complexes can possibly be explained by some differences between their proposed structures. While both **1** and **2** contain Fe-O-Cr cores, the Fe-O and Fe...Cr distances are different. **2** has both a shorter Fe-O distance, 1.77 Å versus 1.81 Å, and a shorter Fe...Cr distance, 3.57 Å versus 3.65 Å. A shorter Fe-O bond indicates a stronger bond and thus a vibration of higher energy, as seen in the case of **2**. This same trend was seen in the axially substituted $[Fe^{IV}(O)(TMC)(X)]^{2+/+}$ system where shorter Fe-O bonds corresponded to higher ν(Fe=O) values.[144] In this series, a bond shortening of 0.03 Å corresponded to an increase in frequency of only 32 cm^{-1}, well below the difference seen between **1** and **2**.

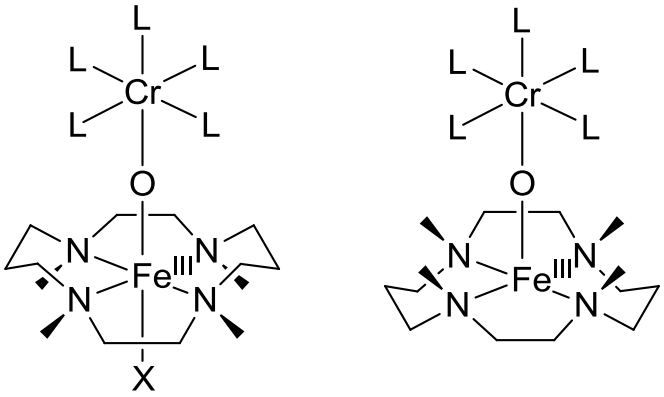

Figure 4.15. Proposed structures for **1** (Left), and **2** (Right) (L = CH_3CN or OTF; X = CH_3CN, NCO or NCS).

The purpose for making complex **2** was to generate the *syn* isomer for comparison with **1**, which as an *anti* configuration. Perhaps it is the inversion of the Fe-O orientation with respect to the TMC methyl groups that has such a dramatic effect on the ν_{as}(Fe-O-M) frequency. As previously stated in the introduction, the *syn* and *anti* isomers of $[Fe^{IV}(O)(TMC)(NCCH_3)]^+$ have recently been characterized and their ν(Fe=O) values obtained by IR.[131] The *syn* isomer has a ν(Fe=O) frequency of 856 cm^{-1}, 22 cm^{-1} higher than that for the *anti* isomer. The difference in ν(Fe=O) frequency cannot be solely attributed to the inversion of the ligand because the Fe=O bond distance is also 0.02 Å shorter for the *syn* isomer, which would expectedly lead to a higher ν(Fe=O) frequency. Regardless, simple inversion of the ligand geometry does not appear to have a dramatic enough effect on the stretching frequencies of the system to induce a ~100 cm^{-1} difference for the Fe-O-Cr complexes.

Another difference between **1** and **2** is the coordination number of the iron center. **2** has a 5-coordinate iron center with no ligand trans to the Fe-O-Cr, while **1** has a trans $NCCH_3$ ligand and is thus 6-coordinate. The assignment as a 5-coordinate iron center is supported by the large pre-edge area, 33.7, taken from the XANES analysis and the fact that addition of axial ligands, such as NCS^- and NCO^-, did not cause a change in the UV-vis spectrum, implying no binding of the introduced axial ligands to the iron center. For

comparison, the pre-edge area for **1** is 11, while the pre-edge area for the 5-coordinate Fe(III)-O-Sc(III) complex is 32.[130] The difference in ν_{as}(Fe-O-Fe) between a 5- to 6-coordinate Fe center is again very large when comparing another pair of TMC-based Fe-O-M complexes in which one is 6-coordinate, with a trans Cl^- ligand (**3**), and the other is 5-coordinate and lacks any ligand trans to the Cl_3Fe-O-Fe (**4**) unit (Figure 4.16).[146] The ν_{as}(Fe-O-Fe) values for **3** and **4** were determined by IR to be 798 and 886 cm^{-1} respectively, again showing a large difference in ν_{as}(Fe-O-Fe) frequency (88 cm^{-1}). It has been shown previously that the nature of the trans ligand can affect the ν(Fe=O) frequency in the axially-substituted $[Fe^{IV}(O)(TMC)(X)]^{2+/+}$ series,[144] but these are the first set of complexes that systematically tests the effect the inclusion/absence of a trans ligand has on the ν_{as}(Fe-O-M) value.

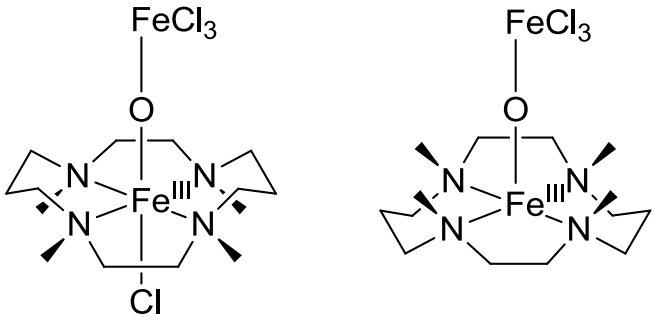

Figure 4.16. Structures for **3** (Left), and **4** (Right).

4.2.3 Evidence for an Oxygen Evolving Fe-O-Ce Intermediate in Fe-catalyzed Water Oxidation

While there has been much work in developing structural models for the unique metallo-oxo cluster found in the OEC,[113,122–124] these synthetic models have been found lacking in water oxidation (WO) function. There are examples of synthetic metallo-oxo clusters which have proven effective at WO,[147] but because of their heterogeneous nature, they do not provide much mechanistic insight into the key step in WO, O-O bond formation. Researchers have been using homogeneous, synthetic catalysts to gain insight into the mechanism of water oxidation WO,[148,149] and specifically O-O bond formation, as it is recognized that this multi-electron and proton step is the bottleneck challenge in

the development of synthetic systems. It was recently discovered that a variety of non-heme iron complexes supported by tetradentate nitrogen-based ligands were competent towards chemically driven WO.[150–153] The most effective of these catalysts contained two *cis* labile sites and of these, the complex α-[$Fe^{II}(CF_3SO_3)_2$(mcp)] (mcp = (*N*,*N*'-dimethyl-*N*,*N*'-bis(2-pyridylmethyl)-1,2-*cis*-diaminocyclohexane) (**5-α**) showed particularly good efficiency.

The addition of 3 eq. of ceric ammonium nitrate (CAN) to **5-α** in H_2O at pH = 1 resulted in the formation of the corresponding Fe(IV)=O species, **6-α** (Figure 4.17, Left). The assignment of **6-α** as an Fe(IV)=O species was confirmed by high resolution cryospray ionization mass spectrometry (CSI-HRMS) and resonance Raman spectroscopy (rR). CSI-HRMS showed an intense peak at *m/z* = 545.1101 ± 0.003, which upshifted by 2 mass units when **6-α** was generated in $H_2{}^{18}O$ (Figure 4.17, Right). The *m/z* ratio and isotope distribution pattern correspond to an assignment of $[Fe^{IV}(O)(OTf)(mcp)]^+$. An additional signal was seen at *m/z* = 413.162 ± 0.003, which upshifted by 4 mass units with the use of $H_2{}^{18}O$ as solvent. Therefore, the peak was assigned to the $[Fe^{IV}(O)(OH)(mcp)]^+$ ion. This pair of ions may correspond to the respective loss of H_2O and CF_3SO_3H from the parent $\{[Fe^{IV}(O)(OH_2)(mcp)](CF_3SO_3)\}^+$ ion, thus identifying **6-α** as $[Fe^{IV}(O)(OH_2)(mcp)]^{2+}$. Resonance Raman spectroscopy confirmed this assignment with the observation of a resonance enhanced feature at 822 cm^{-1} that downshifted by 40 cm^{-1} upon the incorporation of ^{18}O (Figure 4.18a).[69,144]

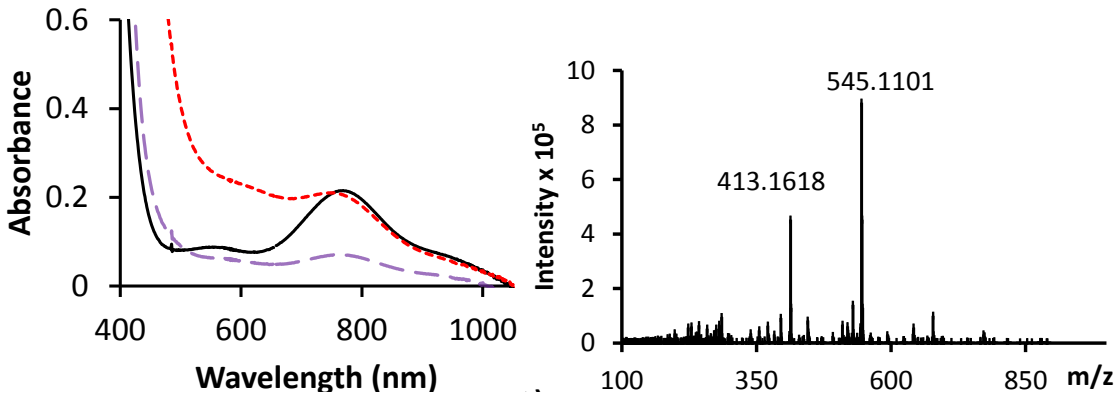

Figure 4.17. Left) UV-Vis spectra of **6-α** (solid black line) formed by the reaction of **5-α** (1mM) in Milli-Q H_2O at 25 °C with 3 eq. of CAN, upon addition of 75 eq. of CAN (dotted red line) and after CAN consumption (dashed purple line). **Right)** CSI-HRMS spectrum of **6-α** recorded immediately after the oxidation of **5-α** (1mM) by 3-eq. CAN.

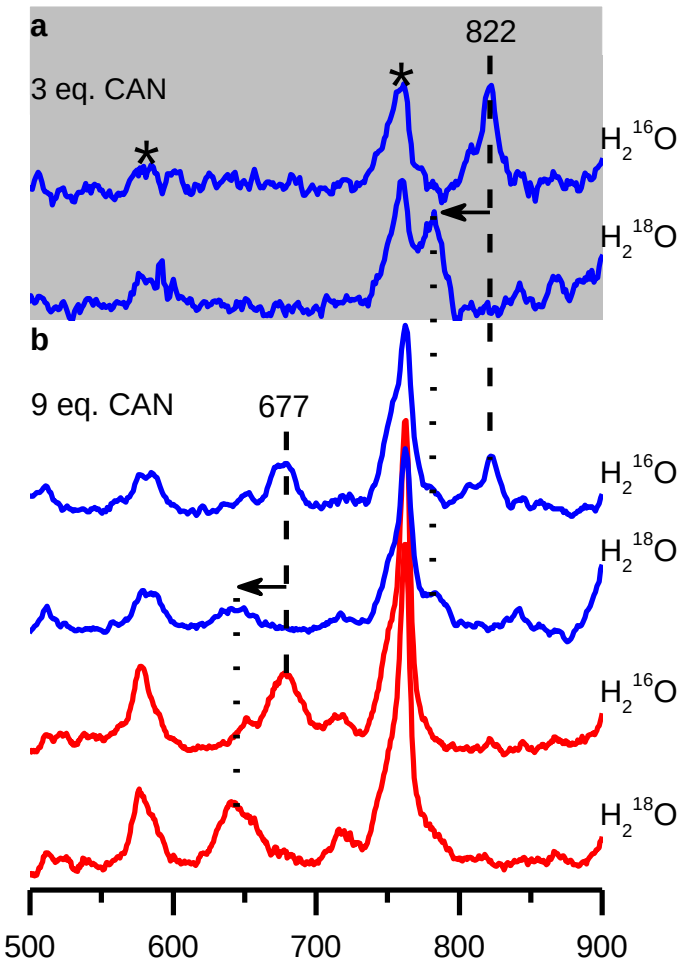

Figure 4.18. (**a**) Highlighted in grey, rR spectra of **6-α** (λ_{ex} 413.1 nm, 100 mW) prepared on addition of 3 equiv. CAN to a solution of **5-α** (5 mM) in 1:1 H_2O:MeCN. (**b**) rR spectra of **7-α** prepared on addition of 9 equiv. CAN to a solution of **5-α** in 1:1 H_2O:MeCN. Blue: λ_{ex} = 413.1 nm, 100 mW, [Fe] = 5mM. Red: λ_{ex} = 514.5 nm, 100 mW, [Fe] = 8mM. All spectra were collected from liquid solutions maintained at -8 °C. Asterisks denote features arising from CAN. The intensity of the MeCN solvent peak at 922 cm^{-1} was used to normalize the intensities of the peaks among the various spectra.

Decay of **6-α** did not result in O_2 evolution, showing that it cannot be the water oxidation (WO) species. Further addition of CAN was necessary to generate a species capable of WO. Addition of 75 eq. of CAN to **6-α** resulted in O_2 evolution concomitant with Ce^{IV} consumption with a TON of 18.4 (theoretical maximum TON = 18.75 based on

initial Ce^{IV} with $n(Ce^{IV})/n(O_2) = 4$). Through monitoring the reaction of **6-α** with excess CAN by UV-Vis spectroscopy, a new broad absorption band in the 500-650 nm range was observed (Figure 4.17, left). This band decayed during the course of O_2 evolution concomitant with Ce^{IV} consumption, thus providing evidence for a new reaction intermediate competent in WO, **7-α**.

CSI-HRMS experiments were able to shed light on the nature of **7-α**. The addition of excess CAN caused the disappearance of the peak at *m/z* = 515.110, corresponding to **6-α**, and the appearance of a new peak at *m/z* = 738.0235. The use of $H_2{}^{18}O$ as solvent caused this new peak to upshift by 4 units, implying **7-α** contained two oxygen atoms that are capable of facile exchange with water, while the use of D_2O did not cause any shift, showing **7-α** does not have any exchangeable protons. The isotope distribution pattern for **7-α** fit with the formulation of $[Fe^{IV}(O)_2(mcp)Ce^{IV}(NO_3)_3]^+$ (Figure 4.19).

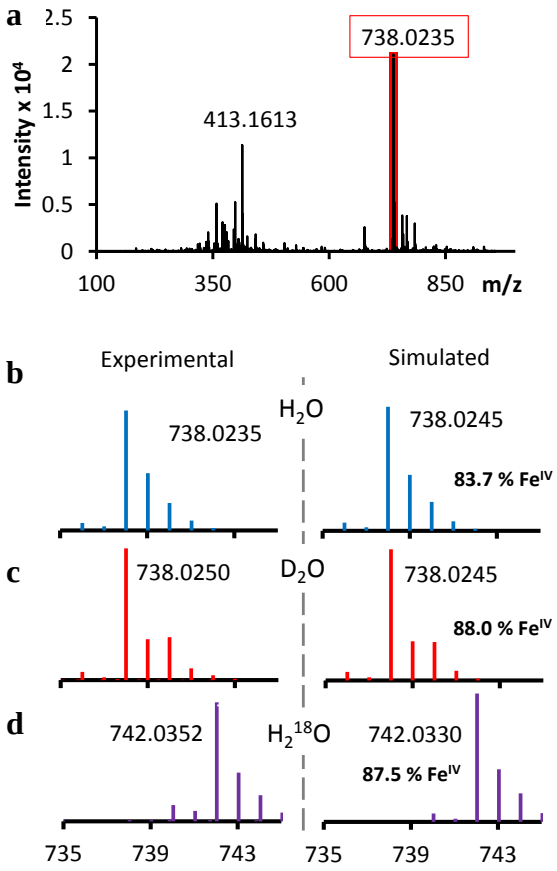

Figure 4.19. (**a**) CSI-HRMS spectrum obtained during the WO reaction, on the addition of 75 eq. of CAN to **6-α**. (**b-d**) CSI-HRMS features associated with **7-α** obtained in H_2O, D_2O and $H_2{}^{18}O$ as solvent. Spectra were recorded by setting the nebulizer and dry gas temperature of the cryospray instrument to 25 °C.

With the atomic composition of **7-α** in hand, further insight into the nature of this novel iron-cerium adduct was obtained through the use of rR of liquid samples maintained at -8 °C in a 1:1 H_2O:CH_3CN. As shown in Figure 4.18a, the rR spectrum of **6-α** prepared with 3 equiv. of Ce^{IV} exhibits a feature at 822 cm^{-1} that downshifts to 782 cm^{-1} upon replacing $H_2{}^{16}O$ by $H_2{}^{18}O$, consistent with its assignment as the $\nu_{Fe=O}$ of **6-α**. Near-UV excitation was required to observe this feature, as **6-α** has insignificant absorbance in the visible region, as found for other non-heme Fe(IV)=O complexes.[69,144]

Interestingly, the rR spectra of **7-α** obtained with the same excitation wavelength (Figure 4.18b) also show the 822 cm^{-1} vibration and its downshift to 782 cm^{-1} upon $H_2{}^{18}O$ substitution. This feature may arise from either **6-α** or **7-α** or both species. To clarify, we compared the intensities of the 822 cm^{-1} peaks for the **6-α** (3-CAN) and **7-α** (9-CAN) samples relative to the adjacent 762 cm^{-1} nitrate feature as an internal standard, after taking into account that the 9-CAN sample has three times the amount of nitrate as the 3-CAN sample. Indeed, the two samples were found to have 822 cm^{-1} peaks of comparable intensity. Given an association constant of 120(± 25) M^{-1} for the interaction of **6-α** with CAN from UV-vis titration experiments, it is expected that **7-α** would account for ~80% of the iron in the Raman samples. Therefore, the 822 cm^{-1} $\nu_{Fe=O}$ vibration observed in the 9-CAN samples must arise mainly from **7-α**.

Notably, a second feature of similar intensity appears at 677 cm^{-1} with 413.1 nm excitation in the sample of **7-α** (Figure 4.18b). This lower-frequency feature persists when **7-α** is probed with 514.5 nm excitation, a wavelength at which only **7-α** has an absorption feature, but the 822 cm^{-1} vibration is not observed, consistent with the absorption features associated with the Fe(IV)=O unit.[154,155] With either excitation wavelength, the 677 cm^{-1} peak downshifts to 643 cm^{-1} on replacing $H_2{}^{16}O$ by $H_2{}^{18}O$, but is not affected when the experiment was carried out in D_2O (Figure 4.18b). The 34 cm^{-1} downshift is consistent with a diatomic Fe-O vibration, but the lower frequency indicates a weaker Fe-O bond that is also resonance-enhanced with 514.5 nm excitation upon Ce-adduct formation. Fe-O modes in this frequency range have previously been reported for complexes with $Fe^{III}(\mu\text{-}O)_2Fe^{IV}$ (666 cm^{-1})[156,157] and $Fe^{IV}{}_2(\mu\text{-}O)_2$ (674 cm^{-1})[158] cores, respectively, suggesting the possibility of forming an analogous $Fe^{IV}(\mu\text{-}O)_2Ce^{IV}$ core, which would be consistent with the elemental composition of **7-α** determined by CSI-HRMS. To test whether this feature could arise from an $Fe^{IV}(\mu\text{-}O)_2Ce^{IV}$ diamond core, rR experiments on **7-α** were performed in a 1:1 $H_2{}^{16}O$:$H_2{}^{18}O$ solvent mixture. Under these conditions, the rR spectrum exclusively shows peaks at 677 and 643 cm^{-1}, with no peak found at an intermediate frequency that could be associated with a mixed-labeled diamond core (Figure 4.20).[159] The $H_2{}^{16}O$:$H_2{}^{18}O$ experiment thus excludes formation of an $Fe^{IV}(\mu\text{-}O)_2Ce^{IV}$ core. Consideration of the above points together with its mass spectral formulation leads us to favour an $O{=}Fe^{IV}$-O-Ce^{IV} core for **7-α**.

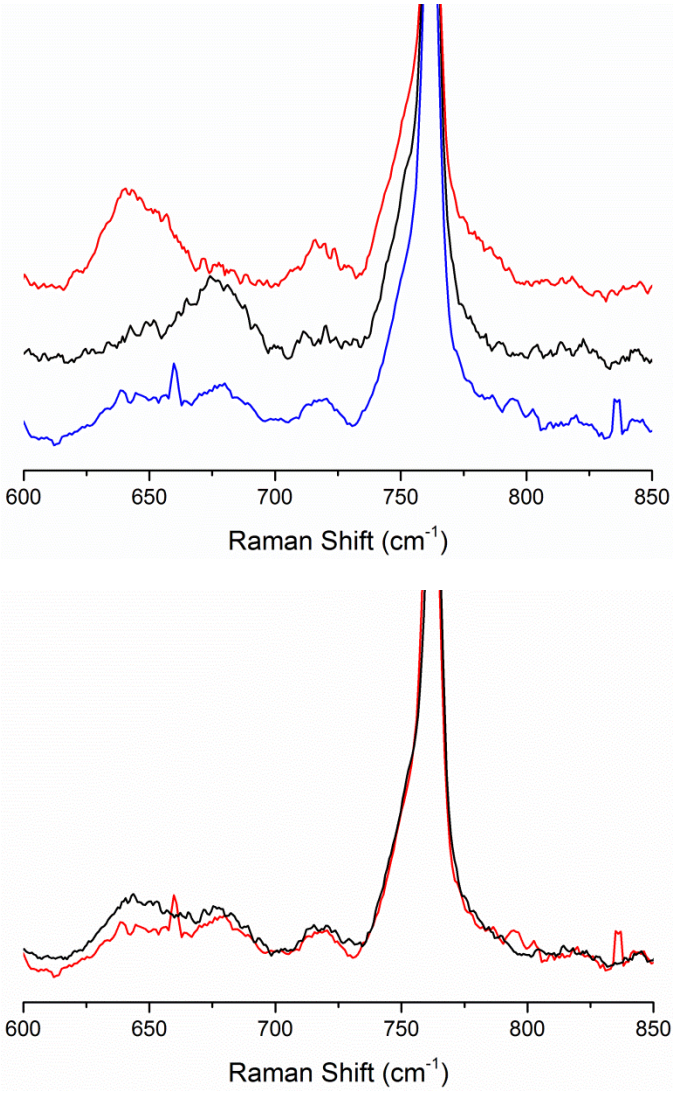

Figure 4.20. Top) Resonance Raman spectra of **7-α** (λ_{ex} 514.5 nm, 140 mW) prepared upon addition of 9 eq. of CAN to a 6-mM solution of **5-α** in 1:1 H_2O:MeCN. $H_2{}^{16}O$: Black. $H_2{}^{18}O$: Red. 1:1 $H_2{}^{16}O$: $H_2{}^{18}O$: Blue. **Bottom)** Resonance Raman spectra of **7-α** (λ_{ex} 514.5 nm, 140 mW) prepared upon addition of 9 eq. of CAN to a 6 mM solution of **5-α** in 1:1 H_2O:MeCN. 1:1 $H_2{}^{16}O$: $H_2{}^{18}O$: Red. Sum of individual $H_2{}^{16}O$ and $H_2{}^{18}O$ spectra divided by 2: black.

Identification of **7-α** with an O=Fe^{IV}-O-Ce^{IV} core as the key reaction intermediate in WO reactions introduces unconsidered mechanistic scenarios for the oxidation of water by Ce^{IV} (Scheme 4.1). Most obviously, Ce^{IV} appears not to behave simply as an outer-sphere oxidant, but instead forms an inner-sphere Fe^{IV}(μ-O)Ce^{IV} intermediate that is crucial for the reaction to proceed. Although Ru-O-Ce intermediates have been proposed in water oxidation reactions by different research groups,[160–164] to the best of our knowledge this is the first direct experimental characterization of a heterobimetallic core in a synthetic WO catalyst.

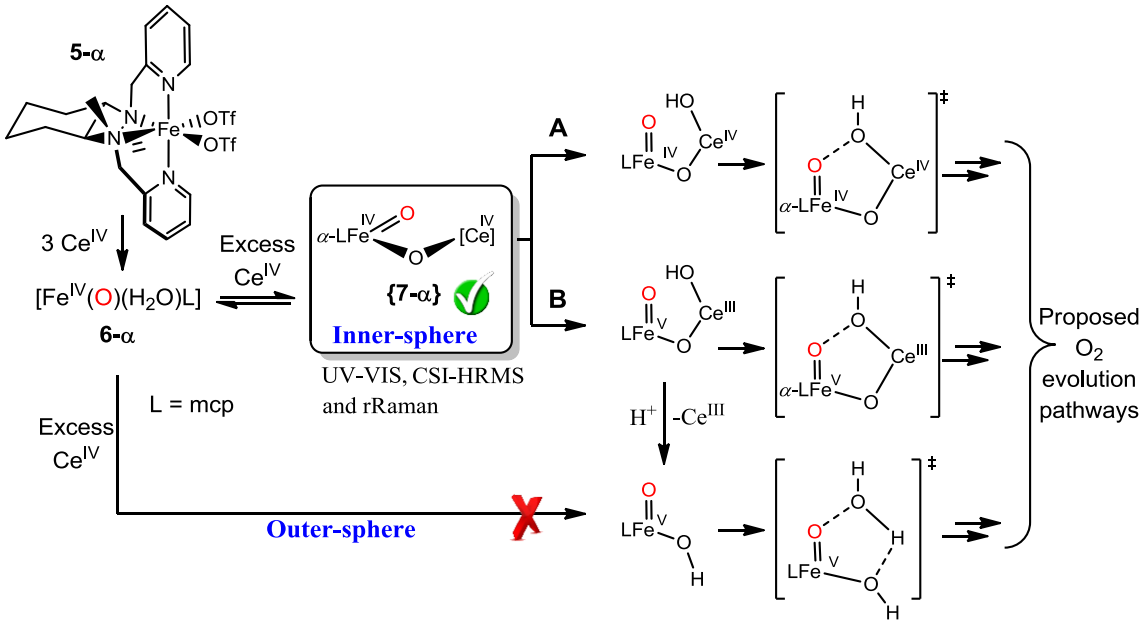

Scheme 4.1. The mechanism is based on the formation of **7-α** as key intermediate for the O_2 evolution. Mechanism A describes the oxo/oxyl radical coupling between Fe^{IV}(O) and Ce^{IV}(OH). Path B describes the formation of Fe^{V}(O) and the subsequent nucleophilic attack of a water molecule.

4.3 Summary

In summary, a heterobimetallic nonheme species **1** with a Fe-O-Cr core has been generated from activation of dioxygen and, separately, by inner-sphere electron transfer. Characterization of this species provided an interesting observation; that the ν_{as}(Fe-O-Cr) frequency (773 cm^{-1}) was much lower than would be expected for a nearly-linear Fe-O-Cr (800-890 cm^{-1}),[140] as proposed by EXAFS analysis. Species **1** represents only the

second example of a heterobimetallic (TMC)Fe-O-M complex, and the first to be generated by O_2.

The *syn* isomer of species **1**, complex **2**, was also synthesized and characterized. The most striking difference between these two species is the >100 cm^{-1} difference in ν_{as}(Fe-O-Cr) frequency. By comparing this pair of species to a set of similar *anti*/*syn* complexes (**3** and **4**), we were able to propose that the dramatic difference seen in the ν_{as}(Fe-O-M) frequency is related to the difference in coordination number around the Fe-center, with 5-coordinate complexes having much higher ν_{as}(Fe-O-M) values.

Finally, a heterobimetallic species in iron-catalyzed water oxidation was characterized. This species, **7-α**, was formulated as containing a Fe^{IV}-O-Ce^{IV} core and was found to be the last detectible intermediate prior to O_2 evolution. The ν_{as}(Fe-O-Ce) value for this species was found to be 676 cm^{-1}, a value much lower than those observed for the above mentioned Fe-O-M. Unfortunately, there is no structural data for **7-α** to give us insight into the linearity of the Fe-O-Ce unit, but because of its low ν_{as}(Fe-O-Cr) value,[140] we would expect this core to deviate substantially from linear, similar to what is seen for the Mn-O-Ca unit of the OEC.[165]

The systems studied above provide synthetic models for heterobimetallic, enzymes. During the course of characterization, some interesting relationships between rR frequency, linearity of the M-O-M' unit and coordination number were found. Taken together, the observations seen should provide impetus for further exploration into these relationships and how they intertwine.

Table 4.1. Summary of Species Characterized in this Chapter

Complex	Orientation	Coord #	Fe-O Å	v(Fe-O-M), cm-1 ($\Delta^{18}O$)	ref
1	*anti*	6	1.81[a]	773 (43)	[133]
1-NCS	*anti*	6	1.85[a]	767 (49)	This Work
1-NCO	*anti*	6	-	773 (49)	This Work
2	*syn*	5	1.77[a]	877 (45)	This Work
3	*anti*	6	1.851	798[b]	[146]
4	*syn*	5	1.746	886[b]	[146]
Fe(III)-O-Sc(III)	*syn*	5	1.748	-	[130]
7-α	-	6[c]	-	676 (34)	[166]
6-α	-	6[c]	-	822 (40)	[166]
anti-(TMC)Fe^{IV}=O	*anti*	6	1.646	834 (34)[b]	[132]
syn-(TMC)Fe^{IV}=O	*syn*	6	1.625	856 (36)[b]	[131]

[a] Value obtained by EXAFS. [b] Value obtained by IR. [c] Inferred from CSI-HRMS formulation.

4.4 Experimental

Resonance Raman spectra were collected at 568.2-nm and 413.1-nm excitation from a Spectra-Physics model 2060 krypton-ion laser, 514.5-nm excitation from a Spectra-Physics model 2080 argon-ion laser, and 561-nm excitation from a Cobolt Jive 150 mW laser and an Acton AM-506 monochromator equipped with a Princeton LN/CCD data collection system. Spectra in Acetonitrile were obtained at 77 K using a 135° backscattering geometry. Samples were frozen onto a gold-plated copper cold finger in thermal contact with a Dewar flask containing liquid N_2. Low-temperature spectra in H_2O:CH_3CN solution mixtures were obtained at 265 K using 90° backscattering geometry. Raman frequencies were calibrated to indene prior to data collection. The monochromator slit width was set for a band pass of 4 cm^{-1} for all spectra. Raman spectral intensities were calibrated relative to the 921-cm^{-1} solvent peak of Acetonitrile.

Bibliography

(1) Hausinger, R. P. *Crit. Rev. Biochem. Mol. Biol.* **2004**, *39*, 21.

(2) Hanauske-Abel, H. M.; Günzler, V. *J. Theor. Biol.* **1982**, *94*, 421.

(3) Krebs, C.; Galonić Fujimori, D.; Walsh, C. T.; Bollinger, J. M. *Acc. Chem. Res.* **2007**, *40*, 484.

(4) Elkins, J. M.; Ryle, M. J.; Clifton, I. J.; Dunning Hotopp, J. C.; Lloyd, J. S.; Burzlaff, N. I.; Baldwin, J. E.; Hausinger, R. P.; Roach, P. L. *Biochemistry* **2002**, *41*, 5185.

(5) Koehntop, K. D.; Emerson, J. P.; Que Jr, L. *J. Biol. Inorg. Chem.* **2005**, *10*, 87.

(6) Price, J. C.; Barr, E. W.; Tirupati, B.; Bollinger, J. M.; Krebs, C. *Biochemistry* **2003**, *42*, 7497.

(7) Price, J. C.; Barr, E. W.; Glass, T. E.; Krebs, C.; Bollinger, J. M. *J. Am. Chem. Soc.* **2003**, *125*, 13008.

(8) Price, J. C.; Barr, E. W.; Hoffart, L. M.; Krebs, C.; Bollinger, J. M. *Biochemistry* **2005**, *44*, 8138.

(9) Riggs-Gelasco, P. J.; Price, J. C.; Guyer, R. B.; Brehm, J. H.; Barr, E. W.; Bollinger, J. M.; Krebs, C. *J. Am. Chem. Soc.* **2004**, *126*, 8108.

(10) Proshlyakov, D. A.; Henshaw, T. F.; Monterosso, G. R.; Ryle, M. J.; Hausinger, R. P. *J. Am. Chem. Soc.* **2004**, *126*, 1022.

(11) Sinnecker, S.; Svensen, N.; Barr, E. W.; Ye, S.; Bollinger J. Martin; Neese, F.; Krebs, C. *J. Am. Chem. Soc.* **2007**, *129*, 6168.

(12) Costas, M.; Mehn, M. P.; Jensen, M. P.; Que Jr, L. *Chem. Rev.* **2004**, *104*, 939.

(13) Groves, J. T.; Van der Puy, M. *J. Am. Chem. Soc.* **1976**, *98*, 5290.

(14) Chvapil, M.; Hurych, J. *Nature* **1959**, *184*, 1145.

(15) Hamilton, G. A.; Workman, R. J.; Woo, L. *J. Am. Chem. Soc.* **1964**, *86*, 3390.

(16) Siegel, B.; Lanphear, J. *J. Am. Chem. Soc.* **1979**, *101*, 2221.

(17) Siegel, B.; Lanphear, J. *J. Org. Chem.* **1979**, *44*, 942.

(18) Khenkin, A. M.; Shilov, A. E. *New J. Chem.* **1989**, *13*, 659.

(19) Chiou, Y. M.; Que Jr, L. *J. Am. Chem. Soc.* **1992**, *114*, 7567.

(20) Chiou, Y.-M.; Que Jr, L. *J. Am. Chem. Soc.* **1995**, *117*, 3999.

(21) Ho, R. Y. N.; Mehn, M. P.; Hegg, E. L.; Liu, A.; Ryle, M. J.; Hausinger, R. P.; Que Jr, L. *J. Am. Chem. Soc.* **2001**, *123*, 5022.

(22) Pavel, E. G.; Kitajima, N.; Solomon, E. I. *J. Am. Chem. Soc.* **1998**, *120*, 3949.

(23) Hegg, E. L.; Whiting, A. K.; Saari, R. E.; McCracken, J.; Hausinger, R. P.; Que Jr, L. *Biochemistry* **1999**, *38*, 16714.

(24) Ryle, M. J.; Padmakumar, R.; Hausinger, R. P. *Biochemistry* **1999**, *38*, 15278.

(25) Trewick, S. C.; Henshaw, T. F.; Hausinger, R. P.; Lindahl, T.; Sedgwick, B. *Nature* **2002**, *419*, 174.

(26) Ha, E. H.; Ho, R. Y. N.; Kisiel, J. F.; Valentine, J. S. *Inorg. Chem.* **1995**, *34*, 2265.

(27) Mukherjee, A.; Cranswick, M. a; Chakrabarti, M.; Paine, T. K.; Fujisawa, K.; Münck, E.; Que Jr, L. *Inorg. Chem.* **2010**, *49*, 3618.

(28) Kitajima, N.; Tamura, N.; Amagai, H.; Fukui, H.; Moro-oka, Y.; Mizutani, Y.; Kitagawa, T.; Mathur, R.; Heerwegh, K. *J. Am. Chem. Soc.* **1994**, *116*, 9071.

(29) Kim, K.; Lippard, S. J. *J. Am. Chem. Soc.* **1996**, *118*, 4914.

(30) Mehn, M. P.; Fujisawa, K.; Hegg, E. L.; Que Jr, L. *J. Am. Chem. Soc.* **2003**, *125*, 7828.

(31) Mukherjee, A.; Martinho, M.; Bominaar, E. L.; Münck, E.; Que Jr, L. *Angew.*

Chemie Int. Ed. **2009**, *48*, 1780.

(32) Janardanan, D.; Wang, Y.; Schyman, P.; Que Jr, L.; Shaik, S. *Angew. Chem. Int. Ed. Engl.* **2010**, *49*, 3342.

(33) Burzlaff, N. I.; Rutledge, P. J.; Clifton, I. J.; Hensgens, C. M. H.; Pickford, M.; Adlington, R. M.; Roach, P. L.; Baldwin, J. E. *Nature* **1999**, *401*, 721.

(34) Crawford, J. A.; Li, W.; Pierce, B. S. *Biochemistry* **2011**, *50*, 10241.

(35) Mbughuni, M. M.; Chakrabarti, M.; Hayden, J. A.; Bominaar, E. L.; Hendrich, M. P.; Münck, E.; Lipscomb, J. D. *Proc. Natl. Acad. Sci. U. S. A.* **2010**, *107*, 16788.

(36) Xing, G.; Diao, Y.; Hoffart, L. M.; Barr, E. W.; Prabhu, K. S.; Arner, R. J.; Reddy, C. C.; Krebs, C.; Bollinger, J. M. *Proc. Natl. Acad. Sci. U. S. A.* **2006**, *103*, 6130.

(37) Kovaleva, E. G.; Lipscomb, J. D. *Science* **2007**, *316*, 453.

(38) Shan, X.; Que, L. *Proc. Natl. Acad. Sci.* **2005**, *102*, 5340.

(39) Chiang, C.-W.; Kleespies, S. T.; Stout, H. D.; Meier, K. K.; Li, P.-Y.; Bominaar, E. L.; Que Jr, L.; Münck, E.; Lee, W.-Z. *J. Am. Chem. Soc.* **2014**, *136*, 10846.

(40) Hong, S.; Sutherlin, K. D.; Park, J.; Kwon, E.; Siegler, M. a.; Solomon, E. I.; Nam, W. *Nat. Commun.* **2014**, *5*, 5440.

(41) Oddon, F.; Chiba, Y.; Nakazawa, J.; Ohta, T.; Ogura, T.; Hikichi, S. *Angew. Chemie Int. Ed.* **2015**, *54*, 7336.

(42) Jensen, M. P.; Costas, M.; Ho, R. Y. N.; Kaizer, J.; Mairata i Payeras, A.; Münck, E.; Que, L.; Rohde, J.-U.; Stubna, A. *J. Am. Chem. Soc.* **2005**, *127*, 10512.

(43) Fiedler, A. T.; Que, L. *Inorg. Chem.* **2009**, *48*, 11038.

(44) Bollinger, J. M.; Krebs, C. *Curr. Opin. Chem. Biol.* **2007**, *11*, 151.

(45) van der Donk, W. a; Krebs, C.; Bollinger, J. M. *Curr. Opin. Struct. Biol.* **2010**, *20*, 673.

(46) Pojer, F.; Kahlich, R.; Kammerer, B.; Li, S.-M.; Heide, L. *J. Biol. Chem.* **2003**, *278*, 30661.

(47) Cicchillo, R. M.; Zhang, H.; Blodgett, J. A. V; Whitteck, J. T.; Li, G.; Nair, S. K.; van der Donk, W. A.; Metcalf, W. W. *Nature* **2009**, *459*, 871.

(48) Li, F.; Meier, K. K.; Cranswick, M. A.; Chakrabarti, M.; Van Heuvelen, K. M.; Münck, E.; Que Jr, L. *J. Am. Chem. Soc.* **2011**, *133*, 7256.

(49) Kitagawa, T.; Dey, A.; Lugo-Mas, P.; Benedict, J. B.; Kaminsky, W.; Solomon, E.; Kovacs, J. A. *J. Am. Chem. Soc.* **2006**, *128*, 14448.

(50) Ho, R. Y. N.; Jr., L. Q.; Roelfes, G.; Feringa, B. L.; Hermant, R.; Hage, R. *Chem. Commun.* **1999**, 2161.

(51) Simaan, A. J.; Döpner, S.; Banse, F.; Bourcier, S.; Bouchoux, G.; Boussac, A.; Hildebrandt, P.; Girerd, J.-J. *Eur. J. Inorg. Chem.* **2000**, *2000*, 1627.

(52) Ho, R. Y. N.; Roelfes, G.; Feringa, B. L.; Que, L. *J. Am. Chem. Soc.* **1999**, *121*, 264.

(53) Chow, M. S.; Liu, L. V; Solomon, E. I. *Proc. Natl. Acad. Sci.* **2008**, *105* , 13241.

(54) Decker, A.; Chow, M. S.; Kemsley, J. N.; Lehnert, N.; Solomon, E. I. *J. Am. Chem. Soc.* **2006**, *128*, 4719.

(55) Ashikawa, Y.; Fujimoto, Z.; Usami, Y.; Inoue, K.; Noguchi, H.; Yamane, H.; Nojiri, H. *BMC Struct. Biol.* **2012**, *12*, 15.

(56) Neibergall, M. B.; Stubna, A.; Mekmouche, Y.; Münck, E.; Lipscomb, J. D. *Biochemistry* **2007**, *46*, 8004.

(57) Karlsson, A.; Parales, J. V; Parales, R. E.; Gibson, D. T.; Eklund, H.; Ramaswamy, S. *Sci.* **2003**, *299* , 1039.

(58) Liu, L. V; Hong, S.; Cho, J.; Nam, W.; Solomon, E. I. *J. Am. Chem. Soc.* **2013**, *135*, 3286.

(59) Crabtree, R. H. *Chem. Rev.* **2010**, *110*, 575.

(60) Fujita, E.; Goldman, A. S. *Inorg. Chem.* **2015**, *54*, 5040.

(61) Sono, M.; Roach, M. P.; Coulter, E. D.; Dawson, J. H. *Chem. Rev.* **1996**, *96*, 2841.

(62) Solomon, E. I.; Brunold, T. C.; Davis, M. I.; Kemsley, J. N.; Lee, S.-K.; Lehnert, N.; Neese, F.; Skulan, A. J.; Yang, Y.-S.; Zhou, J. *Chem. Rev.* **2000**, *100*, 235.

(63) Puri, M.; Que Jr, L. *Acc. Chem. Res.* **2015**, *48*, 2443.

(64) Nam, W. *Acc. Chem. Res.* **2015**, *48*, 2415.

(65) Kleespies, S. T.; Oloo, W. N.; Mukherjee, A.; Que, L. *Inorg. Chem.* **2015**, *54*, 5053.

(66) McDonald, A. R.; Que Jr, L. *Coord. Chem. Rev.* **2013**, *257*, 414.

(67) Klinker, E. J.; Kaizer, J.; Brennessel, W. W.; Woodrum, N. L.; Cramer, C. J.; Que Jr, L. *Angew. Chemie Int. Ed.* **2005**, *44*, 3690.

(68) Hong, S.; So, H.; Yoon, H.; Cho, K.-B.; Lee, Y.-M.; Fukuzumi, S.; Nam, W. *Dalt. Trans.* **2013**, *42*, 7842.

(69) Wang, D.; Ray, K.; Collins, M. J.; Farquhar, E. R.; Frisch, J. R.; Gómez, L.; Jackson, T. A.; Kerscher, M.; Waleska, A.; Comba, P.; Costas, M.; Que Jr, L. *Chem. Sci.* **2013**, *4*, 282.

(70) Seo, M. S.; Kim, N. H.; Cho, K.-B.; So, J. E.; Park, S. K.; Clémancey, M.; Garcia-Serres, R.; Latour, J.-M.; Shaik, S.; Nam, W. *Chem. Sci.* **2011**, *2*, 1039.

(71) Company, A.; Prat, I.; Frisch, J. R.; Mas-Ballesté, D. R.; Güell, M.; Juhász, G.; Ribas, X.; Münck, D. E.; Luis, J. M.; Que Jr, L.; Costas, M. *Chem. - A Eur. J.* **2011**, *17*, 1622.

(72) Biswas, A. N.; Puri, M.; Meier, K. K.; Oloo, W. N.; Rohde, G. T.; Bominaar, E. L.; Münck, E.; Que Jr, L. *J. Am. Chem. Soc.* **2015**, *137*, 2428.

(73) Tse, C.-W.; Chow, T. W.-S.; Guo, Z.; Lee, H. K.; Huang, J.-S.; Che, C.-M. *Angew. Chemie Int. Ed.* **2014**, *53*, 798.

(74) Vincent, J. B.; Huffman, J. C.; Christou, G.; Li, Q.; Nanny, M. A.; Hendrickson, D. N.; Fong, R. H.; Fish, R. H. *J. Am. Chem. Soc.* **1988**, *110*, 6898.

(75) Kovaleva, E. G.; Lipscomb, J. D. *Nat Chem Biol* **2008**, *4*, 186.

(76) Loenarz, C.; Schofield, C. J. *Nat Chem Biol* **2008**, *4*, 152.

(77) Meunier, B.; de Visser, S. P.; Shaik, S. *Chem. Rev.* **2004**, *104*, 3947.

(78) Momenteau, M.; Reed, C. A. *Chem. Rev.* **1994**, *94*, 659.

(79) Groce, S. L.; Miller-Rodeberg, M. A.; Lipscomb, J. D. *Biochemistry* **2004**, *43*, 15141.

(80) Zhao, M.; Helms, B.; Slonkina, E.; Friedle, S.; Lee, D.; Dubois, J.; Hedman, B.; Hodgson, K. O.; Fréchet, J. M. J.; Lippard, S. J. *J. Am. Chem. Soc.* **2008**, *130*, 4352.

(81) Ray, K.; Pfaff, F. F.; Wang, B.; Nam, W. *J. Am. Chem. Soc.* **2014**, *136*, 13942.

(82) Addison, A. W.; Rao, T. N.; Reedijk, J.; van Rijn, J.; Verschoor, G. C. *J. Chem. Soc., Dalt. Trans.* **1984**, 1349.

(83) Schatz, M.; Raab, V.; Foxon, S. P.; Brehm, G.; Schneider, S.; Reiher, M.; Holthausen, M. C.; Sundermeyer, J.; Schindler, S. *Angew. Chemie Int. Ed.* **2004**, *43*, 4360.

(84) Peterson, R. L.; Himes, R. A.; Kotani, H.; Suenobu, T.; Tian, L.; Siegler, M. A.; Solomon, E. I.; Fukuzumi, S.; Karlin, K. D. *J. Am. Chem. Soc.* **2011**, *133*, 1702.

(85) Cho, J.; Kang, H. Y.; Liu, L. V; Sarangi, R.; Solomon, E. I.; Nam, W. *Chem. Sci.* **2013**, *4*, 1502.

(86) Cho, J.; Woo, J.; Nam, W. *J. Am. Chem. Soc.* **2010**, *132*, 5958.

(87) Bordwell, F. G.; Cheng, J.; Ji, G. Z.; Satish, A. V; Zhang, X. *J. Am. Chem. Soc.* **1991**, *113*, 9790.

(88) Katona, G.; Carpentier, P.; Nivière, V.; Amara, P.; Adam, V.; Ohana, J.; Tsanov, N.; Bourgeois, D. *Sci.* **2007**, *316* , 449.

(89) Shiemke, A. K.; Loehr, T. M.; Sanders-Loehr, J. *J. Am. Chem. Soc.* **1984**, *106*, 4951.

(90) Bukowski, M. R.; Comba, P.; Limberg, C.; Merz, M.; Que Jr, L.; Wistuba, T. *Angew. Chemie Int. Ed.* **2004**, *43*, 1283.

(91) Lehnert, N.; Ho, R. Y. N.; Que, L.; Solomon, E. I. *J. Am. Chem. Soc.* **2001**, *123*, 12802.

(92) Barraclough, C. G.; Lawrance, G. A.; Lay, P. A. *Inorg. Chem.* **1978**, *17*, 3317.

(93) Komiyama, K.; Furutachi, H.; Nagatomo, S.; Hashimoto, A.; Hayashi, H.; Fujinami, S.; Suzuki, M.; Kitagawa, T. *Bull. Chem. Soc. Jpn.* **2004**, *77*, 59.

(94) Garcia-Bosch, I.; Company, A.; Frisch, J. R.; Torrent-Sucarrat, M.; Cardellach, M.; Gamba, I.; Güell, M.; Casella, L.; Que Jr, L.; Ribas, X.; Luis, J. M.; Costas, M. *Angew. Chemie Int. Ed.* **2010**, *49*, 2406.

(95) Baldwin, M. J.; Ross, P. K.; Pate, J. E.; Tyeklar, Z.; Karlin, K. D.; Solomon, E. I. *J. Am. Chem. Soc.* **1991**, *113*, 8671.

(96) Donoghue, P. J.; Gupta, A. K.; Boyce, D. W.; Cramer, C. J.; Tolman, W. B. *J. Am. Chem. Soc.* **2010**, *132*, 15869.

(97) Brennan, B. A.; Chen, Q.; Juarez-Garcia, C.; True, A. E.; O'Connor, C. J.; Que, L. *Inorg. Chem.* **1991**, *30*, 1937.

(98) Cranswick, M. A.; Meier, K. K.; Shan, X.; Stubna, A.; Kaizer, J.; Mehn, M. P.; Münck, E.; Que Jr, L. *Inorg. Chem.* **2012**, *51*, 10417.

(99) Dong, Y.; Zang, Y.; Shu, L.; Wilkinson, E. C.; Que Jr, L.; Kauffmann, K.; Münck,

E. *J. Am. Chem. Soc.* **1997**, *119*, 12683.

(100) Moënne-Loccoz, P.; Baldwin, J.; Ley, B. A.; Loehr, T. M.; Bollinger, J. M. *Biochemistry* **1998**, *37*, 14659.

(101) Moënne-Loccoz, P.; Krebs, C.; Herlihy, K.; Edmondson, D. E.; Theil, E. C.; Huynh, B. H.; Loehr, T. M. *Biochemistry* **1999**, *38*, 5290.

(102) Broadwater, J. A.; Ai, J.; Loehr, T. M.; Sanders-Loehr; Fox, B. G. *Biochemistry* **1998**, *37*, 14664.

(103) Vu, V. V; Emerson, J. P.; Martinho, M.; Kim, Y. S.; Münck, E.; Park, M. H.; Que Jr, L. *Proc. Natl. Acad. Sci.* **2009**, *106*, 14814.

(104) Ho, R. Y. N.; Que Jr, L.; Roelfes, G.; Feringa, B. L.; Hermant, R.; Hage, R. *Chem. Commun.* **1999**, 2161.

(105) Liu, J.-G.; Ohta, T.; Yamaguchi, S.; Ogura, T.; Sakamoto, S.; Maeda, Y.; Naruta, Y. *Angew. Chemie Int. Ed.* **2009**, *48*, 9262.

(106) Mathé, C.; Mattioli, T. A.; Horner, O.; Lombard, M.; Latour, J.-M.; Fontecave, M.; Nivière, V. *J. Am. Chem. Soc.* **2002**, *124*, 4966.

(107) Lehnert, N.; Ho, R. Y. N.; Que Lawrence; Solomon, E. I. *J. Am. Chem. Soc.* **2001**, *123*, 8271.

(108) Chen, P.; Fujisawa, K.; Solomon, E. I. *J. Am. Chem. Soc.* **2000**, *122*, 10177.

(109) Balch, A. L. *Inorganica Chim. Acta* **1992**, *198–200*, 297.

(110) Zhang, Y.-X.; Du, D.-M.; Chen, X.; Lü, S.-F.; Hua, W.-T. *Tetrahedron: Asymmetry* **2004**, *15*, 177.

(111) Buick, R. *Philos. Trans. R. Soc. London B Biol. Sci.* **2008**, *363*, 2731.

(112) Yano, J.; Kern, J.; Sauer, K.; Latimer, M. J.; Pushkar, Y.; Biesiadka, J.; Loll, B.; Saenger, W.; Messinger, J.; Zouni, A.; Yachandra, V. K. *Sci.* **2006**, *314* , 821.

(113) Kanady, J. S.; Tsui, E. Y.; Day, M. W.; Agapie, T. *Sci.* **2011**, *333* , 733.

(114) Tsui, E. Y.; Tran, R.; Yano, J.; Agapie, T. *Nat Chem* **2013**, *5*, 293.

(115) Cox, N.; Pantazis, D. A.; Neese, F.; Lubitz, W. *Acc. Chem. Res.* **2013**, *46*, 1588.

(116) Ono, T.; Inoue, Y. *FEBS Lett.* **1988**, *227*, 147.

(117) Boussac, A.; Rutherford, A. W. *Biochemistry* **1988**, *27*, 3476.

(118) Ferguson-Miller, S.; Babcock, G. T. *Chem. Rev.* **1996**, *96*, 2889.

(119) Jiang, W.; Yun, D.; Saleh, L.; Barr, E. W.; Xing, G.; Hoffart, L. M.; Maslak, M.-A.; Krebs, C.; Bollinger, J. M. *Science (80-.).* **2007**, *316*, 1188.

(120) Andersson, C. S.; Öhrström, M.; Popović-Bijelić, A.; Gräslund, A.; Stenmark, P.; Högbom, M. *J. Am. Chem. Soc.* **2012**, *134*, 123.

(121) Mukhopadhyay, S.; Mandal, S. K.; Bhaduri, S.; Armstrong, W. H. *Chem. Rev.* **2004**, *104*, 3981.

(122) Tsui, E. Y.; Agapie, T. *Proc. Natl. Acad. Sci.* **2013**, *110* , 10084.

(123) Tsui, E. Y.; Kanady, J. S.; Agapie, T. *Inorg. Chem.* **2013**, *52*, 13833.

(124) Chen, C.; Zhang, C.; Dong, H.; Zhao, J. *Chem. Commun.* **2014**, *50*, 9263.

(125) Kim, E.; Chufán, E. E.; Kamaraj, K.; Karlin, K. D. *Chem. Rev.* **2004**, *104*, 1077.

(126) Chufán, E. E.; Puiu, S. C.; Karlin, K. D. *Acc. Chem. Res.* **2007**, *40*, 563.

(127) Hotzelmann, R.; Wieghardt, K.; Floerke, U.; Haupt, H. J.; Weatherburn, D. C.; Bonvoisin, J.; Blondin, G.; Girerd, J. J. *J. Am. Chem. Soc.* **1992**, *114*, 1681.

(128) Fukuzumi, S.; Morimoto, Y.; Kotani, H.; Naumov, P.; Lee, Y.-M.; Nam, W. *Nat. Chem.* **2010**, *2*, 756.

(129) Swart, M. *Chem. Commun.* **2013**, *49*, 6650.

(130) Prakash, J.; Rohde, G. T.; Meier, K. K.; Jasniewski, A. J.; Van Heuvelen, K. M.;

Münck, E.; Que Jr, L. *J. Am. Chem. Soc.* **2015**, *137*, 3478.

(131) Prakash, J.; Rohde, G. T.; Meier, K. K.; Münck, E.; Que, L. *Inorg. Chem.* **2015**, *54*, 11055.

(132) Rohde, J.-U.; In, J.-H.; Lim, M. H.; Brennessel, W. W.; Bukowski, M. R.; Stubna, A.; Münck, E.; Nam, W.; Que Jr, L. *Science* **2003**, *299*, 1037.

(133) Zhou, A.; Kleespies, S. T.; Van Heuvelen, K. M.; Que, L. *Chem. Commun.* **2015**, *51*, 14326.

(134) Koehntop, K. D.; Rohde, J.-U.; Costas, M.; Que Jr., L. *Dalt. Trans.* **2004**, 3191.

(135) Shan, X.; Rohde, J.-U.; Koehntop, K. D.; Zhou, Y.; Bukowski, M. R.; Costas, M.; Fujisawa, K.; Que, L. *Inorg. Chem.* **2007**, *46*, 8410.

(136) Kurtz, D. M. *Chem. Rev.* **1990**, *90*, 585.

(137) Lee, S. C.; Holm, R. H. *J. Am. Chem. Soc.* **1993**, *115*, 11789.

(138) Berry, J. F.; Bill, E.; García-Serres, R.; Neese, F.; Weyhermüller, T.; Wieghardt, K. *Inorg. Chem.* **2006**, *45*, 2027.

(139) Liston, D. J.; Kennedy, B. J.; Murray, K. S.; West, B. O. *Inorg. Chem.* **1985**, *24*, 1561.

(140) Sanders-Loehr, J.; Wheeler, W. D.; Shiemke, A. K.; Averill, B. A.; Loehr, T. M. *J. Am. Chem. Soc.* **1989**, *111*, 8084.

(141) Zheng, H.; Zang, Y.; Dong, Y.; Young, V. G.; Que Jr, L. *J. Am. Chem. Soc.* **1999**, *121*, 2226.

(142) Westre, T. E.; Kennepohl, P.; DeWitt, J. G.; Hedman, B.; Hodgson, K. O.; Solomon, E. I. *J. Am. Chem. Soc.* **1997**, *119*, 6297.

(143) Roe, A. L.; Schneider, D. J.; Mayer, R. J.; Pyrz, J. W.; Widom, J.; Que, L. *J. Am. Chem. Soc.* **1984**, *106*, 1676.

(144) Jackson, T. A.; Rohde, J.-U.; Seo, M. S.; Sastri, C. V; DeHont, R.; Stubna, A.; Ohta, T.; Kitagawa, T.; Münck, E.; Nam, W.; Que Jr, L. *J. Am. Chem. Soc.* **2008**, *130*, 12394.

(145) Czarnecki, K.; Nimri, S.; Gross, Z.; Proniewicz, L. M.; Kincaid, J. R. *J. Am. Chem. Soc.* **1996**, *118*, 2929.

(146) Prakash, J.; Rohde, G. T. .

(147) Nocera, D. G. *Acc. Chem. Res.* **2012**, *45*, 767.

(148) Kärkäs, M. D.; Verho, O.; Johnston, E. V; Åkermark, B. *Chem. Rev.* **2014**, *114*, 11863.

(149) Blakemore, J. D.; Crabtree, R. H.; Brudvig, G. W. *Chem. Rev.* **2015**, 150720112150009.

(150) Fillol, J. L.; Codolà, Z.; Garcia-Bosch, I.; Gómez, L.; Pla, J. J.; Costas, M. *Nat. Chem.* **2011**, *3*, 807.

(151) Codolà, Z.; Garcia-Bosch, I.; Acuña-Parés, F.; Prat, I.; Luis, J. M.; Costas, M.; Lloret-Fillol, J. *Chemistry* **2013**, *19*, 8042.

(152) Hong, D.; Mandal, S.; Yamada, Y.; Lee, Y.-M.; Nam, W.; Llobet, A.; Fukuzumi, S. *Inorg. Chem.* **2013**, *52*, 9522.

(153) Chen, G.; Chen, L.; Ng, S.-M.; Man, W.-L.; Lau, T.-C. *Angew. Chemie Int. Ed.* **2013**, *52*, 1789.

(154) Lutz, O. M. D.; Hofer, T. S.; Randolf, B. R.; Weiss, A. K. H.; Rode, B. M. *Inorg. Chem.* **2012**, *51*, 6746.

(155) Piro, N. A.; Robinson, J. R.; Walsh, P. J.; Schelter, E. J. *Coord. Chem. Rev.* **2014**, *260*, 21.

(156) Wilkinson, E. C.; Dong, Y.; Zang, Y.; Fujii, H.; Fraczkiewicz, R.; Fraczkiewicz, G.; Czernuszewicz, R. S.; Que, L. *J. Am. Chem. Soc.* **1998**, *120*, 955.

(157) Skulan, A. J.; Hanson, M. A.; Hsu, H.; Que Jr, L.; Solomon, E. I. *J. Am. Chem. Soc.* **2003**, *125*, 7344.

(158) Xue, G.; Fiedler, A. T.; Martinho, M.; Münck, E.; Que, L. *Proc. Natl. Acad. Sci.* **2008**, *105* , 20615.

(159) Que Jr, L.; Tolman, W. B. *Angew. Chem. Int. Ed. Engl.* **2002**, *41*, 1114.

(160) Murakami, M.; Hong, D.; Suenobu, T.; Yamaguchi, S.; Ogura, T.; Fukuzumi, S. *J. Am. Chem. Soc.* **2011**, *133*, 11605.

(161) Yoshida, M.; Masaoka, S.; Abe, J.; Sakai, K. *Chem. - An Asian J.* **2010**, *5*, 2369.

(162) Kimoto, A.; Yamauchi, K.; Yoshida, M.; Masaoka, S.; Sakai, K. *Chem. Commun.* **2012**, *48*, 239.

(163) Lee, W.-Z.; Chiang, C.-W.; Lin, T.-H.; Kuo, T.-S. *Chemistry* **2012**, *18*, 50.

(164) Wasylenko, D. J.; Ganesamoorthy, C.; Henderson, M. A.; Koivisto, B. D.; Osthoff, H. D.; Berlinguette, C. P. *J. Am. Chem. Soc.* **2010**, *132*, 16094.

(165) Umena, Y.; Kawakami, K.; Shen, J.-R.; Kamiya, N. *Nature* **2011**, *473*, 55.

(166) Codolà, Z.; Gómez, L.; Kleespies, S. T.; Que Jr, L.; Costas, M.; Lloret-Fillol, J. *Nat. Commun.* **2015**, *6*, 5865.